

Multi-functional Optoelectronic Substrates

by

Sajad Haghanifar

MS in Material Science and Engineering, University of Tehran,
2012

Submitted to the Graduate Faculty of
the Swanson School of Engineering in partial fulfillment
of the requirements for the degree of

Doctor of Philosophy

University of Pittsburgh

2020

UNIVERSITY OF PITTSBURGH
SWANSON SCHOOL OF ENGINEERING

This dissertation was presented

by

Sajad Haghanifar

It was defended on

March 25, 2020

and approved by

Paul W. Leu, Ph.D., Associate Professor, Department of Industrial Engineering

Young Jae Chun, Ph.D., Associate Professor, Department of Industrial Engineering

Mostafa Bedewy, Ph.D., Assistant Professor, Department of Industrial Engineering

Paul Ohodnicki, Ph.D., Associate Professor, Department of Mechanical Engineering and

Materials Science

Dissertation Director: Paul W. Leu, Ph.D., Associate Professor, Department of Industrial

Engineering

Copyright © by Sajad Haghanifar
2020

Multi-functional Optoelectronic Substrates

Sajad Haghanifar, PhD

University of Pittsburgh, 2020

New bio-inspiration, micro-/nanomaterials, and micro-/nanomanufacturing processes offer unprecedented opportunities in engineering optoelectronic substrates for novel photon management strategies, difficult-to-realize material–property combinations, and new multi-functionality. In the past decade, discoveries in the multi-functional properties of micro-/nanostructured surfaces have led to a renaissance of activity in surface engineering, which have transformed substrates for a wide variety of rigid and flexible optoelectronic devices.

The most important properties are related to photon management, such as high transparency, antireflection, and haze control. Transparency is the most important property as this determines the amount of light that either goes into or out of the active region of the device. In addition, haze control is an important property for various devices. Displays and touch screens require low optical haze, as high haze can contribute to the blurriness of text and images viewed. In contrast, applications such as solar cells and light emitting diodes (LEDs) would benefit from substrates with both high transparency and high haze. Substrates with high haze can increase how much light scatters into or out of the photoactive layers and may increase the solar cell power conversion efficiency and display or LED extraction efficiency, respectively.

In addition to photon management properties, a wide variety of other properties are important that are related to the reliability of the optical properties under a variety of stressors. This includes wettability-related properties such as anti-soiling, self-cleaning, stain-resistance, fog resistance, where it is beneficial for the substrate to maintain its optical properties after exposure to various particulates or liquids. Durability under abrasion, hydrostatic pressure, and repeated bending are also important. Finally, properties such as optical switching may also be useful for various applications.

In this study, we summarize our recent research progress in the micro-/nanostructuring of various optoelectronic substrate materials while discussing sources of bio-inspiration, advances in micro-/nanomanufacturing and machine learning strategies we used for fabrication of multi-functional optoelectronic substrates. These engineered surfaces have broad application to a wide variety of substrates for applications such as displays, solar cells, smartphones, light emitting diodes (LEDs), and e-paper, as well as new wearables, RF-ID tags, artificial skin, and medical/health sensors.

Table of Contents

Preface	xii
1.0 Introduction	1
1.1 Bio-inspiration	2
1.2 Photon Management Properties	3
1.3 Wetting Properties and Multi-Functionality	3
1.4 Durability	4
1.5 Choice of Material	4
2.0 Fundamental Performance Limits and Haze Evaluation of Metal Nanomesh	
Transparent Conductors	6
2.1 Introduction	6
2.2 Results and Discussion	7
2.3 Conclusions	17
3.0 High Transparency, High Haze Optoelectronic Substrates	18
3.1 High Transparency, Ultrahigh Haze Nanograss Glass with Fluid-Induced Switchable Haze	18
3.1.1 Introduction	18
3.1.2 Results and Discussion	19
3.1.3 Conclusions	27
3.2 Flexible Nanograss With Highest Combination Of Transparency And Haze For Optoelectronic Plastic Substrates	27
3.2.1 Introduction	27
3.2.2 Results and Discussion	28
3.2.3 Conclusions	34
4.0 Superomniphobic Optical Substrate	35
4.1 Self-Cleaning, High Transmission, Near Unity Haze OTS/Silica Nanostruc- tured Glass	35

4.1.1	Introduction	35
4.1.2	Results and Discussion	36
4.1.3	Conclusions	48
4.2	Stain-Resistant, Superomniphobic Flexible Optical Plastics Based on Nano- Enoki Mushrooms	48
4.2.1	Introduction	48
4.2.2	Results and Discussion	50
4.2.3	Conclusions	60
5.0	Toward Finding Perfect Antireflection and Superomniphobic Structures . .	61
5.1	Creating Glasswing-Butterfly Inspired Glass Through Bayesian Learning and Optimization	61
5.1.1	Introduction	61
5.1.2	Fabrication Strategy	64
5.1.3	Experimental design methodology	67
5.1.4	Standard Bayesian optimization	67
5.1.5	Modifications to Bayesian optimization	68
5.1.6	Results and Discussion	71
5.1.7	Characterizing the nanostructured glass properties	73
5.1.8	Characterizing the nanostructured glass functionality	76
5.1.9	Conclusion	79
5.2	Discovering Near-Perfect Broadband and BroadAngle Antireflection Sur- faces for Optoelectronics by Machine Learning	79
5.2.1	Introduction	79
5.2.2	Results and discussion	81
5.2.3	Conclusion	87
5.3	3D Printed Superomniphobic Structures With Ultra-Low Hysteresis, and High Abrasion Resistance	87
5.3.1	Introduction	87
5.3.2	Results and Discussion	89
5.3.3	Conclusion	95

6.0 Conclusions and prospects	96
Appendix. Additional Details For: Discovering Perfect Broadband and Broad	
AngleAntireflection Surfaces for Optoelectronics byMachine Learning	98
A.1 Experimental	98
A.1.1 Fabrication process	98
A.1.2 Optical characterization	99
A.1.3 Simulation	100
A.2 Results and discussion	100
A.2.1 NW array	101
A.2.2 NC array	101
A.2.3 Literature data on fabricated NC array	102
Bibliography	104

List of Tables

1	Fabricated NC array details in literature.	102
---	--	-----

List of Figures

1	Optoelectronic substrates, properties, applications and functionality.	2
2	Simulated metal nanomesh properties.	9
3	Diffraction patterns of different metal nanomeshes.	10
4	Performance limits evaluation of Cu nanomeshes.	11
5	SEM images of Cu nanomesh.	12
6	Angular distribution function of Cu nanomesh.	14
7	Range of transmission, haze and sheet resistance of Cu nanomesh.	15
8	Transmission and haze as a function of wavelength for Cu nanomeshes. . . .	16
9	SEM images of hazy glass.	19
10	Transmission and haze contour plots for hazy glass.	21
11	Transmission and haze as a function of nanoglass height.	22
12	Theoretical and experimental comparison of hazy glass.	23
13	Optical images of hazy glass.	24
14	Scattering ability of hazy glass	25
15	Water contact angle and switch ability of hazy glass.	26
16	Optical plots of dry and wet hazy glass.	26
17	Schematic and SEM images of hazy plastic.	29
18	Optical plots of hazy plastic.	31
19	Hazy plastic bending durability.	33
20	Schematic and SEM images of superhydrophobic glass.	37
21	SEM images of different blade heights superhydrophobic glass.	39
22	Transmission plots of superhydrophobic glass.	41
23	Haze and angular distribution function of superhydrophobic glass.	42
24	Pareto-frontier of high haze high transmission substrates.	42
25	Wetting characterization of superhydrophobic glass.	43
26	Self-cleaning characterization of superhydrophobic glass.	45

27	Life cycle of superhydrophobic glass.	46
28	SEM images of Nano-enoki mushroom structures on PET.	50
29	Surface wetting results Nano-enoki PET.	51
30	Stability characterization of Cassie-Baxter state wetting.	55
31	Optical plots of nano-enoki PET.	56
32	Comparison of transparency, haze, water and ethylene glycol contact angle. .	57
33	Stain test results of nano-enoki PET.	58
34	Nano-enoki PET bending durability.	59
35	Schematic of experimental fabrication for glasswing-butterfly inspired glass .	65
36	Sample depiction of proposed Bayesian optimization process.	72
37	Depictions of the experimental design.	73
38	SEM images and optical plots of nanostructured glass.	75
39	Condensation behaviour of nanostructured glass.	76
40	Self-healing behaviour of nanostructured glass.	78
41	Bayesian learning and optimization of electrodynamic simulation results. . .	82
42	Post-hoc analysis of optimal and near-optimal results.	84
43	Experimental NC array results.	85
44	Schematic of 3D printed superomniphobic structures.	89
45	Breakthrough pressure and solid fraction area of 3D printed structures. . . .	91
46	SEM images of 3D printed superomniphobic structures.	92
47	Abrasion resistant behaviour of 3D printed structures.	94
48	SEM images of fabricated NC array.	99
49	Nearly efficient of NW array.	101
50	Nearly efficient of NC array.	102

Preface

This work is dedicated to my parents, Sara and Ali, and my wife Mona.

I would first like to thank my academic advisor, Dr. Paul Leu, for giving me the opportunity to pursue my Ph.D. degree at University of Pittsburgh. Over the four years, his mentorship has always been very helpful and inspiring. I would also like to thank Professors Youngjae Chun, Mostafa Bedewy and Paul Ohodnicki for serving on my candidacy and thesis committees. I appreciate their time and the valuable comments on my research and on my life.

I would like to acknowledge and thank all of the students and staff members that I have worked with, learned from, and become friends with over the years. I'd like to thank Drs. Tongchuan Gao, and Md Imrul Kayes for the useful discussions and their devotion to our research projects. I would like to thank the staff members who helped me at University of Pittsburgh: Dr. Susheng Tan, Mike McDonald, Dr. Jun Chen, Dr. Daniel Lamont and Matthew France in Gertrude E. & John M. Petersen Institute of NanoScience and Engineering, and Dr. Shervin Siammak in the Center for Simulation & Modeling. I also would like to thank all of our collaborators, Dr. Michael McCourt and Dr. Bolong Cheng at Sigopt, Dr. Paul Ohodnicki, Dr. Jeffrey Wuenschell, Dr. Ping Lu, and Dr. Ki-Joong Kim at the National Energy Technology Laboratory, U.S. Department of Energy for their help and support.

I would like to thank the graduate students: Anthoney Galante, Bradley Pafchek, Ziyu Zhou, and Zhengyu Xu as well as all undergraduate students I had the privilege of mentoring in Dr. Leu's Laboratory of Advanced Materials at Pittsburgh (LAMP): Rafael T Rodriguez De Vecchis, Maxwell G Lindsay, Luke M Tomasovic, Sooraj Sharma, and Benjamin Bailey. I would also thank my friends at the Department of Industrial Engineering, specially Shadi Sanoubar, Mohsen Tabrizi, and Moataz Elsisy for their help and for being such good friends. I would like to express my sincere gratitude to all the my friends here in Pittsburgh for their continuous help and support. I would definitely miss my Pittsburgh family.

I would like to dedicate my special thanks to my lovely wife, Mona, for all her company and the sweet moments over the four years. She is going to be a doctor, soon, too. You always give me the energy to become a better researcher and also a better person in life. Lastly but most importantly, I would like to thank my mom and dad for their unconditional love and for supporting me to pursue my Ph.D. degree abroad. You are the reason I have done all this, and my siblings Leila and Saeed. I missed you so much.

1.0 Introduction

Optoelectronic substrates are a critical component in a wide variety of optoelectronic devices such as displays, solar panels, smart phones, tablets, e-paper, touchscreens, and lighting. These substrates must allow light to pass through with high efficiency, protect the device from the ambient environment, and offer additional multi-functionality. Flexible optoelectronic substrates are also needed for emerging flexible versions of the aforementioned optoelectronic devices, as well as new wearables, RF-ID tags, artificial skin, and medical sensors. Glass is most commonly used for optoelectronic substrates, but there also is great interest in new types of flexible glass or plastics and paper.

Over the past decade, bio-inspiration from various natural surfaces as well as new advances in micro-/nanomanufacturing have led to a renaissance of activity in optoelectronic substrate research (Fig. 1). In this study, we summarize recent research progress while discussing sources of bio-inspiration, advances in micro-/nanomanufacturing, and challenges and prospects related to optoelectronic substrates and their integration into various optoelectronic applications. First, we discuss some of the photon management properties that are relevant to optoelectronic substrates such as transparency and haze. Next, we discuss some of the functionalities that are desirable for maintaining optical properties in various environments such as anti-soiling, anti-fouling, self-cleaning, stain-resistance, and anti-fogging. We discuss a variety of natural surfaces that have served as bio-inspiration for providing these optical properties and functionality, such as insect eyes, insect wings, and lotus leaves.

Finally, we discuss the durability of these various optoelectronic substrates. We discuss how the optoelectronic substrate must maintain its properties and functionality in the presence of various stressors such as bending, abrasion, condensation, and pressure.

1.1 Bio-inspiration

Over time, various animals, insects and plants have developed unique microscale or nanoscale topography and surface chemistry for specific functionalities that help them survive. Biologically evolved surfaces exemplify various functionalities of nano- and microscale features including anti-reflection, camouflage, anti-hazing, liquid repellency, light absorption, and anti-icing. These natural surfaces have inspired research into how these surface provide for these desired functionalities and utilized this research to demonstrated various synthetic surfaces with novel functionalities.

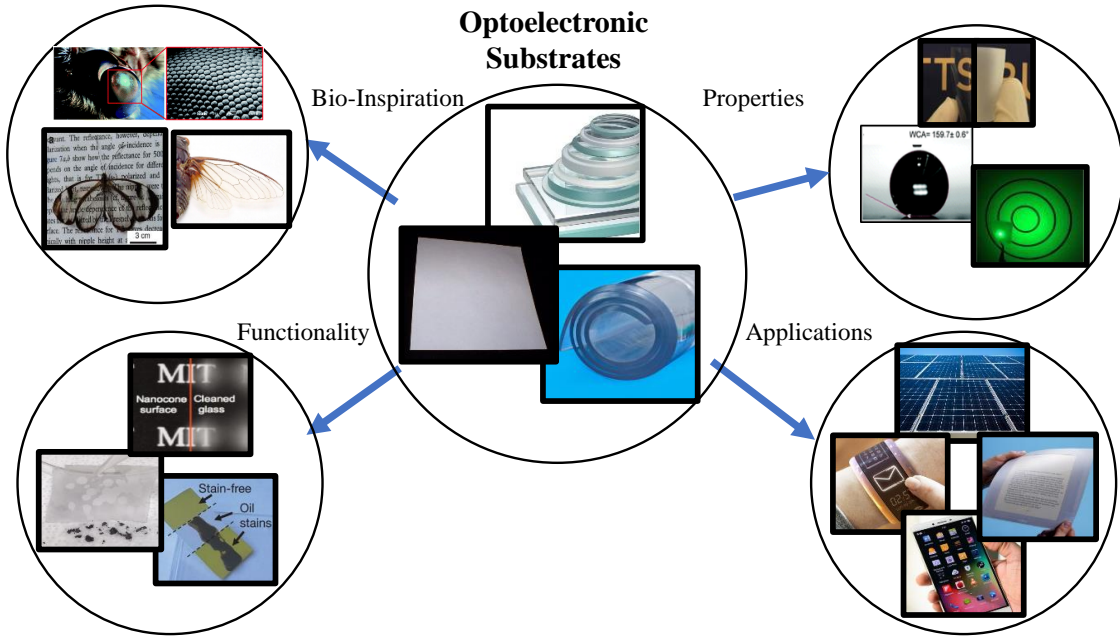


Figure 1 Optoelectronic substrates includes glass, paper, and plastics that are bio-inspired by examples from nature such as the moth eye [104], glass wing butterfly [171] and cicada wing [17]. Various properties are valued such as high transparency and high haze [69, 64], high transparency and low haze [67, ?], high water contact angle [65] as well as functionalities such as self-cleaning [65], anti-fogging [150], and stain resistance [199]. Optoelectronic applications include traditional rigid solar cells, electronic devices, electronic paper, and touch screens as well as emerging flexible versions of these devices as well as wearables and health/medical sensors.

1.2 Photon Management Properties

The photon management properties of transparency and haze are important with regard to optoelectronic substrates. High transparency substrates are essential for optoelectronic applications to increase the amount of light going into or coming out of the device. Maximizing the transparency is equivalent to minimizing the reflection for nonabsorbing materials. Thus, optoelectronic materials are often described in terms of their antireflecting properties, which may be needed across a broad range of wavelengths as well as a wide range of incidence angles.

Optical haze is another important characteristic of an optoelectronic substrate and defined as the percent of transmitted scattered light to the total transmission. Displays and touch screens require low haze [227, 52, 77, 124], which provides for clarity of text and images. On the other hand, substrates with high haze can increase how much light scatters into or out of the photoactive layers and may increase the power conversion efficiency or extraction efficiency of solar cells [134] and LEDs[71], respectively.

1.3 Wetting Properties and Multi-Functionality

Optoelectronic devices must maintain their performance in various environments and thus a variety of functionalities related to maintaining their optical performance are often desired. These functionalities include anti-soiling, anti-biofouling, self-cleaning, stain-resistance, anti-icing, and anti-fogging. Soiling refers to the accumulation of dust and other airborne particulates which reduce the transmission of light through the substrate into or out of the device. Anti-soiling surfaces reduce the adhesion of these particulates onto the surface. Microbes can adhere to surfaces and form biofilms, which can lead to structural or functional issues in the surface or contribute to the transmittance of infectious diseases. Anti-biofouling surfaces reduce the adhesion of these microorganisms. Self-cleaning is also often useful, where any dust, particles, or organisms, may be easily removed upon the application of heat, water or solvent. Stain-resistance functionality

refers to the ability of the surface to resist discoloration from exposure to different liquids or fingerprint marks from touching or swiping. Anti-icing surfaces inhibit the formation of ice or frost which can reduce visibility. Finally, there is also interest in anti-fogging functionality where the condensation of water is hindered. Small droplets of water may scatter light and inhibit visibility. These functionalities are often closely correlated with the wetting characteristics of the surface.

1.4 Durability

Optoelectronic substrates typically form a barrier between the optoelectronic device and the environment. This is of great importance to optoelectronic devices, which may degrade in the presence of water and oxygen vapor molecules. The environment may also include the impact of salts and ultraviolet illumination. This is of particular importance to optoelectronic devices made of organic materials or perovskites, which tend to have poor stability.

In addition to effects on the optoelectronic device, various stressors may also effect the surface properties and functionality. Elevated temperatures, sea water, UV-light, outdoor exposure, acidic/alkali environments, and mechanical effects may degrade performance through the loss of optical properties or other functionalities. New strategies are being investigated for improving the durability of these multi-functional surfaces.

1.5 Choice of Material

Glass is ubiquitous as a rigid optoelectronic substrate due to its high optical transparency, low cost, and moisture barrier properties. Various types of glass such as soda lime, fused silica, lead, borosilicate glass, and aluminosilicate glass are typically used for optoelectronic applications. New types of smaller thickness glass, which not only reduce the weight of the glass, but decrease its bending stiffness so that that it can be flexed are

being researched [50]. Plastics and paper are also being researched for flexible optoelectronic applications, which not only include flexible versions of traditional rigid applications but new types of biomedical optoelectronic applications.

Plastics exhibit a high degree of mechanical flexibility and durability, and can be made transparent and integrated with low cost roll-to-roll manufacturing processes. Plastics are very attractive for industrial use due to their light weight and low prices. Semicrystalline polyethylene terephthalate (PET) and polyethylene naphthalate (PEN) polymers are the two main transparent flexible substrates used for flexible optoelectronics. These plastics exhibit good chemical resistance and high melting point, though manufacturing processes are still typically constrained to less than 200 °C.

Recently, paper substrates have attracted interest of both industry and researchers. Paper is an environmental-friendly and low cost material that can be made in mass quantities with roll-to-roll fabrication process[207]. Also, paper is flexible and lightweight. However, the major obstacle to the use of paper in optoelectronics is that paper is generally not transparent. Paper is typically comprised of cellulose fibers with diameters of 10 to 50 μm and lengths of several millimeters. The cell wall of a cellulose fiber consists of a bunch of microfibrils (5 to 50 nm in diameter and several micrometers in length). The microfibrils themselves are composed of self-assembled elementary fibrils, with a diameter of 3.5 nm [62]. This microscale surface roughness and opaqueness of cellulosic papers have limited its incorporation into optoelectronic applications. There is a great interest in fabricating transparent paper through the use of microfibrils or nanofibrillated cellulose as well as surface roughness reduction. [147, 38, 41, 160, 210, 187, 166, 143, 206, 78, 169, 144, 87, 208, 225, 115, 140, 142]. Recently, Ha *et al.* reviewed the application of paper in a wide variety of electronic and optoelectronic devices.[62] Paper may be used in photovoltaics, as an antireflection coating [61, 60] or as a substrate [34, 2, 82, 189, 110, 80, 98, 228, 190, 105]. Paper may also be used in other optoelectronic applications such as transparent conductive electrodes [78, 80, 33, 194, 111, 162, 156, 153, 100, 101, 200, 43, 159, 75, 36, 123, 163, 205, 37, 54, 141, 3, 191, 204], OLEDs [211, 5, 193, 56, 137, 158, 230, 130, 183, 146, 108] and touch screens [33, 128].

2.0 Fundamental Performance Limits and Haze Evaluation of Metal Nanomesh Transparent Conductors

In this chapter, we comprehensively evaluate the optical transmission, sheet resistance, and haze of metal nanomeshes to determine their fundamental performance limits as transparent conductors through both simulations and experiments. Numerical and analytical simulations are used to evaluate the tradeoffs and correlations between these three figure of merits [44].

2.1 Introduction

Transparent conductors are an important component in a variety of optoelectronic applications, such as solar cells[216, 184, 95], displays, touch screens, and light-emitting diodes (LEDs)[107, 172, 112]. Recently, many inexpensive and alternative flexible transparent conductors have been demonstrated, including metal nanowires,[24, 18, 28], carbon based materials[6, 76, 27], and metal grids and nanomeshes,[132, 49] as well as various hierarchical structures [106, 48, 45, 122]. Many of these alternative transparent conductors have demonstrated comparable or superior performance to indium tin oxide (ITO) in terms of optical transmission and sheet resistance.

Most research on alternative transparent conductors has focused on evaluating and understanding the performance limits and tradeoffs in terms of optical transmission and sheet resistance, such as the study on metal nanowire films [47, 46, 9]. However, aside from these two figures of merit, haze, which describes the amount of transmitted light that is scattered, is another important figure of merit for transparent conductors that has largely been unstudied. In optoelectronic devices, haze determines how much light couples into or out of the underlying photoactive layers. High haze, for instance, is important for applications such as solar cells and LEDs, since more light can couple into and out of photoactive layers, respectively. [211] Yet, there has only been one limited study on

the haze of nanowire films so far, which compared the properties of two diameters of nanowires [157]. It is still not clear how to control haze in nanowire films, because the haze also depends on the nanowire film spacing, uniformity, alignment, and ordering, and there tends to be much randomness in these films.

In contrast to random metal nanowire films, we demonstrated metal nanomeshes that may be fabricated with well-defined morphology and high uniformity over large areas in any metal that can be deposited. [49] These metal nanomeshes have demonstrated comparable performance to ITO. The ability to fabricate metal nanomeshes with well-defined pitch, hole diameter, and thickness, translates to the engineering of particular optical properties such as transmission and haze.

In this chapter, we evaluate the optical transmission, sheet resistance, and haze of metal nanomeshes as transparent conductors. We study these properties comprehensively through simulations for all nanomeshes with pitch and diameter less than 4000 nm and a thickness of 50 nm. The fundamental performance limits of these three properties are evaluated, and the tradeoffs between these three figures of merit as well as the correlations between these properties are discussed. In particular, a strong correlation between haze and transparency is found in nanomeshes. Metal nanomeshes with high transparency tend to have low haze and *vice versa*. Furthermore, we fabricate Cu nanomeshes with a range of geometries to verify our simulation results. The haze of metal nanomeshes may be primarily explained by Fraunhofer diffraction theory, and the spectral dependence of haze may be explained by Mie scattering from the metal regions between holes. Here, we focus on Cu nanomeshes, though the results of our studies should also apply to other metals. These results should also apply to all types of grating or grid-like structures, in which the metal structure has a well-defined 2D lattice.

2.2 Results and Discussion

Figure 2 shows a summary of our simulation results for metal nanomeshes. Figure 2(a) shows a schematic of the metal nanomesh, which consists of a metal thin film with cylindri-

cal holes patterned in a hexagonal lattice. The morphology of metal nanomeshes is defined by the pitch of the hexagonal array a , the diameter of the holes d , and the thickness of the metal t . Figures 2(b), (c), and (d) show the sheet resistance R_s , total transmission at wavelength $\lambda = 550$ nm, and haze at $\lambda = 550$ nm, respectively, as a function of metal nanomesh pitch a and hole diameter d for nanomeshes with thickness $t = 50$ nm. The pitch a and hole diameter d range from 600 to 4000 nm, with $d < a$ to ensure continuity of the metal. The sheet resistance shown in Fig. 2(b) was obtained through finite element analysis simulations and calculated as the average of $R_{s,xx}$ and $R_{s,yy}$, where $R_{s,xx}$ and $R_{s,yy}$ are the sheet resistance measured in x - and y -direction, respectively. The simulations assume the bulk resistivity of Cu ($\rho = 1.68 \times 10^{-8}$ $\Omega\cdot\text{m}$) and do not consider the polycrystallinity of the Cu or surface scattering of electrons. Thus, R_s should simply decrease linearly with increasing thickness in these simulations.

The optical total transmission in Fig. 2(c) accounts for the light scattered into all angles (both non-scattered and scattered) and will be referred to as the transmission, unless otherwise specified. The optical transmission was simulated by the finite-difference time-domain method with periodic boundary conditions.[213] Cu films are essentially opaque when thicker than 30 nm, [47] so the Cu nanomesh transmission should become constant for thicknesses over 30 nm. The transmission is averaged for incident light polarized along the x - and y -direction with 550 nm wavelength. We find that a pitch greater than 1000 nm is needed for achieving transmission over 80%.

The haze H shown in Fig. 2(d) is defined as

$$H = \frac{\text{forward scattered light}}{\text{total transmission}} \times 100\%, \quad (2.1)$$

where the total transmission is composed of forward non-scattered light and forward scattered light. The haze is computationally investigated by calculating the analytical Fraunhofer diffraction pattern of metal nanomeshes, where the metal nanomeshes are an infinite hexagonal array of cylindrical holes in an optically opaque film. The Fraunhofer diffraction pattern is calculated by sampling the diffraction pattern of a single hole (Bessel function of the first kind) at the k -points associated with the reciprocal lattice of the two-dimensional hexagonal hole lattice. The (0, 0) diffraction mode is considered the forward non-scattered

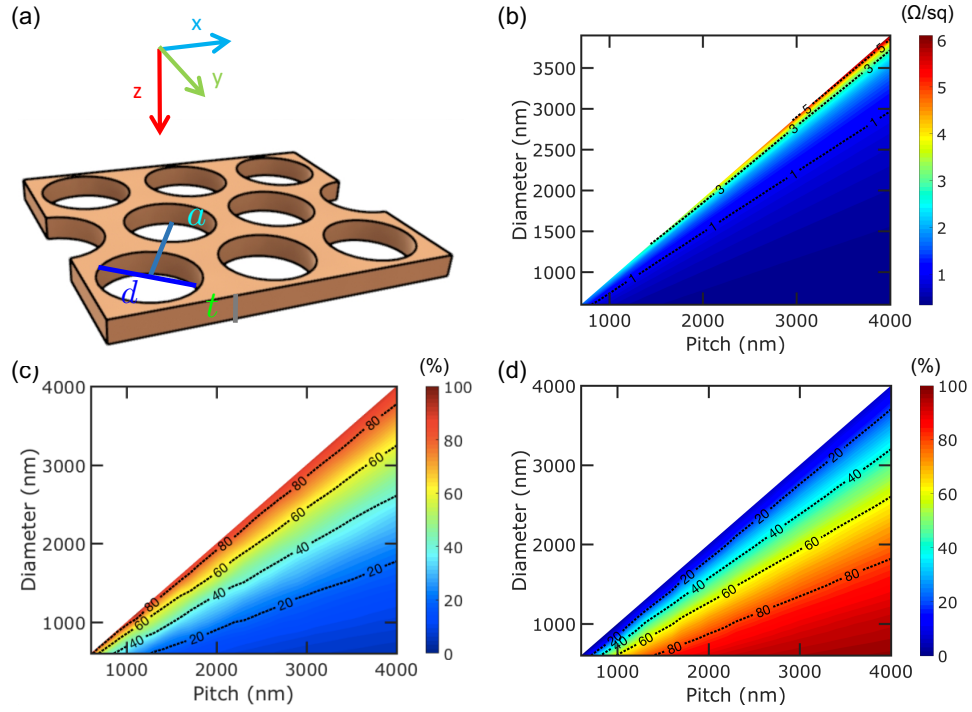


Figure 2 Simulated metal nanomesh properties. (a) Metal nanomesh schematic. The metal nanomesh is defined by pitch a , hole diameter d , and thickness t . Contour plots of (b) sheet resistance R_s of copper nanomeshes, (c) transmission T (at $\lambda = 550$ nm), and (d) haze H (at $\lambda = 550$ nm) as a function of pitch a and hole diameter d for thickness $t = 50$ nm.

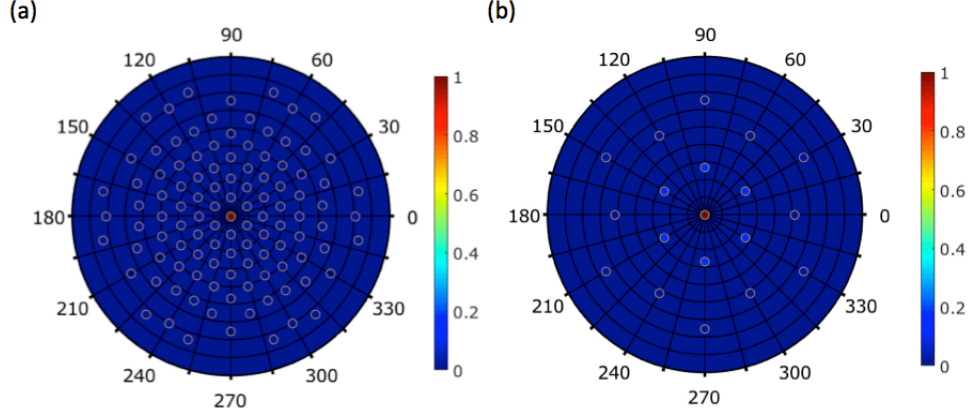


Figure 3 Diffraction patterns of different metal nanomeshes with (a) $a = 3500$ and $d = 3200$ nm and (b) $a = 1400$ and $d = 1200$ nm. The color scale shows light intensity normalized to the $(0, 0)$ order diffraction mode.

light, while the rest of the modes are considered forward scattered light. The haze calculated from this definition for the metal nanomeshes discussed in this paper is the same as the haze definition given by ASTM D1003, [26] where non-scattered forward light is considered as all transmitted light that deviates from the incident beam less than or equal to 2.5° , and scattered forward light is transmitted light that deviates from the incident beam greater than 2.5° ($\theta \leq 2.5^\circ$ and $\theta > 2.5^\circ$, respectively). Amongst all the Cu nanomeshes geometries in our study, the largest pitch is 4000 nm, corresponding to the lowest non- $(0, 0)$ light mode diffracting at about 9° from the incidence angle. The lowest non- $(0, 0)$ modes diffract at angles less than 2.5° only for $a = 14600$ nm at $\lambda = 550$ nm.

Figure 3 plots the diffraction patterns of two different nanomeshes where θ is plotted on the radius from 0° to 90° and ϕ is plotted as the angle from 0° to 360° . θ is the angle of deviation from the incident beam, which is the z -axis, and ϕ is the angle of rotation around the injection z -axis. Figure 3(a) plots the diffraction pattern of a nanomeshes with pitch $a = 3500$ and $d = 3200$ nm and (b) plots the diffraction pattern with pitch $a = 1400$ and $d = 1200$ nm. These two particular nanomeshes were fabricated experimentally, and their experimental characterization will be discussed later and compared with simulation results described here. For the nanomesh with pitch $a = 3500$ nm, there are 109 modes present

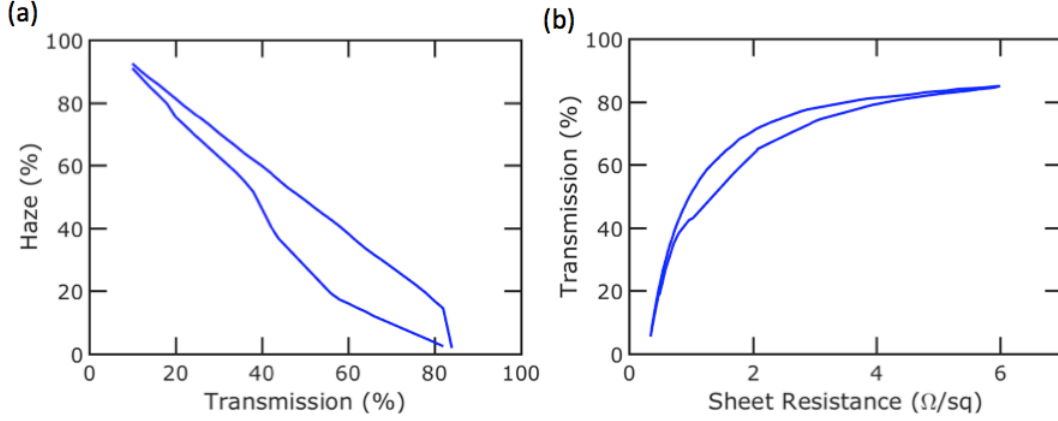


Figure 4 Performance limits of haze, transmission, and sheet resistance achievable in Cu nanomeshes of various hole diameters d and pitch a . The data shown is specifically for thickness $t = 50$ nm. (a) Range of haze and transmission achievable by varying diameter and pitch. (b) Range of transmission and sheet resistance.

due to the large pitch. Since the holes are large, the light is mainly diffracted into lower order modes. As mentioned earlier, the $(0, 0)$ diffraction mode is considered the forward non-scattered light, while the rest of the modes are considered forward scattered light. For this particular nanomesh, the analytical haze is 22% and from electrodynamic simulations, the transmission is 71% (compared to 76% from a geometrical shadowing calculation). Figure 4(b) plots the diffraction pattern of a metal nanomesh with pitch $a = 1400$ nm and diameter $d = 800$ nm. Due to the smaller pitch, there are only 19 modes present. Since the holes are small, the light is also strongly diffracted into higher order modes, such that the haze is high. The analytical haze is 49% and from electrodynamic simulations and the transmission is 41% (compared to 46% from just a geometrical shadowing calculation).

In order to study the correlation between transmission, haze and sheet resistance, we evaluated the range of values that are achievable by different nanomesh geometries. Figure 4 plots the envelope or the range of transmission, haze, and sheet resistance for the metal nanomeshes simulated (specifically, $600 \text{ nm} \leq a \leq 4000 \text{ nm}$ and $600 \text{ nm} \leq d \leq 4000 \text{ nm}$ with $d < a$ and $t = 50 \text{ nm}$). For different thicknesses above $t \geq 30 \text{ nm}$, the haze and transmission should be about the same as those shown, since the Cu regions are

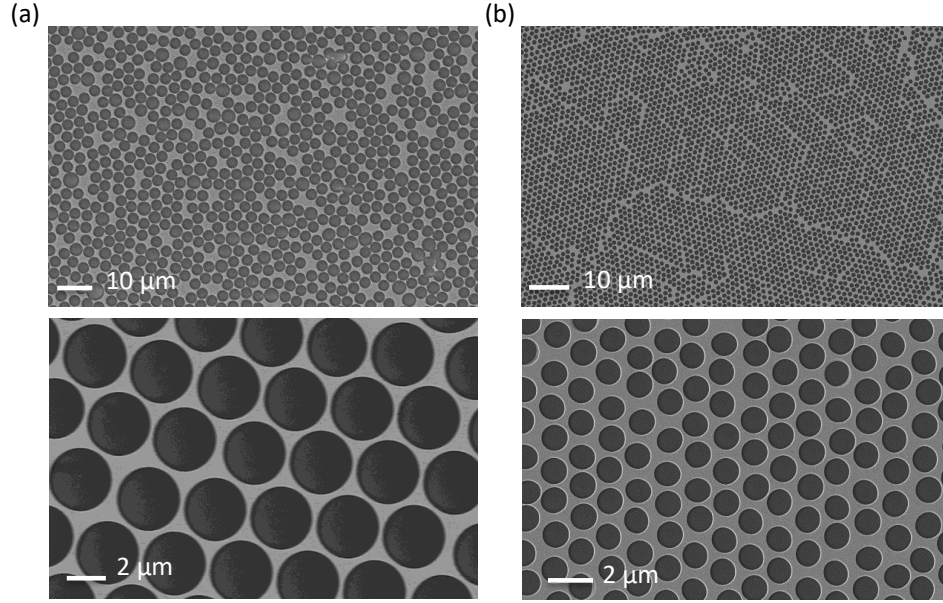


Figure 5 SEM pictures of Cu NMs with different geometries fabricated using microsphere lithography. (a) $a = 3500$ nm, $d = 3200$ nm and (b) $a = 1400$ nm, $d = 1000$ nm. The thickness is 50 nm for both.

essentially opaque, and for increasing thicknesses, the sheet resistance should decrease linearly. Figure 4(a) plots the range of transmission and haze (at $\lambda = 550$ nm). As can be seen from this plot, the transmission and haze show a strong and nearly linear correlation with each other. Nanomeshes with transmission $\geq 80\%$ have $H \leq 17\%$ and nanomeshes with $H \geq 80\%$ have transmission $\leq 21\%$. Figure 4(b) shows the range of sheet resistances and transmissions that are achievable. Cu nanomeshes with a higher transmission tend to have a higher sheet resistance, but increasing the thickness of the metal nanomesh may be utilized to decrease the sheet resistance without significantly sacrificing transmission. In addition, a variety of hierarchical structures have been reported to dramatically decrease sheet resistance and only slightly affect transmission.[79, 48, 45]

We next studied the haze and transmission properties of various experimentally fabricated metal nanomeshes and compare them with simulation results. Cu nanomeshes of a variety of pitches and hole diameters with thickness $t = 50$ nm were fabricated by microsphere lithography.[49] Figure 5 shows scanning electron microscope (SEM) pictures of two representative Cu nanomeshes. The nanomeshes pictured have (a) $a = 3500$ and

$d = 3200$ nm and (b) $a = 1400$ and $d = 1000$ nm, which are the same metal nanomeshes discussed specifically in simulations (Fig. 3). We found that it is more difficult to fabricate larger pitch ($a = 3500$ nm) nanomeshes with high uniformity and ordering, because larger microspheres tend to have larger variance in diameter. The optical transmission was measured using a PerkinElmer Lambda 750 spectrophotometer. The transmission was measured with an integrating sphere, while the direct transmission was measured with a 2D optical detector. The transmission for the samples shown in Fig. 5(a) and (b) are 80% and 45%, respectively at $\lambda = 550$ nm, compared with 71% and 41% from simulations discussed earlier. The hazes are 17% and 36%, respectively, at 550 nm (compared to 22% and 49%, respectively, from theory) and the sheet resistances are 20 and 1.5 Ω/sq , respectively (compared to 2.6 and 0.9 Ω/sq , respectively, from simulations). The larger difference in sheet resistance for the 3500 nm pitch nanomeshes may result from assumptions of bulk resistivity and some of the nonuniformity in experimental fabrication.

We next compared the angular distribution of the transmission through these copper nanomeshes with analytical calculations. The angular distribution of transmission through the Cu nanomeshes was measured using a universal spectrometer (Cary 7000 Universal Measurement Spectrophotometer) with a 5 mm by 5 mm square beam at $\lambda = 550$ nm (Figure 6). The photodetector receives light in a 6-degree cone so that there is substantial broadening on the light intensities measured and the haze calculated directly from these plots has different values from that measured with an integrating sphere. The angular distribution was measured at two azimuthal angles, $\phi = 0^\circ$ and 180° , at varying zenith angle, $\theta = 0^\circ$ to 90° to account for all transmission angles. Since the fabricated metal nanomeshes consist of various grains where the individual crystallites are oriented randomly, the diffraction modes are averaged over all ϕ and thus, may still be observed. In addition to experimental data, we also plot the analytical solution for the metal nanomeshes assuming the size of the hole array is 5 by 5 in the case of the (a) larger pitch metal nanomesh and 9 by 9 in the case of the (b) smaller pitch metal nanomesh. The analytical data is also smoothed with a Gaussian kernel with a bandwidth of 3° to account for the photodetector receiving light over a 6-degree cone. As can be seen in Figure 6, the experimental and analytical data match well. While the larger metal nanomesh consists

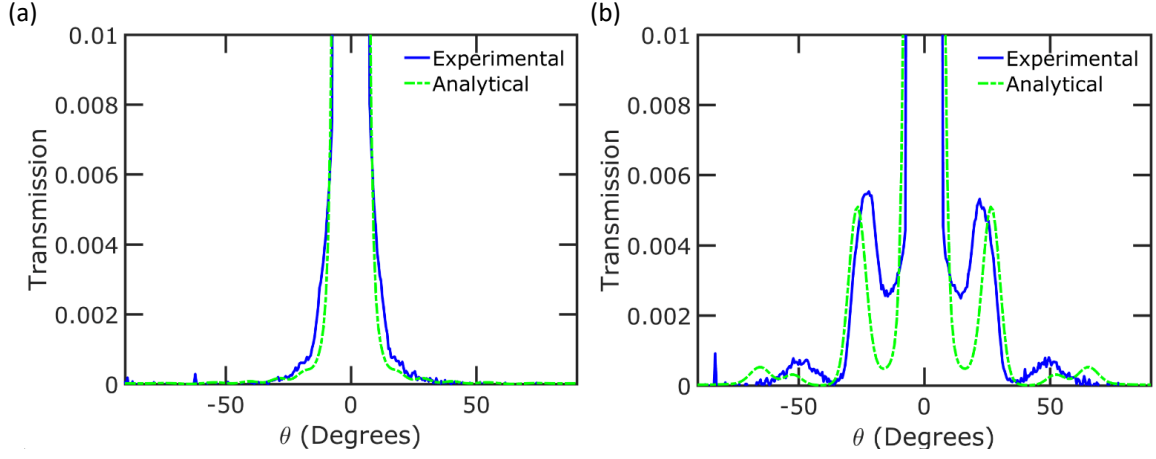


Figure 6 Angular distribution of transmission through the Cu NMs pictured in Figure 4. (a) $a = 3500$ nm, $d = 3200$ nm and (b) $a = 1400$ nm, $d = 1000$ nm. The thickness is 50 nm for both.

of many diffraction modes, most of the light is transmitted straight through into the (0, 0) mode. Since the higher modes are closely spaced together in angle and averaged over all azimuthal angles, the individual peaks are not observable. In contrast, for the smaller pitch metal nanomesh, the higher order diffraction modes can be observed. The experimental measured data appears to have broader higher order modes due to imperfections in the nanomesh crystal lattice (different sized holes, hole not being perfectly circular, off lattice site holes, etc.). The hole spacing can be estimated from the width of the first-order diffraction modes using Bragg's law for a 2D hexagonal hole array. The first-order diffraction, i.e. first-order Debye ring, takes place when:

$$a = \frac{2 \times \lambda}{\sqrt{3} \times \sin(\theta)} \quad (2.2)$$

The maximum and minimum θ within the Debye ring correspond to the minimum and maximum of hole spacing a . The range of diffraction angle θ is obtained by peak fit. In Figure 6(b), the center of the peak is at 23° and the full width at half maximum (FWHM) is 6.7° , with the 6° instrumental broadening subtracted. Therefore, the hole spacing is estimated to be ranging from 1430 nm to 1890 nm. The estimate is a result of the sum of all the aforementioned imperfection types.

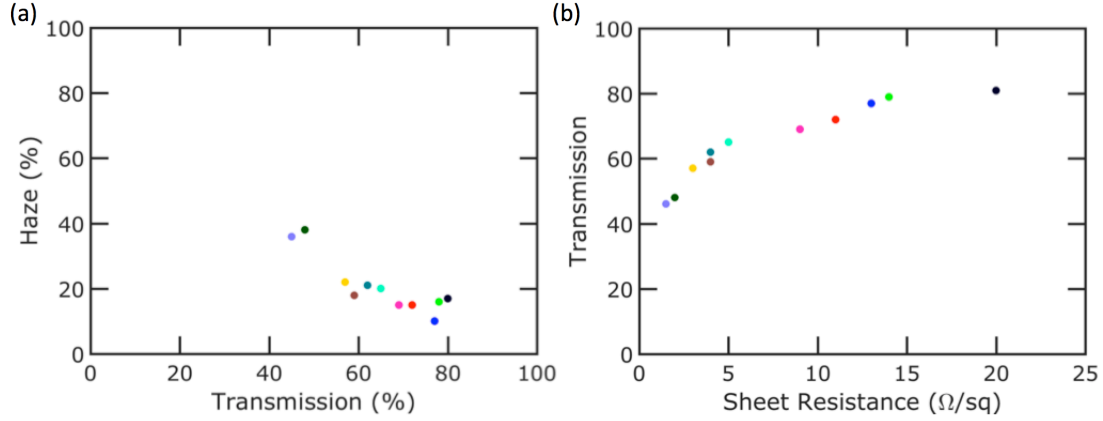


Figure 7 Range of (a) transmission and haze, and (b) sheet resistance and transmission from the fabricated Cu NM samples.

Figure 7(a) shows the transmission and haze of all our fabricated Cu nanomeshes. By varying the pitch and hole diameter of the Cu nanomeshes, a variety of hazes ranging from 17% to 36%, and transmissions corresponding to 80% to 45% were measured. The experimentally measured values and correlation match well with the computational results in Fig. 4(a). Smaller hole diameters are required by the Cu nanomeshes for a higher haze, which in turn compromise the transmission due to higher reflection and higher absorption. Figure 7(b) shows the sheet resistance and transmission of the fabricated nanomeshes. Cu nanomeshes with 80% transmission at 20 Ω/sq is demonstrated, which is comparable to ITO. Similar to the simulation results shown in Fig. 4(b), there is also a tradeoff between sheet resistance and transmission in the experimental data. The fabricated Cu NMs exhibit higher sheet resistance than the simulation results at a fixed transmission, because our simulations assume bulk resistivity, ignore surface scattering, and assume ideal geometry.

Finally, we studied the transmission and haze as a function of wavelength. Figure 8 shows the experimental and simulation results of (a) transmission and (b) haze as a function of wavelength for the same geometry nanomeshes that we have been discussing. The experimentally fabricated Cu NMs have flatter transmission spectra compared with the simulation results because of their less perfect periodicity. The calculated haze spectra match the experimental results reasonably well for both geometries. The theoretical haze

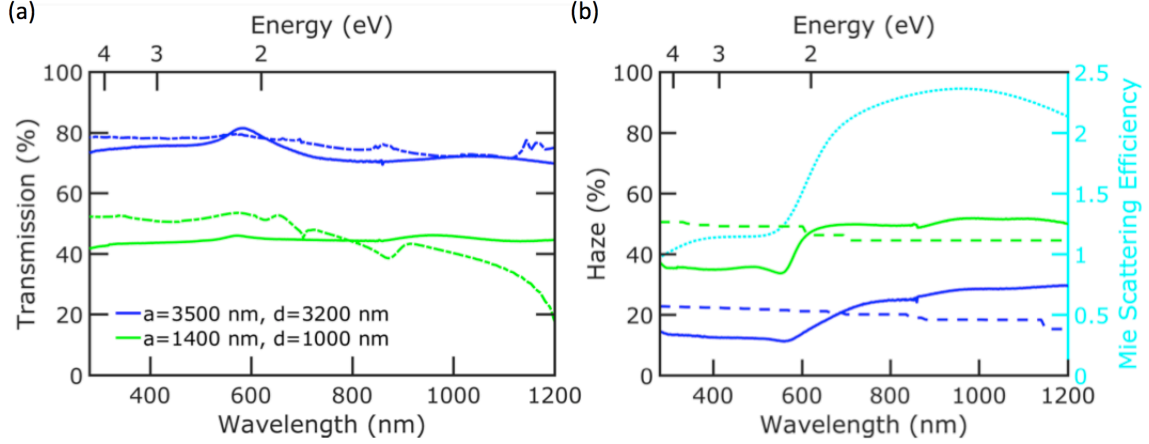


Figure 8 (a) Transmission and (b) haze as a function of wavelength for Cu nanomeshes with pitch $a = 1400$, diameter $d = 1000$ nm, and $a = 3500$ nm, $d = 3200$ nm. The thickness is 50 nm for both nanomeshes. Experimental results are shown with solid lines and theoretical results are shown with dashed lines. The scattering efficiency of a single Cu nanowire with thickness $t = 50$ nm and width $w = 400$ nm is shown on the right y -axis in cyan.

spectra decreases monotonically with increasing wavelength, as the number of diffraction modes decreases with increasing wavelength. For example, the large pitch ($a = 3500$ nm) nanomesh has 433 diffraction modes at $\lambda = 280$ nm and 19 at $\lambda = 1200$ nm and the smaller pitch ($a = 1400$ nm) nanomesh has 61 diffraction modes at $\lambda = 280$ nm and 7 at $\lambda = 1200$ nm. With less modes at larger wavelengths, more of the light intensity is concentrated in the $(0,0)$ non-scattered mode, and thus the haze decreases. However, the experimentally measured haze tends to be lower at smaller wavelengths. This discrepancy may be explained by Mie scattering from the metal regions between the holes. Figure 8(b) shows the Mie scattering efficiency of a single freestanding Cu nanowire with rectangular cross section, with thickness $t = 50$ nm, width $w = 400$ nm. This efficiency was calculated by the finite-difference time-domain method using a total-field scattered-field source to detect the scattered power flux.

The Mie scattering efficiency of a Cu nanowire is defined as the ratio of the scattering cross section and the width of the nanowire w , where the scattering cross section is the energy flux removed from the incident light due to scattering. Mie scattering efficiency

of Cu nanowire for incident light with electric field vector parallel and perpendicular to the nanowire was calculated respectively and averaged. As can be seen from the plot, this geometry has a lower Mie scattering efficiency at wavelengths shorter than 550 nm.

2.3 Conclusions

In conclusion, we report both simulation and experimental results on transmission, sheet resistance, and haze of Cu nanomeshes. Simulations and theoretical calculations were used to comprehensively evaluate the transmission, haze, and sheet resistance of metal NM structures, shedding light on the performance limits and correlation of metal nanomeshes as transparent conductors. Experimentally, we fabricated a variety of Cu nanomeshes to verify simulation results. The experimental results verifies the correlation between haze and transmission. The haze may be primarily explained by Fraunhofer diffraction, though there are some Mie scattering effects from the metal region between holes. Future work will be devoted to breaking this correlation by introducing additional light scattering elements to the Cu nanomesh.

3.0 High Transparency, High Haze Optoelectronic Substrates

In this chapter, we will review our recent works on high transparency high haze optoelectronic substrates including glass[64] and plastics[69].

3.1 High Transparency, Ultrahigh Haze Nanograss Glass with Fluid-Induced Switchable Haze

3.1.1 Introduction

Glass substrates form a critical component in many optoelectronic devices, such as displays, lighting, solar cells, smart phones, tablets, and e-paper, where the glass must protect the device from the ambient environment and allow light to pass through and couple into or out of the active layers of the device. Typically, glass has a quarter-wave thickness antireflection layer coating in order to reduce reflection losses at the air/glass interface [195]. In addition to these functionalities, many optoelectronic applications such as solar cells [135, 186], backlit liquid crystal displays [178], and light emitting diodes (LEDs) [97, 102] would benefit from glass substrates with both high transparency and high haze. Substrates with high haze can increase how much light scatters into or out of the underlying photoactive layers [211] and may increase the solar cell power conversion efficiency or LED extraction efficiency, respectively. For example, Fang *et al.* recently introduced a transparent paper fabricated using wood fibers that possesses both ultrahigh transmission (96%) and high haze (60%), and showed that this paper can increase solar cell efficiency [34]. Finally, optical switchability is desired in a variety of smart glass window applications, where this functionality may be utilized to affect temperature, comfort, and privacy [21, 59, 57]. A variety of active approaches such as electrochromism [25, 154, 214] and liquid crystal alignment [99, 152] have been demonstrated for optical switchability, though these approaches still face many technological and economic barriers to widespread adop-

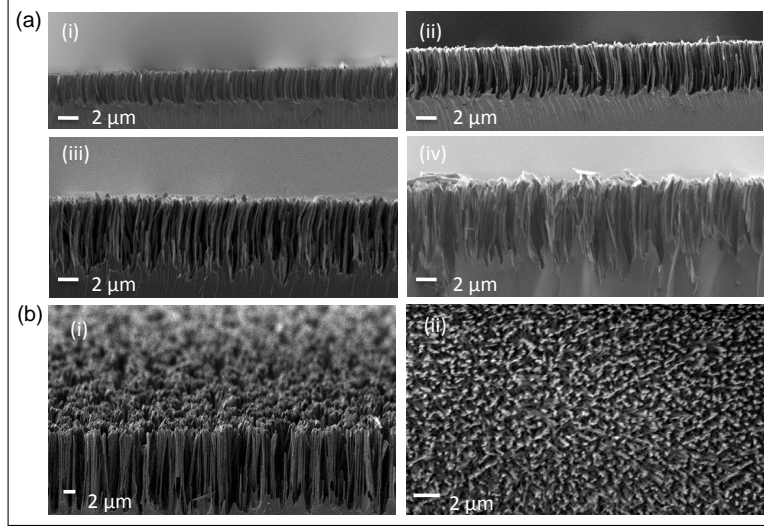


Figure 9 (a) Cross section SEM images of nanostructured grass-like glass with (i) 2.5, (ii) 4.5, (iii) 6, and (iv) 8.5 μm height and (b) (i) 15 $^\circ$ tilted and (ii) overhead view of 6 μm height hazy glass.

tion. In this section, we demonstrate monolithic fused silica nanoglass glass with both ultrahigh transparency and ultrahigh haze (both over 95% at 550 nm wavelength). The nanoglass may be fabricated through a scalable maskless, one-step reactive ion etching (RIE) process on fused silica glass where the height may be controlled through the etch time. We demonstrate that shorter grass ($< 2.5 \mu\text{m}$) improves the antireflection properties of the glass, but the antireflection decreases at longer heights due to increased scattered (or diffuse) reflectance. In contrast, longer grass tends to monotonically increase the haze. Finally, we demonstrate that the nanoglass glass is superhydrophilic. Various fluids with a similar index of refraction as the glass may be utilized to permeate the nanoglass, such that it resembles a uniform flat glass substrate with little haze. Upon removal of this fluid, the nanoglass recovers its original hazy state.

3.1.2 Results and Discussion

Figure 9 shows SEM images of the sub-wavelength nanoglass glass. The nanoglass is fabricated by a maskless RIE fabrication process (Trion Technology Phantom III) [212].

The fused silica is etched by CHF_3 , SF_6 and Ar at 40, 10 and 85 sccm, respectively. The total pressure of chamber was kept at 200 mTorr and the power was 300 W. During the etching process, polymer particles are deposited on the surface of the fused silica substrate, which acts as a micro-mask and allows the etching to create the high aspect-ratio nanoglass [145]. Seven different glass substrates were etched for 20, 80, 100, 150, 200, 300 and 450 minutes, yielding nanoglass with heights of 0.8, 2.5, 3.3, 4.5, 5.2, 6.0, and 8.5 μm , respectively. Figure 9(a) shows cross-section SEM images of the (i) 2.5, (ii) 4.5, (iii) 6, and (iv) 8.5 μm height nanoglass. The etch rate is approximately 16 nm/min for a several cm^2 area, 500 μm thick chip. Figure 9(b)(i) and (ii) show 15° tilted and overhead view SEM images of the 6 μm nanoglass glass, respectively. The diameter of each grass blade is roughly 100 - 200 nm and the distance between adjacent grass blades is approximately 100 to 700 nm. The surface is etched uniformly over the entire glass substrate.

The total and direct (or specular) transmission of all nanoglass samples as well as smooth glass were measured using a UV-vis-NIR spectrophotometer (PerkinElmer, Lambda 750) with and without an integrating sphere, respectively. Figure 10 plots the contour of (a) total transmission and (b) haze factor spectra of different height nanoglass glass ranging in height from 0 to 8.5 μm over wavelengths 250 to 1200 nm. For the entire spectrum, the smooth glass has a haze of less than 2.5% and a total transmission of about 93.5%. For the 2.5 μm height nanoglass, the transmission spectra remains fairly flat and improves over that of the smooth glass. However, as the nanoglass continues to increase in height, the total transmission tends to decrease, particularly more at shorter wavelengths. In contrast, the haze tends to decrease at longer wavelengths. The scattering of near infrared photons (wavelength 750 to 1110 nm) would benefit thin silicon solar cells by scattering light into the silicon [70, 233]. The high haze nanoglass may help to overcome silicon's low absorption near its band gap energy.

Next, we focus our discussion on how the nanoglass height affects the transmission and haze of 550 nm wavelength light, which is the average wavelength of visible light. Figure 11 plots the results of the total transmission and haze at this wavelength as a function of nanoglass height. Smooth glass has a transmission of 93.5%. Low height nanoglass increases the transmission due to improved antireflection. We find a maximum

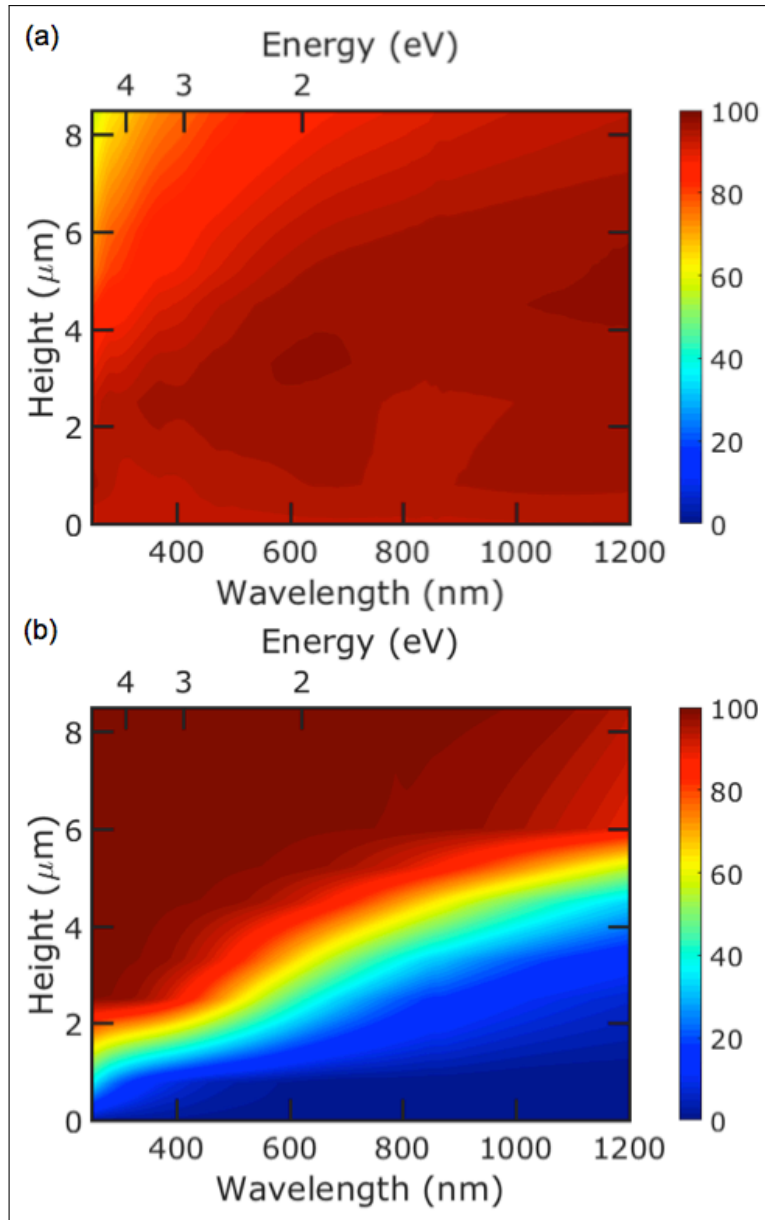


Figure 10 Contour plots of (a) total transmission (%) and (b) haze (%) as a function of wavelength and nanograss height.

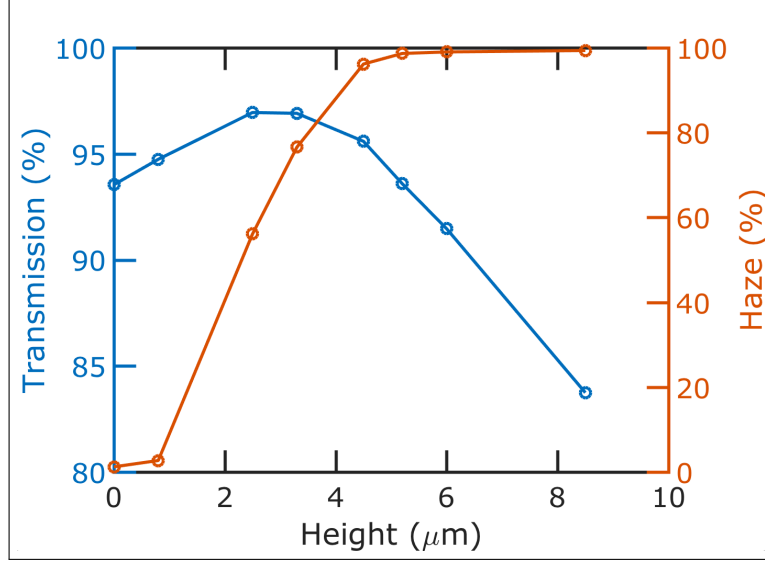


Figure 11 Plots of total transmission (left y-axis) and haze (right y-axis) at 550 nm wavelength as a function of nanoglass height.

transmission of 97.0% for 2.5 μm height nanoglass. The transmission decreases at larger heights due to increased scattered (or diffuse) reflection. In contrast, the haze increases monotonically with increasing height as the scattering probability of the light increases. While the smooth glass has a haze of only 0.8%, this haze increases to 1.7% for 0.8 μm nanoglass, and haze factors over 99% may be achieved with nanoglass above 6 μm height.

To explain our haze results, we compare our results with the haze predicted from scalar scattering theory of a single rough surface where the height of the surface has a Gaussian distribution [165, 14]. According to this theory, the wavelength dependent haze at normal angle of incidence is

$$H(\lambda) = \left(1 - \exp \left[- \left(\frac{2\pi\sigma_{rms}[n_1 - n_2(\lambda)]}{\lambda} \right)^2 \right] \right) \times 100\% \quad (3.1)$$

where root mean square roughness of surface and the refractive indices of the two media on either side of the interface are represented by σ_{rms} , n_1 and $n_2(\lambda)$, respectively. In our case, $n_1 = 1$ for air and n_2 varies from 1.51 at 250 nm to 1.45 at 1200 nm for fused silica [113]). This theory assumes that the surface correlation length is much larger than

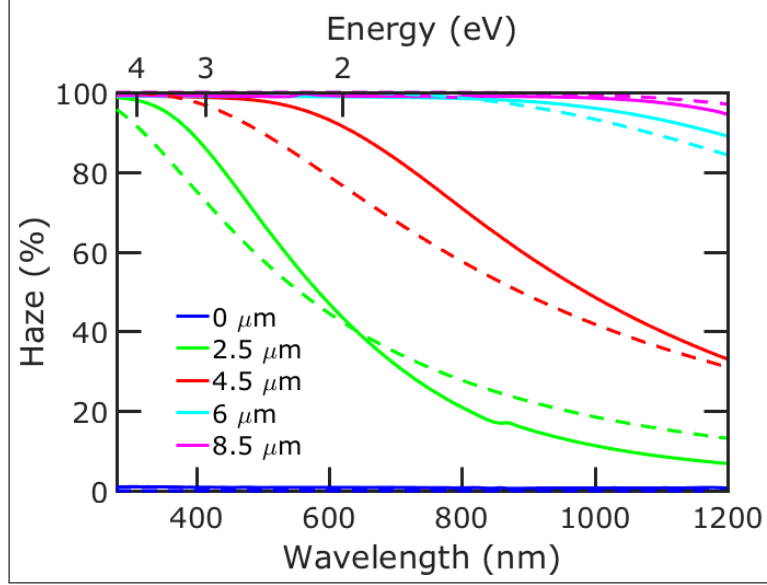


Figure 12 Experimental (solid lines) and scalar scattering theory (dashed lines) haze values for smooth and glass with 2.5, 4.5, 6, and 8.5 μm height nanoglass.

the root mean square roughness and does not consider multiple scattering. This equation has been used to model scattering in thin-film solar cells [221, 173, 155, 165]. Optical profilometry (Contour GT Bruker) was used to measure the root mean square roughnesses of the hazy glass. σ_{rms} equal to 160, 260, 580, and 800 nm were measured for the hazy glass with heights of 2.5, 4.5, 6, and 8.5 μm , respectively. Figure 12 plots our experimental haze results compared to that predicted from (3.1). The scalar scattering theory results match well with experimental results, though some differences are seen due to the lack of considering multiple scattering from surfaces in the theory.

Figure 13 shows optical images of smooth fused silica and fused silica with various height nanoglass when the substrate is (a) placed directly on top of text and (b) placed about 1 cm above the text. When the substrate is placed directly on the text, the differences in visible transmission of the various samples is apparent. When the substrate is held about 1 cm above the text, the increasing haze with increasing height can be observed. Even though the 6 μm height nanoglass glass looks opaque, in fact, it is only the direct transmission that is low; Its total transmission is 91.5% at 550 nm.

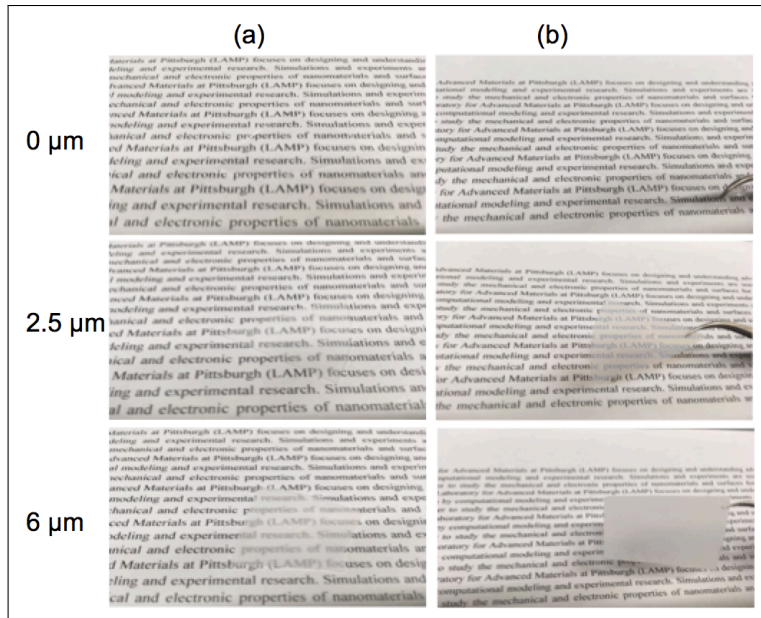


Figure 13 Optical images smooth and with 2.5, and 6, μm height nanograss glass when (a) place directly on paper with text and (b) about 1 cm above.

The scattering of light is shown in Fig. 14. A green laser beam with a wavelength 532 nm was used to visualize the light scattering ability of the (a) flat fused silica and (b) 6 μm height nanograss glass. The transmitted light passing through the flat fused silica shows a small luminous radius on the target with high intensity. The light scattering and haze of the flat fused silica is low. In contrast, for the 6 μm height nanograss, the light passing through the sample is almost completely scattered with no observation of a central point on the target. The distance between samples and target is 30 cm.

The smooth fused silica is hydrophilic. The static water contact angle (WCA) of flat fused silica is $46 \pm 1.5^\circ$ (Fig. 15a (i)). Due to the hydrophilicity of the surface, water easily fills the empty spaces between the blades of the grass and spreads across the surface. Nanostructures enhance the hydrophilicity or hydrophobicity of a surface when the wetting is in the Wenzel state [29]. For the 6 μm nanograss glass, the static WCA is $7 \pm 1.5^\circ$ (Fig. 15a (ii)). Consequently, since the refractive index of the water (1.33 at 550 nm [113]) is near that of the fused silica (1.46 at 550 nm [113]), the glass has low haze when it is wet by

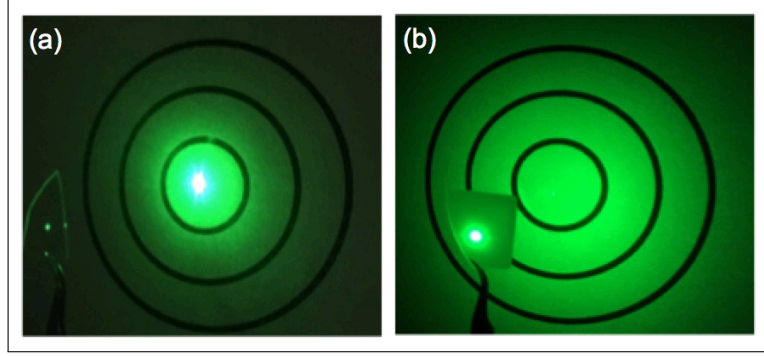


Figure 14 Scattering ability of (a) flat fused silica and (b) $6\ \mu\text{m}$ height nanoglass. The scattering ability is demonstrated by shining a laser through a sample onto a target. The rings on the target are spaced 15 cm apart. The distance between sample and target is 30 cm.

the liquid. Optical images are shown in Fig. 15(b) of the transition between transparent and haze modes of $6\ \mu\text{m}$ nanoglass which occurs when water is applied. When the surface is wet, the water fills the gaps and the glass has low haze (0 sec). As the water is removed (in this case, from evaporation), the haziness increases and after about 80 seconds, the glass returns to its original hazy state.

We characterize the transmission properties of the nanoglass glass when wet by different liquids, water, acetone and toluene, in the 350 to 850 nm wavelength range. The wavelength range is restricted to this range since the cuvette we used (FireflySci Type 523 Rectangular Absorption Cuvette) for characterization is designed for this wavelength range. The refractive indices of these fluids are 1.33, 1.36, and 1.50, respectively, compared to 1.46 for the fused silica at 550 nm wavelength [113]. Figure 16 plots the haze (left y-axis) and direct transmission (right y-axis) of the wet $6\ \mu\text{m}$ nanoglass glass for water and toluene. The direct transmission of $6\ \mu\text{m}$ hazy glass at 550 nm is 0.94% and its haze factor is 99%. When this glass is wet with water and toluene, the direct transmission at 550 nm wavelength increases to 44.3% and 61.5% respectively, while the haze decreases to 55.4 % and 38.3%, respectively. The total transmission also increases to near unity when it is wet.

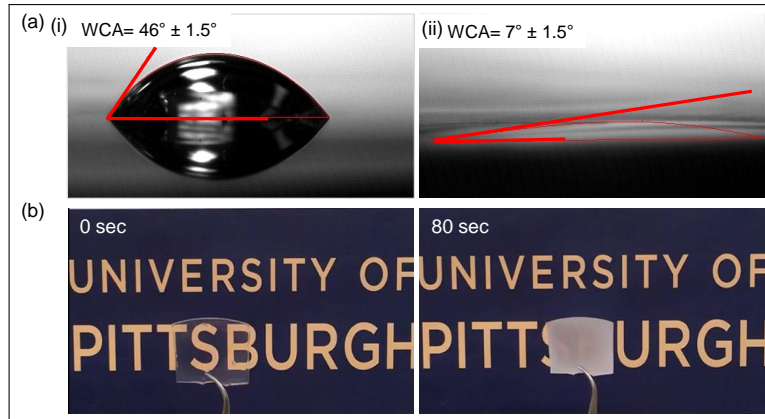


Figure 15 (a) Contact angle of water droplet on (i) smooth fused silica and (ii) 6 μm nanoglass (b) Transition between transparent and haze mode of 6 μm ultrahazy glass by putting water on the glass and evaporation in 80 seconds.

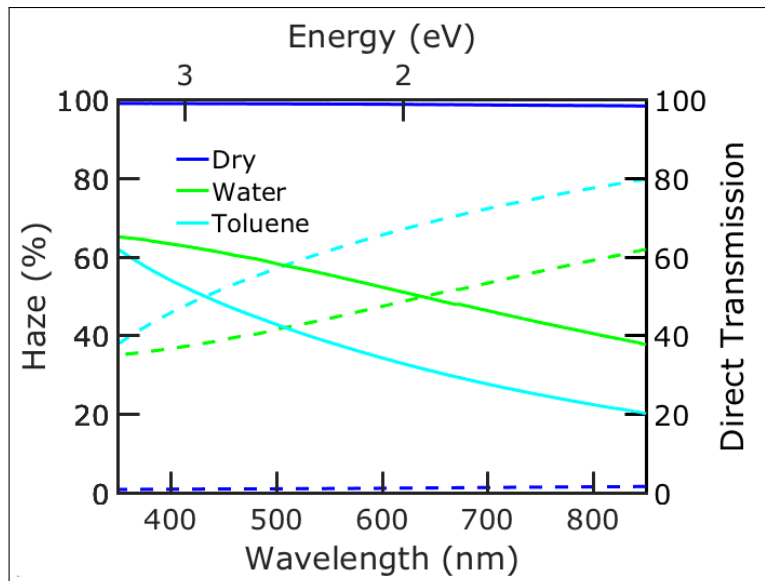


Figure 16 Haze (solid lines) and direct transmission (dashed lines) as a function of wavelength for 6 μm hazy glass in dry state and wet state with different liquids.

As the fluid infuses the nanograss glass, the optical properties more closely resemble that of a flat fused silica, where the haze is low. The nanograss glass can switch between low and high haze states within a few seconds with the application and removal of the fluid.

3.1.3 Conclusions

In conclusion, we report ultrahigh transmission, ultrahigh haze nanograss glass which has the ability to switch haze by applying fluid with a similar refraction index. The 4.5 μm height hazy glass showed 95.6% total transmission and 96.2% haze at 550 nm wavelength. These characteristics make the hazy glass a strong candidate to use in optoelectronic applications such as solar cells and LEDs, as well as switchable haze smart glass that may help adjust privacy, comfort, or temperature.

3.2 Flexible Nanograss With Highest Combination Of Transparency And Haze For Optoelectronic Plastic Substrates

3.2.1 Introduction

Flexible optoelectronics are emerging for a large variety of applications such as flexible versions of traditional rigid displays, smart phones, tablets, and e-paper, as well as new applications such as wearables, RF-ID tags, artificial skin, and the Internet of Things [211, 179]. Plastics are the most commonly used substrate for flexible optoelectronics due to their high transmittance [71, 136, 134]. The optical properties of the substrates are critical for optoelectronic applications as light needs to be coupled into or out of the active region of the device through the transparent substrates. Polyethylene terephthalate (PET), in particular, is often used due to its tolerance to temperature and resistance to solvents as well as high optical transmittance [220]. Various structures have been incorporated into PET substrates for different photon management strategies such as moth-eye-like films [179] and polyurethane acrylate nanostructures [224] for antireflection.

For flexible optoelectronic applications such as organic-light-emitting-diodes (OLEDs) [71, 136] and solar cells [134], substrates with both high transmittance and high haze are desirable as increased light scattering results in increased photon outcoupling or incoupling efficiency in these devices, respectively. Plastic-paper hybrids [211], silica nanoparticle arrays [218], and poly(methyl methacrylate)(PMMA)/PET [117, 118] have been demonstrated to increase the amount of light scattering. However, these PET substrates involve lithographic steps and/or the synthesis of nanomaterials that increase cost and complexity for fabrication. These nanostructures tend to increase haze while decreasing the transmission as there tends to be tradeoff between these two properties [44]. A combination of both transmission and haze over 90% (at 550 nm wavelength) has yet to be demonstrated in flexible PET substrates. Recently, we demonstrated nanoglass glass substrates [64]. In this section, we demonstrate flexible nanoglass PET substrates that may be fabricated through a scalable maskless, one-step reactive ion etching (RIE) process. These flexible substrates are monolithic and require no additional lithographic processes or synthesis of nanomaterials. These sub-wavelength nanostructures are able to simultaneously provide for antireflection and scattering such that both transparency and haze may be improved. While bare PET has a transparency and haze of 88.4% and 1.1% at 550 nm, respectively, our 9 μm height nanoglass samples demonstrate a transparency and haze of 92.4% and 89.4%, respectively. Our 34 μm tall nanoglass samples exhibit a transparency and haze of 91.0% and 97.1%, respectively. These nanostructured PET substrates demonstrate the highest combination of transparency and haze at 550 nm of all PET substrates in the literature. Our nanoglass samples displays a light scattering angle of 165° compared to 5° for planar PET. We also performed durability experiments that show these nanostructured PET substrates are robust from bending and maintain similar transmission and haze values after 5,000 cycles of bending.

3.2.2 Results and Discussion

Figure 17 shows the results of the fabrication process. Figure 17(a) displays schematic of the maskless RIE fabrication process (Trion Technology Phantom III). The PET substrate,

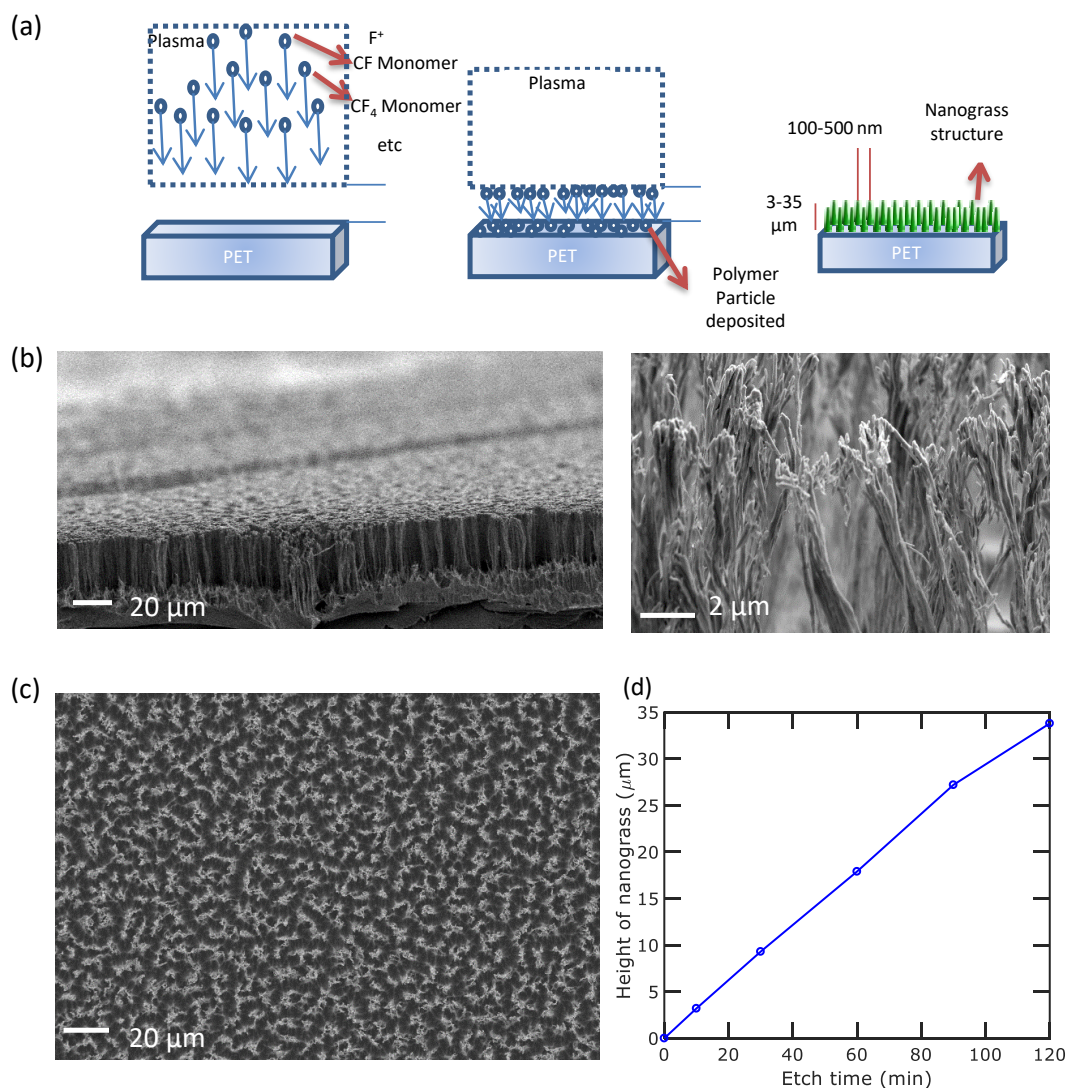


Figure 17 Fabrication of nanograin PET results. (a) Schematic of fabrication process. (b) Cross section SEM images of 34 μm nanograin PET. (c) Overhead SEM image, and (d) Height of nanograin PET as a function of etch time.

which is 125 μm thick, is etched by CF_4 and O_2 . The etch conditions were optimized to create high aspect-ratio grass-like nanostructures that maximize both transparency and haze. The CF_4 and O_2 flow rates are 45 and 5 sccm, respectively. The total pressure of the chamber is maintained at 150 mTorr and the power is set at 125 W. During the etching process, CF and CF_2 monomers form polymers that deposit on the PET [145]. These polymers act as a nano-mask that allows for the etching to create high-aspect ratio nanostructures.

Figure 17(b) shows cross-section SEM image of the nanograss PET. The nanograss shown here was etched for 120 minutes and is about 34 μm in height. The diameter of each nanograss blade is roughly 200-500 nm at the top and gradually decreases to approximately 50-100 nm at the bottom of the structures. Each blade of grass in the texture has a consistent height across the entire substrate. Figure 17(c) shows an overhead view SEM image of the hazy plastic. The distance between adjacent blades is approximately 100 to 700 nm and uniformly cover the entire substrate. Figure 17(d) plots the height of the nanograss as a function of etch time. The etch rate is approximately constant at about 300 nm/min based on a linear fit of the various etched samples.

The use of texturing increases the light scattering, thereby creating a PET substrate that exhibits both high haze and high transparency. Additionally, the sub-wavelength dimensions of the nanograss provides for a gradual change in effective index of refraction from the air to the PET substrate that provides for antireflection and thus, increased transparency. A UV-vis-NIR spectrophotometer (PerkinElmer, Lambda 1050) equipped with an 150 mm integrating sphere was used for measuring the total and direct (or specular) transmission of all nanograss PET samples as well as the bare PET. Figure 18 plots the (a) total transmission and (b) haze factor spectra for bare and different height nanograss PET over wavelengths 400 to 1050 nm. The nanograss is on the side facing the incident light.

The bare PET has a total transmission of about 88.5% and haze of less than 2.5% across the entire spectrum. The nanograss PET increases both the transmission and haze. For the 9 μm height nanograss PET, the transmission increases to 92.4% and haze to 89.4% at 550 nm wavelength. By increasing the height of nanograss to 18 μm , the transmission improves due to improved antireflection. In this case, the highest transmission of 93.0% is observed.

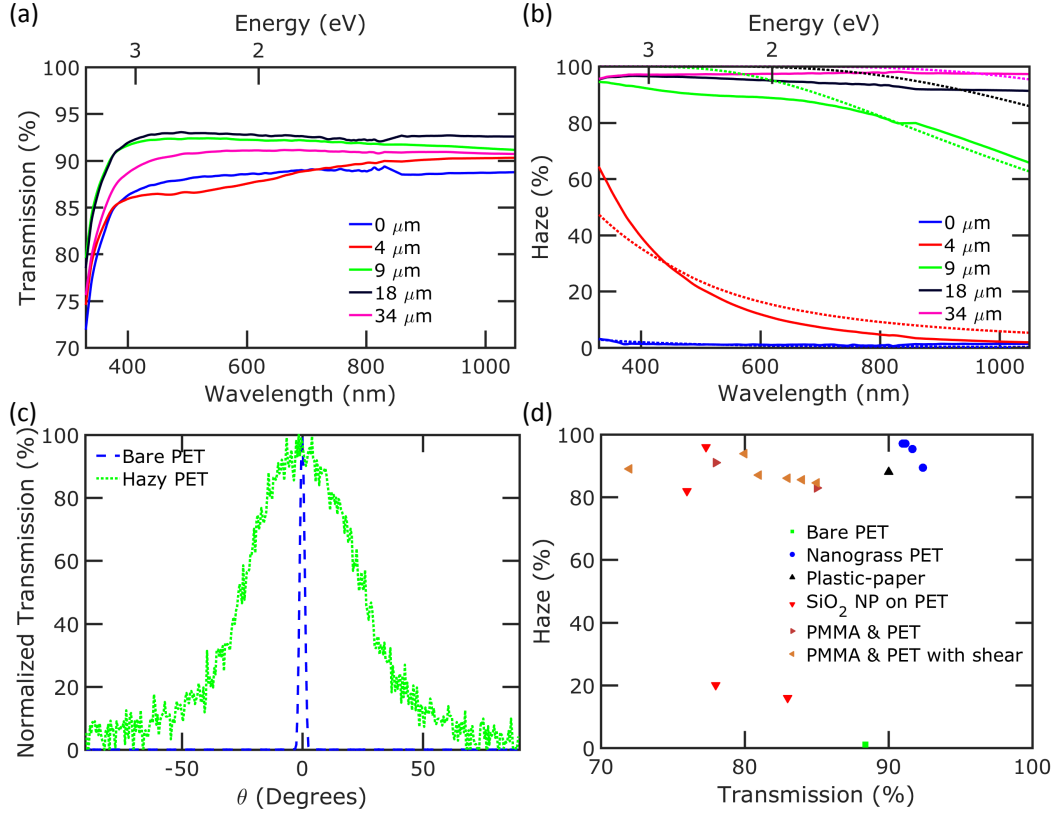


Figure 18 (a) Total transmission and (b) Experimental (solid lines) and scalar scattering theory (dashed lines) haze values for smooth and PET with 4, 9, 18, and 34 μm height nanoglass. (c) ADF plots of bare PET and nanostructured PET, etched for 120 mins. (d) Haze versus transmission for various PET substrates at $\lambda = 550$ nm. Bare PET is shown with a green square and our nanoglass PET samples are shown with blue circles. The best data for plastic-paper [211], silica nanoparticle array on PET [218] and doped poly(methyl methacrylate)(PMMA)/poly(ethylene terephthalate) (PET) without [117] and with shear [118] are also shown.

For longer nanoglass, the total transmission begins to decrease slightly. The transmission decreases at larger heights due to increased scattered (or diffuse) reflection. In contrast, the haze increases monotonically with increasing height as the scattering probability of the light increases. Beyond 27 μm though, this increase is very minimal.

The haze behavior of the nanoglass PET samples can be explained by scalar scattering theory of a single rough surface where the height of the surface has a Gaussian distribution [165, 14, 64]. Figure 18(b) plots our experimental haze results compared to that predicted from Equation (3.1) where σ_{rms} was treated as a fitting parameter. The fits were $\sigma_{rms} = 14, 68, 290, 410$, and 510 nm for the PET with heights of 0, 4, 9, 18, and 34 μm , respectively. The scalar scattering theory results match well with experimental results, though some differences are seen due to the lack of considering multiple scattering from surfaces in the theory, and shows that haze monotonically increases since the surface roughness also increases with increasing height based on Equation (3.1). This model also indicates that nanoglass exhibits dispersion effect that the larger wavelength the lower transmission.

It is demonstrated that by obtaining high haze values for long range of wavelengths the absorption of a solar cell improves, when the path length of scattered light also increase[34]. Therefore for effective light trapping, the haze value, by itself, is not a sufficient requirement and the angular distribution of scattered light also need to be measured. In order to measure the light scattering ability, we measured the angular distribution function (ADF) of both bare PET and the 34 μm height nanoglass PET as shown in Fig. 18(c). The scattering angular distribution was measured using a Cary 7000 Universal Measurement Spectrophotometer (UMS). In this instrument, incident light is normal to the sample surface with a 5 mm \times 5 mm square beam and the photodetector scans from 10° to 350° (-10°); the wavelength scan is from 530 to 570 nm and the wavelength of 550 nm is plotted. The photodetector receives light over a 6-degree cone and thus, the haze calculated from these plots is not exactly as the same as that measured previously. The scattering angle range is defined as the range of angles in which lights exhibits more than 5% of its highest measured intensity at 0°. As can be seen in Fig. 18(c), the bare PET has very small scattering angle, 5°, but this value for the 34 μm height nanoglass PET is 165°, which shows the light scattering ability of the nanostructured PET.

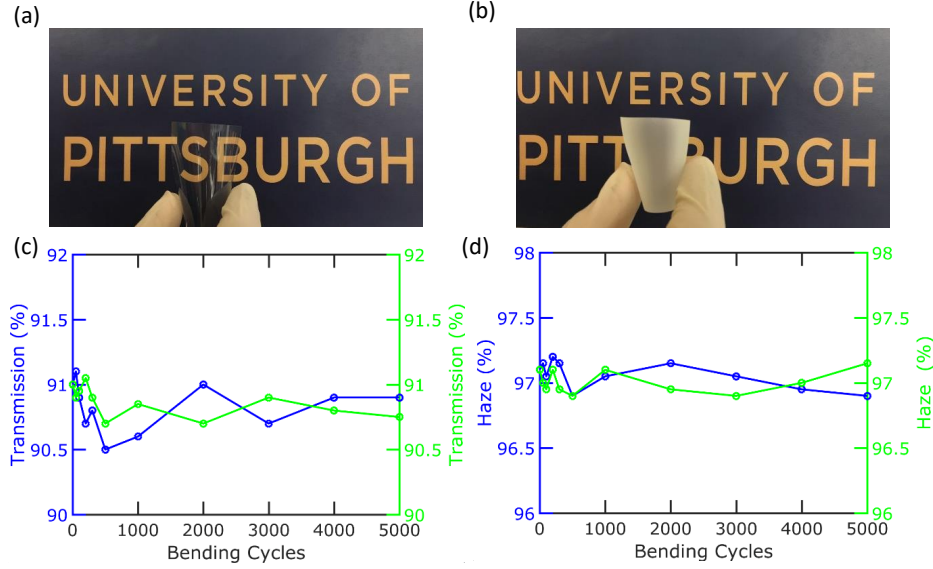


Figure 19 PET bending results. Optical images of (a) bare and (b) 120 min etched nanostructured flexible PET. (c) Transparency and (d) Haze at 550 nm as a function of bending cycle, for tension (left y axis) and compression (right y axis).

Figure 18(d) compares the combination of transmission and haze for our nanostructured PET and best high transparency, high haze PET reported in the literature so far, including plastic-paper flexible substrates [211], silica nanoparticle arrays on PET [218], and doped Poly(methyl methacrylate)(PMMA)/poly(ethylene terephthalate) (PET) without [117] and with shear [118]. All data shown in this plot is at a wavelength of 550 nm. Bare PET has a transmission and haze of 88.4 and 1.1%, respectively. The plastic-paper hybrid has a comparable transmission and much higher haze. Most of the other PET samples sacrifice transmission for an increase in haze. In contrast, our nanoglass PET exhibits both higher transmission and haze. Our nanoglass PET demonstrates the highest combination of transmission and haze of all plastic substrates. The 18 μm height nanoglass PET exhibits 93.0% transmission and 95.6% haze and the 34 μm height nanoglass PET displays 91.0% transmission and 97.1 % haze. In addition, our substrates are the only monolithic samples in the literature. The other PET substrates involve the other materials that need to be synthesized and then introduced into the PET.

Figure 19 plots bending experiment results of our PET. Optical images of both bare PET and 120 min etched nanostructured 34 μm height nanograss PET as the substrates are being bent are shown in Fig. 19a and b, respectively. The total transmission through the nanograss PET is in fact higher than that of the bare PET due to the antireflection properties of the nanograss. However, the letters through the substrate are completely blurred by the scattering of the light. Figure 19 plots the (c) transmission and (d) haze of the nanograss PET at 550 nm wavelength as a function of bending cycle under tension (left y axis) and compression (right y axis). Bending tests were conducted by bending the 34 μm height nanograss PET substrate around a stainless steel rod with a 1 inch diameter. The thickness of the PET substrate is 125 μm . Two samples with identical size, 3 cm \times 3 cm, were placed under bending compression and tension by bending the etched surface towards and away from the steel rod, respectively. Neither the transmission nor haze are changed significantly after 5000 cycles of bending, for either tension or compression. This suggests that the nanograss PET is robust under bending.

3.2.3 Conclusions

In conclusion, we demonstrate a new nanostructured PET that displays both high transparency and high light scattering ability. The 34 μm height PET showed 91.0% transmission and 97.1% haze at 550 nm wavelength, with 165° scattering angle range. The durability test showed that nanostructured PET substrates are robust from bending and show similar transmission and haze values after 5000 cycles of bending. The combination of flexibility, high transparency and high haze with extra large scattering angle range, makes the nanostructured PET as a strong candidates to use in flexible optoelectronic applications.

4.0 Superomniphobic Optical Substrate

In this chapter, we will review our works on multi-functional optoelectronic substrates. In first section, we review the self-cleaning glass with high haze and high transparency[65]. In the second section we review our work on superomniphobic optical PET[68].

4.1 Self-Cleaning, High Transmission, Near Unity Haze OTS/Silica Nanostructured Glass

4.1.1 Introduction

Optoelectronic substrates with high transmission and high light scattering are needed for optoelectronic applications such as solar cells and light emitting diodes (LEDs) where the substrate can increase how much light scatters into or out of the underlying photoactive layers, respectively[211, 44]. These substrates can enhance the power conversion efficiency of solar cells and extraction efficiency of LEDs. Various paper substrates have been demonstrated for optoelectronic applications including mesoporous wood cellulose paper[229], micro-sized wood fibers in paper[32], nanostructured paper[34], wood composites[231], and plastic-paper[211]. While paper may offer new functionality for optoelectronic applications such as flexibility, glass is most frequently used for optoelectronic devices due to its low cost and moisture barrier properties. High transparency, high haze glass substrates have included self-aggregated alumina nanowire arrays on glass[93], imprinted polydimethylsiloxane (PDMS) coatings on glass [22], and our recent nanoglass glass [64]. Optoelectronic substrates would also benefit from self-cleaning properties where particulates are easily removed from the surface upon application of water. Dust or dirt particulates may accumulate on the surface and reduce the transmission of light and can significantly reduce the power conversion and extraction efficiency of solar cells and LEDs, respectively [58, 12].

In this section, we report on self cleaning octadecyltrichlorosilane (OTS)/silica nanostructured glass which exhibits both high transparency and near unity haze. The OTS/silica nanostructures are synthesized by a facile maskless reactive ion etching method (MRIE) to create silica nanoglass blades followed by OTS coating. The OTS/silica nanostructured glass exhibits a transparency of $91.5 \pm 0.5\%$ with a haze value of $98.1 \pm 0.5\%$ at a wavelength of 550 nm. The OTS coating enhances the transparency of the nanoglass glass by as much as over 10% as the silica nanoglass blades merge together from capillary forces during coating and effectively grade the index of refraction between the air and the glass. Furthermore, the OTS coating does not significantly change the haze. The glass exhibits strong light scattering ability with a scattering angle of 143° . Our OTS/silica nanostructured glass demonstrates the highest combination of haze and transmission in the literature as defined by Pareto optimality.

The nanoglass glass is superhydrophilic initially with a water contact angle (WCA) of $7.4 \pm 0.2^\circ$. After coating, the OTS/silica nanostructures become superhydrophobic with a WCA of $159.7 \pm 0.6^\circ$ due to a combination of the nanostructures and low surface energy OTS. The OTS coated glass exhibits lotus leaf-like wetting with high WCA and $4.9 \pm 0.6^\circ$ contact angle hysteresis. We demonstrate the structures have self-cleaning functionality where about 100% of the original transparency can be easily recovered after graphite soiled substrates are rinsed with water. The original transparency and haze of the substrates are recovered after as many as 200 cycles of soiling and cleaning. The combination of optical properties and self-cleaning functionality make the nanostructured hazy glass an strong candidate for several optoelectronic applications.

4.1.2 Results and Discussion

Figure 20 shows details of the fabrication process and structure of the OTS/silica nanostructured glass. Figure 20(a) shows a schematic of the fabrication process. The fused silica substrate is etched by a maskless RIE process to create nanoglass glass [64] and then coated with OTS. Details of the fabrication process are provided in the Methods section. Figure 20(b) shows a 10° tilted cross SEM images of $8.5 \pm 0.2 \mu\text{m}$ initial

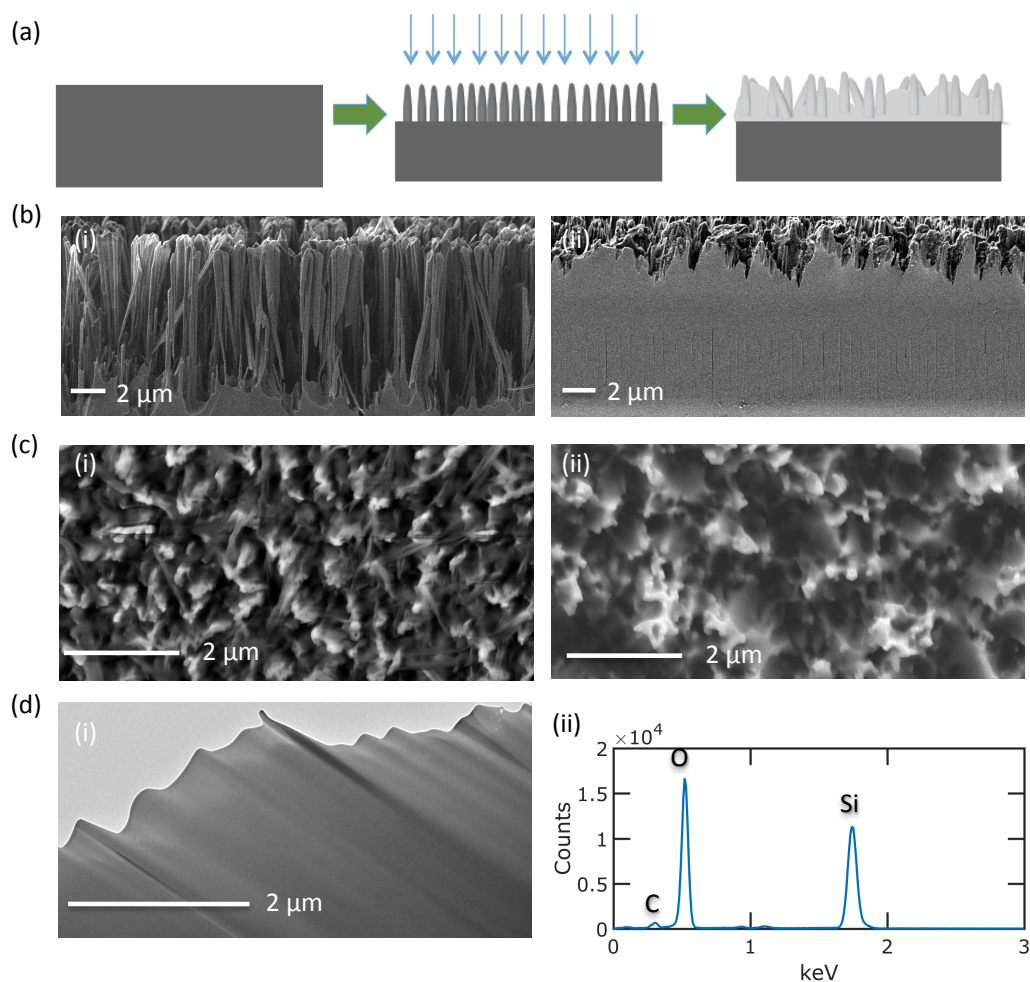


Figure 20 (a) Fabrication process of etching silica nanostructures with RIE followed by OTS coating. (b) 10° tilted cross section SEM images of $8.5 \pm 0.2 \mu\text{m}$ height hazy glass (i) before and (ii) after OTS modification. (c) Overhead SEM images of $8.5 \pm 0.2 \mu\text{m}$ height hazy glass (i) before and (ii) after OTS modification, (d) (i) TEM image and (ii) EDS spectrum of OTS coated hazy glass with $8.5 \pm 0.2 \mu\text{m}$ initial blade height.

height hazy glass (i) before and (ii) after OTS modification, respectively. While the initial structures are about $8.5 \pm 0.2 \mu\text{m}$ long, the OTS deposits in the space between nanoglass blades. In some cases where the nanoglass blades are close together, the drying process merges the blades together by capillary-induced bending [94, 93]. The final height of the structures after OTS coating is only about $2.2 \pm 0.2 \mu\text{m}$ long. Figure 20(c) shows overhead SEM images of $8.5 \pm 0.2 \mu\text{m}$ initial height hazy glass (i) before and (ii) after OTS modification, respectively. The reduced density of structures is apparent in these images as various nanoglass blades have merged together therefore the surface roughness slightly decreases. Figure 20(d)(i) shows a transmission electron microscopy (TEM) image of a selected area of the $8.5 \pm 0.2 \mu\text{m}$ initial height OTS coated hazy glass near the tips and Figure 20(d)(ii) plots the energy-dispersive x-ray spectroscopy (EDS) analysis of this selected area. After hydrolysis of the chlorine groups in the OTS, the molecules attach to the surface and polymerization takes place with elimination of water [180]. The final surfaces are terminated by methyl groups. The structures are primarily silica with some carbon from the carbon chains in the OTS. The small peaks near 0.9 keV and 1.1 keV correspond to the Cu La line and Na Ka line, respectively. The Cu and Na measurements come from the support grid and glass respectively.

Different height nanoglass glass were fabricated by varying the RIE time followed by OTS deposition. Figure 21(a) shows cross section SEM images of the OTS/silica nanostructured glass of different initial heights of (i) 2.5 ± 0.2 , (ii) 4.5 ± 0.2 , (iii) 5.2 ± 0.2 , and (iv) $8.5 \pm 0.2 \mu\text{m}$. After OTS deposition, the final height of the structures are about (i) 0.7 ± 0.2 , (ii) 0.9 ± 0.2 , (iii) 1.0 ± 0.2 , and (iv) $2.2 \pm 0.2 \mu\text{m}$ as the OTS fills the space between the nanostructures. All the measurement are the average and standard deviation of three different measurements in different cross sections of samples. Figure 21(b) shows a plot on the left y-axis of how the OTS thickness varies as a function of initial nanoglass height and on the right y-axis how the final structure height varies as a function of initial nanoglass height.

The optical properties of the various samples were subsequently characterized. The root mean square (RMS) of the surface roughness for different height hazy glass before and after OTS coating is shown in Figure 21(c).

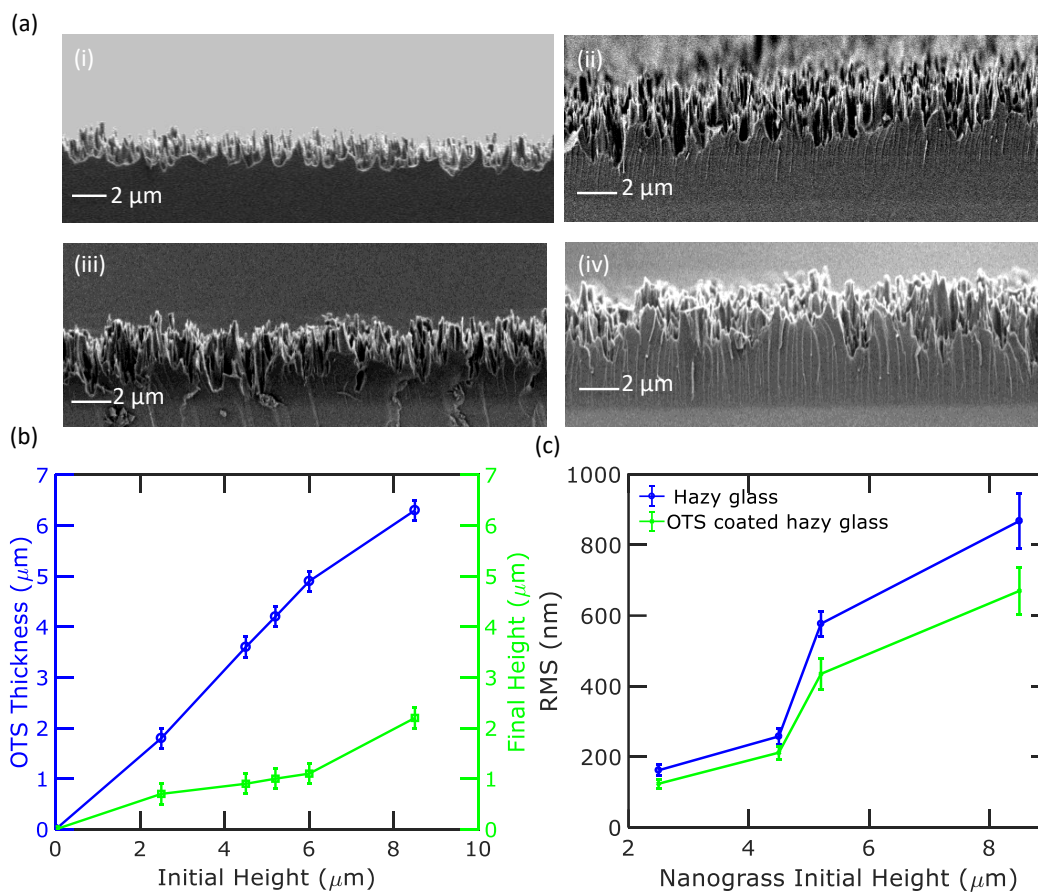


Figure 21 (a) Cross-section SEM images of hazy glass after OTS modification with initial and final blade heights of (i) 2.5 ± 0.2 and 0.7 ± 0.2 , (ii) 4.5 ± 0.2 and 0.9 ± 0.2 , (iii) 5.2 ± 0.2 and 1.0 ± 0.2 , and (iv) 8.5 ± 0.2 and 2.2 ± 0.2 μm . (b) Variation of the OTS thickness (left y-axis) and the final structure height (right y-axis) as a function of initial nanoglass height. (c) Change in root mean square (rms) roughness of different height hazy glass before and after OTS coating.

It is apparent that after OTS coating of hazy glass, the surface roughness slightly decrease for all initial heights due to merged blades together. Figure 22(a) shows the total transmission as a function of wavelength for the nanostructured hazy glass both (i) before and (ii) after OTS coating. Figure 22(b) shows the total transmission of the various structures at 550 nm wavelength. The transmission of bare fused silica is 93.2% both before and after OTS modification. On these surfaces, the OTS only forms a monolayer [180, 125, 138, 198] and has negligible change on the transmission of the original fused silica across the entire spectrum. For the $2.5 \pm 0.2 \mu\text{m}$ nanoglass glass, the transmission is initially $91.8 \pm 0.5\%$ at 550 nm wavelength. After OTS modification, the transmission increases to $92.4 \pm 0.5\%$. The improvements in transmission are primarily in the wavelengths under 600 nm. Nanoglass glass with initial heights $4.5 \pm 0.2 \mu\text{m}$ and above (final height over $0.9 \pm 0.2 \mu\text{m}$) demonstrate an improvement in transparency across the entire spectrum after OTS coating compared to before. The enhancement in transmission from the OTS coating is shown in Fig. 22(c) and over $8.0 \pm 0.5\%$ at a initial silica nanostructure height of $5.2 \pm 0.2 \mu\text{m}$ and longer (final OTS/silica height over $1.0 \pm 0.2 \mu\text{m}$). This improvement in enhancement is primarily due to the merging of nanoglass blades. While the initial blades are structures of constant diameter, after OTS deposition, structures that are close together are merged together. These sub-wavelength structures effectively grade the index of refraction of the glass such that the antireflection and thus, transmission properties are improved.

Next, we characterized the haze factor of the original nanoglass glass and compared it with the OTS/silica nanostructured glass. Figure 23(a) plots the haze of (i) the original nanoglass glass, and (ii) the OTS/silica core-shell nanoglass glass. The haze in the silica/OTS core-shell nanoglass glass increases monotonically with height similar to that of just the silica nanoglass glass, and the haze does not change much prior to and after OTS coating. The haze is near unity at wavelengths in the ultraviolet and visible, though the haze does start to drop slightly in the near-infrared.

We next characterized the angular distribution of the transmission through various substrates. Figure 23(b) shows the scattering angular distribution of transmission at a wavelength of 550 nm for (i) bare glass before and after OTS modification and (ii) 5.2 ± 0.2

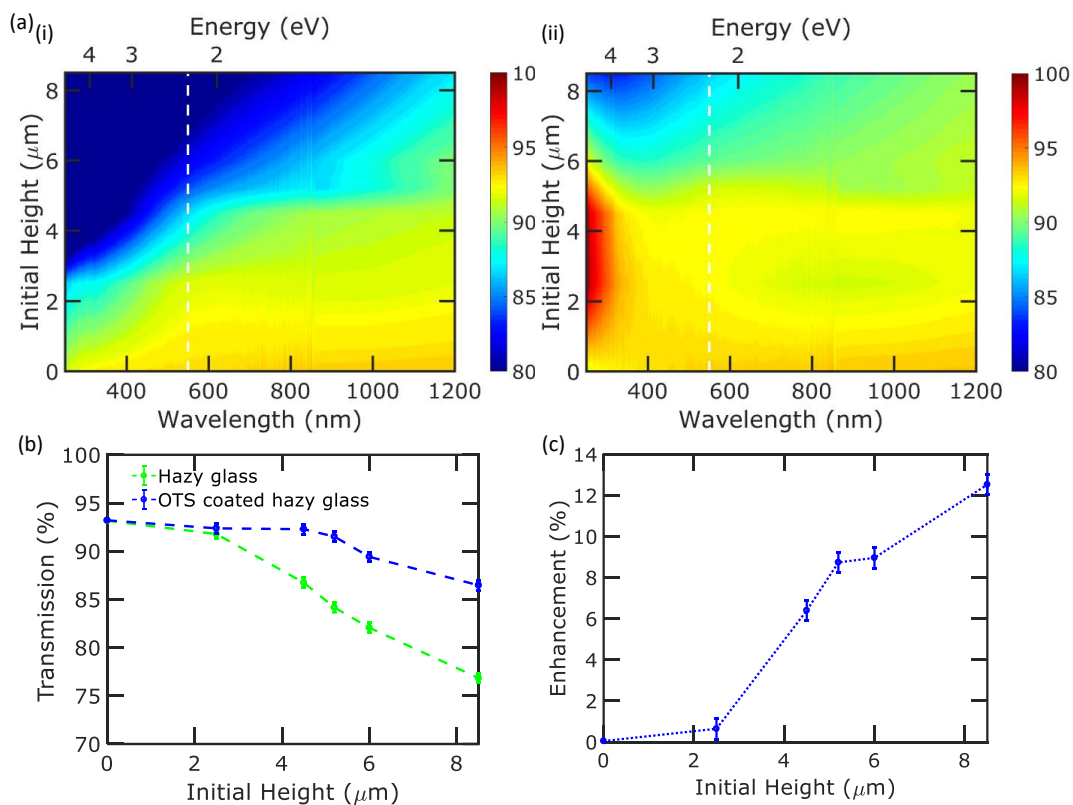


Figure 22 Contour plots of (a) total transmission (%) (i) of nanoglass glass (ii) and core/shell silica/OTS nanoglass glass. (b) Plot of total transmission at 550 nm wavelength as a function of initial blade height. (c) Enhancement in transmission after OTS coating.

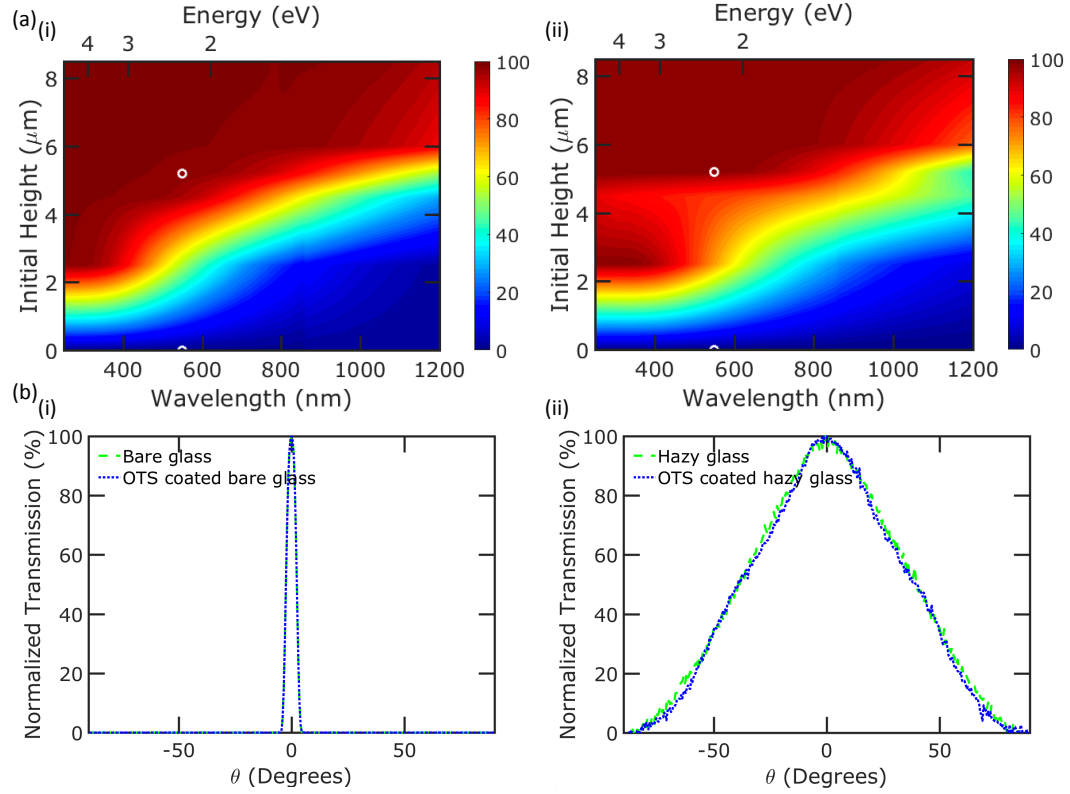


Figure 23 Haze contour plots of (a)(i) nanoglass glass and (ii) core/shell nanograss. (b) ADF plots of (i) Smooth glass and (ii) $5.2 \pm 0.2 \mu\text{m}$ height hazy glass without and with OTS layer.

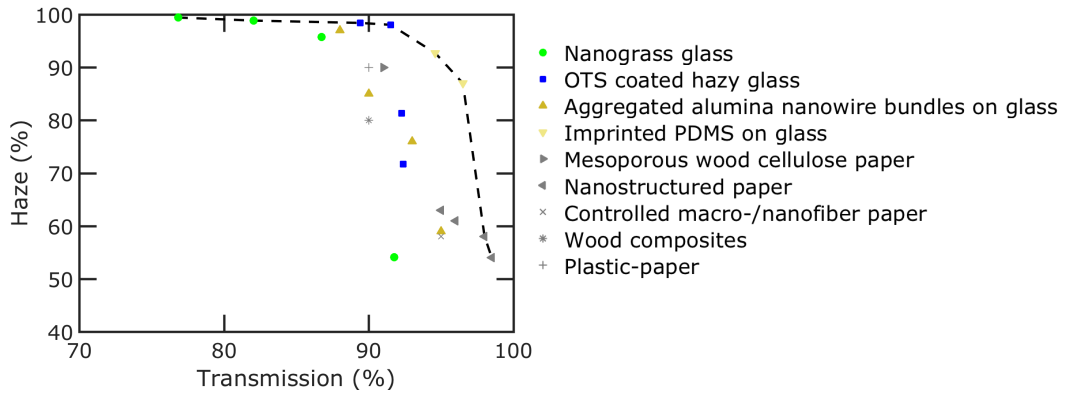


Figure 24 Haze versus transmission for substrates at $\lambda = 550 \text{ nm}$. Our hazy glass data with and without OTS layer is shown. The best data for aggregated alumina nanowire arrays on glass[93], imprinted PDMS on glass [22], mesoporous wood cellulose paper [229], controlled macro/nanofiber paper[32], nanostructured paper[34], wood composites[231], and plastic-paper hybrids[211] are also shown. The Pareto frontier of all the data is marked with a dashed line.

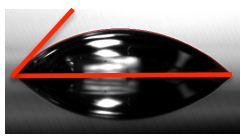
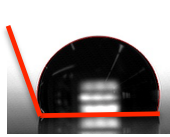
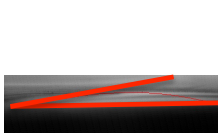
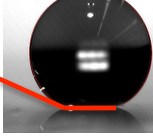
	Bare glass	OTS coated glass	Nanograss glass	OTS/silica nanostructured glass
Water droplet shape				
Static water contact angle (degrees)	42.9 ± 1.1	108.5 ± 0.7	7.4 ± 0.2	159.7 ± 0.6
Contact angle hysteresis (degrees)	35.5 ± 2.7	19.5 ± 1.7	-	4.9 ± 0.6

Figure 25 Water contact angle of bare glass, OTS coated bare glass, $5.2 \pm 0.2 \mu\text{m}$ height nanograss glass, and $5.2 \pm 0.2 \mu\text{m}$ initial height OTS/silica nanostructured glass.

μm initial height hazy glass before and after OTS coating. As can be seen from these plots, the OTS coating does not change the haze substantially in either sample. On bare glass, the OTS only forms a monolayer [90] and does not change the haze as expected. On the nanograss glass, the OTS also does not change the haze significantly. While the OTS reduces the height of the structures and merges some of the silica structures together, the structures are also heterostructures now with silica nanostructures and OTS coating. These additional interfaces may compensate for the reduced scattering from reduced roughness. The scattering angle range, defined as the range of angles in which lights have more than 5% intensity of the highest intensity at 0° was also characterized from these plots [34]. The scattering angle ranges of the bare silica and OTS-coated silica at wavelength of 550 nm are both 7° . The photodetector receives light in a 6° cone so that there is substantial broadening on the light intensities measured and the haze calculated directly from these plots differ from those measured with an integrating sphere. The haze of these samples at 550 nm are both less than 1%. For the $5.2 \pm 0.2 \mu\text{m}$ height hazy nanograss glass, the scattering angle range is 146° initially and 143° after OTS coating. The haze of these samples are $98.5 \pm 0.5\%$ and $98.1 \pm 0.5\%$, respectively.

Figure 24 plots the the total transmission and haze (at 550 nm) for a variety of optoelectronic substrates. For each type of substrate, only the best performing data (as defined by Pareto optimality) is plotted. The Pareto frontier is the set of solutions where one attribute cannot be improved without degrading another attribute. Our experimental data for the nanograss glass is plotted with green circles and our data for the OTS/silica nanostructures is plotted with blue squares. For comparison purposes, we plot the best performing optoelectronic substrate data in the literature for glass substrates using yellow markers and other optoelectronic substrates using gray markers. Glass substrates have been modified using aggregated alumina nanowire arrays [93] and imprinted PDMS on glass [22]. In addition, a variety of paper substrates have been demonstrated such as mesoporous wood cellulose paper [229], controlled macro/nanofiber paper[32], nanostructured paper[34], wood composites[231], and plastic-paper hybrids[211]. For the nanograss glass samples, two of the nanograss glass samples reside on the Pareto frontier. The $8.5 \pm 0.2 \mu\text{m}$ height nanograss glass exhibits $76.8 \pm 0.5\%$ transmission and $99.4 \pm 0.5\%$ haze, and the $6.0 \pm 0.2 \mu\text{m}$ height nanograss glass has $82.1 \pm 0.5\%$ transmission and $98.9 \pm 0.5\%$ haze. Other Pareto optimal structures include imprinted PDMS on glass with 94.6% transparency and 92.7% haze and 96.5% transparency and 87% haze [22]. Our OTS/silica nanostructured glass demonstrates the highest combination of transmission and haze as well. The $6.0 \pm 0.2 \mu\text{m}$ and $5.2 \pm 0.2 \mu\text{m}$ initial height (1.1 ± 0.2 and $1.0 \pm 0.2 \mu\text{m}$ final height, respectively) OTS/silica nanostructures have $89.4 \pm 0.5\%$ transmission and $98.4 \pm 0.5\%$ haze and $91.5 \pm 0.5\%$ transmission and $98.1 \pm 0.5\%$ haze, respectively.

For a surface to be self-cleaning, it needs to have a combination of superhydrophobicity ($\text{WCA} > 150^\circ$) and small contact angle hysteresis[10]. We next compare how the OTS modifies the wetting of various surfaces. Figure 25 shows the static WCA and hysteresis of bare glass, OTS coated bare glass, $5.2 \pm 0.2 \mu\text{m}$ height nanograss glass, and $5.2 \pm 0.2 \mu\text{m}$ initial height ($1.0 \pm 0.2 \mu\text{m}$ final height) OTS/silica nanostructured glass. The hysteresis is the difference between the advancing and receding contact angle. The bare fused silica is hydrophilic with a WCA of $42.9 \pm 1.1^\circ$. After OTS coating, the glass becomes hydrophobic as the WCA increases to $108.5 \pm 0.7^\circ$. However, the OTS coating on bare glass is not enough to make the bare glass sample superhydrophobic. In contrast, nanostructures have been

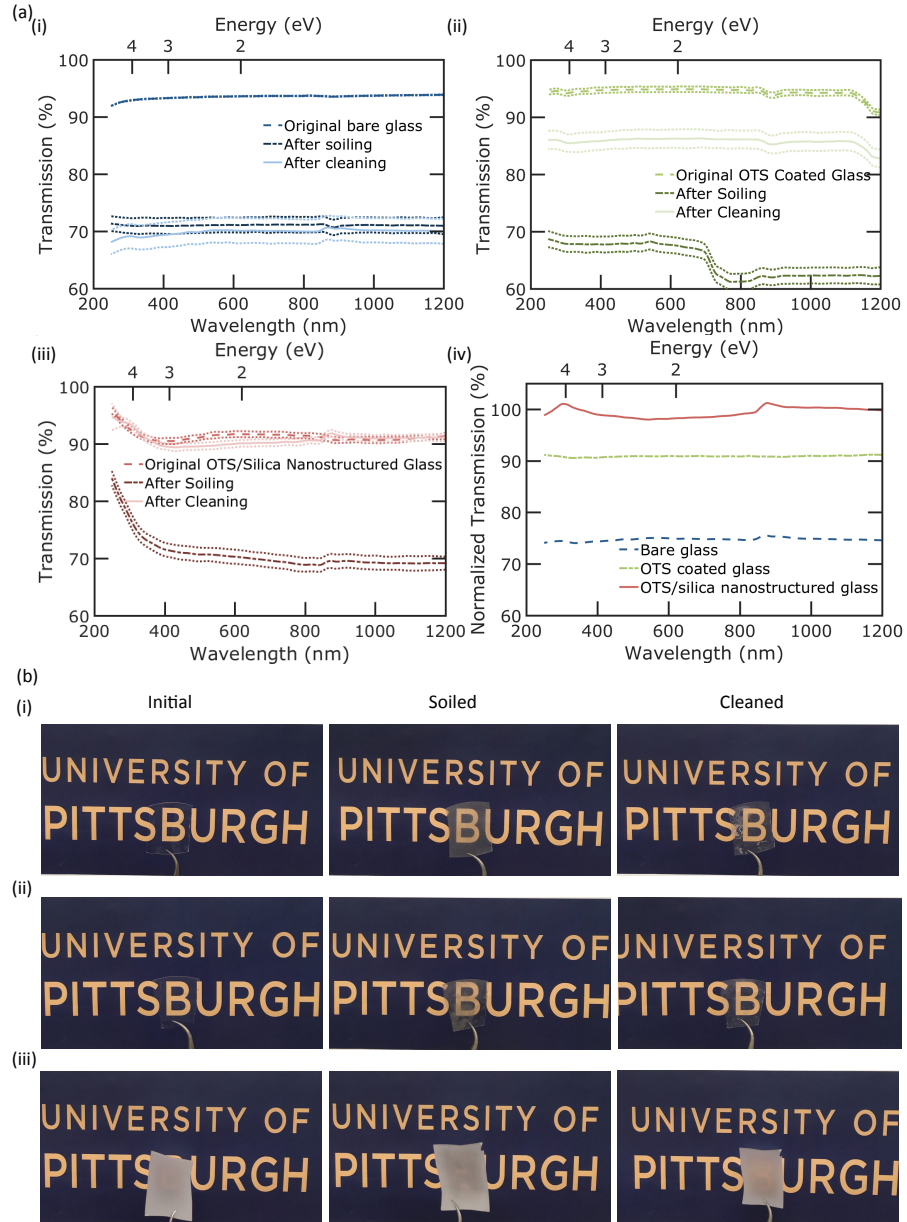


Figure 26 (a) Total transmission plots as a function of wavelength for (i) flat fused silica, (ii) OTS coated flat fused silica and (iii) $5.2 \pm 0.2 \mu\text{m}$ height OTS coated nanoglass glass in three different states. (a) (iv) plots the normalized transmission of the various glass substrates showing the mean transmission after cleaning relative to the original mean transmission. (b) Shows Optical images of (i) flat fused silica, (ii) OTS coated flat fused silica and (iii) $5.2 \pm 0.2 \mu\text{m}$ height OTS coated nanoglass glass in initial, soiled and cleaned states.

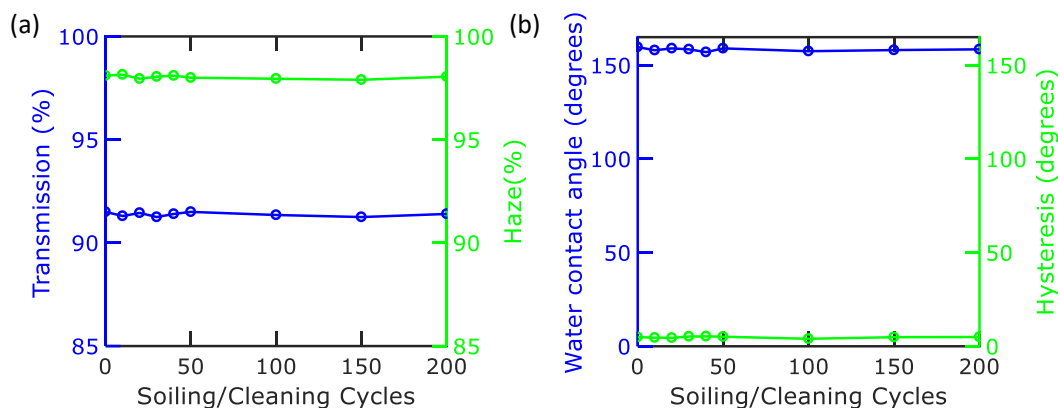


Figure 27 (a) Transmission (left y-axis) and haze (right y-axis) at 550 nm wavelength as a function of soiling/cleaning cycle for $5.2 \pm 0.2 \mu\text{m}$ initial height OTS/silica nanostructured glass. (b) Water contact angle (left y-axis) and hysteresis (right y-axis) as a function of soiling/cleaning cycle for $5.2 \pm 0.2 \mu\text{m}$ initial height OTS/silica nanostructured glass.

demonstrated to increase superhydrophilicity and superhydrophobicity [121, 30, 92, 127]. The nanoglass glass is superhydrophilic with a contact angle of $7.4 \pm 0.2^\circ$ as the nanostructuring enhances the Wenzel state of wetting. After OTS coating, the wetting of the nanostructures becomes superhydrophobic with a WCA of $159.7 \pm 0.6^\circ$. The nanostructures promote Cassie-Baxter wetting where air pockets increase the apparent static water contact angle. The hysteresis is only $4.9 \pm 0.6^\circ$, which is indicative of weak water adhesion with the surface. When the OTS/silica nanostructured glass is tilted just slightly, the droplets easily roll off. The rolling angle was measured as $1.5 \pm 0.5^\circ$.

To study the self-cleaning functionality of the different types of glass, we performed self-cleaning tests where samples were soiled with graphite powder and then rinsed with water. Self-cleaning is defined here as the application of water without any additional scrubbing. Glass substrates of about 5 cm^2 area were soiled with 0.5 grams of graphite powder and then rinsed with 2 mL of water. The total transmission of the samples was measured initially, after soiling, and finally, after cleaning. Figure 26 summarizes these self-cleaning results. Figure 26(a) shows the transmission spectra and figure 26(b) shows optical images of the (i) bare glass, (ii) OTS coated bare glass, and (iii) OTS/silica nanos-

structured glass in the original state, after soiling, and after cleaning. Three measurements were made for each sample and the mean and standard deviation for each state are also shown. For the bare glass, no improvement in transmission was observed after cleaning with water. The standard deviation becomes larger due to decreased uniformity in the transmission as the graphite tended to agglomerate into patches as can be seen in Fig. 26(b). In contrast, the OTS coated bare glass shows some improvement in transmission after cleaning, but does not recover its original transmission. Finally, the OTS/silica nanostructured glass decreases similarly to the other two samples, but the transmission almost recovers back to its original state after rinsing.

Figure 26(a)(iv) plots the normalized transmission of the various glass substrates showing the mean transmission after cleaning relative to the original mean transmission. The bare glass transmission is about 75% of its original value across all wavelengths after cleaning which is about the same as what it is in the soiled state.

In contrast, the soiled OTS coated bare glass recovers about 91% of its original transmission after cleaning. Finally, the OTS/silica nanostructured glass not only demonstrates the best anti-fouling properties as its transmission decreases the least in the soiled state, but self-cleaning, where the transmission is about 100% of its original value. Due to statistical variation, the transmission after cleaning is, in fact, over 100% of its original value and in some parts of the spectrum measured and slightly below 100% in others.

In order to study the long term functionality of self-cleaning glass, the same soiling and cleaning procedure were performed up to 200 cycles and the transmission and haze at 550 nm and the WCA and hysteresis were measured. Figure 27(a) plots transmission at 550 nm (left y-axis) and haze (right y-axis) at 550 nm wavelength as a function of cleaning cycle for 5.2 μm initial height OTS/silica nanostructured glass. There were no significant changes in both transmission and haze after 200 cycles of soiling and cleaning. Figure 27(b) plots the WCA (left y-axis) and hysteresis (right y-axis) as a function of cleaning cycle for 5.2 μm initial height OTS/silica nanostructured glass. The WCA and hysteresis were also maintained after up to 200 cycles of soiling and cleaning. These experiments demonstrate that the durability of the self-cleaning glass is promising.

4.1.3 Conclusions

In conclusion, we demonstrated self-cleaning, high transmission, near unity nanostructured glass. The $5.2 \pm 0.2 \mu\text{m}$ initial height OTS/silica nanostructured glass showed $91.5 \pm 0.5\%$ total transparency and $98.1 \pm 0.5\%$ haze and 143° scattering angle at 550 nm wavelength. The wetting went from superhydrophilic to superhydrophobic after OTS coating. The OTS/silica nanostructures demonstrate high water contact angle and low contact angle hysteresis. The samples demonstrate self-cleaning functionality where graphite soiled substrates recover about all of their transparency after rinsing with water. This characteristics make the superhydrophobic hazy glass a strong candidate to use in optoelectronic applications such as solar cells and LEDs which combination of high transmission, high haze, and self cleaning function are important requirements.

4.2 Stain-Resistant, Superomniphobic Flexible Optical Plastics Based on Nano-Enoki Mushrooms

4.2.1 Introduction

There has been tremendous research interest in superhydrophobic surfaces, which strongly repel water, and can provide for functionalities such as anti-fogging [16], anti-icing [13], antibacterial[96], and self cleaning [42, 65]. In addition, there is great interest in extending this repellency beyond water. Surfaces that exhibit these properties may be referred to as superoleophobic for oils or superomniphobic for a wide range of liquids. A variety of re-entrant geometry structures such as hierarchical structures [55] and mushroom-like micropillars [131, 19, 120] have been demonstrated for superomniphobicity. Superomniphobicity may be used for self-cleaning surfaces [11], chemical shielding surfaces [149], and stain-free clothing [20, 109]. These functionalities may also be combined with high transparency and high haze for use in optoelectronic applications.[55, 127]

So far, the only work on omniphobic substrates with high transparency and high haze has been the work of Jeong *et. al*, where they reported on a PET substrate with silica

nanoparticle coating that improves the photon-to-electron conversion efficiency of organic solar cells by 13% compared to that on a PET substrate without the silica nanoparticle array layer. [88].

However, the transparency of these coated substrates is fairly low at less than 80%. Furthermore, the sample demonstrates a contact angle of 139° , for ethylene glycol, which still has a relatively high surface tension of 47.7 mN/m. The demonstration of superomniphobicity with low liquid surface tension liquids such as hexadecane, which has a surface tension of 27.7 mN/m, while offering high transparency and high haze performance, has yet to be demonstrated.

In this section, we demonstrate stain-resistant superomniphobic flexible optical plastics with nano-enoki mushroom-like structures that may be fabricated through scalable processes.

Our nano-enoki polyethylene terephthalate (PET) has re-entrant geometry and close spacing between structures to provide for both high apparent contact angles $> 150^\circ$ and low contact angle hysteresis for a wide variety of liquids of varying surface tension such as water, ethylene glycol, olive oil, and hexadecane. The nano-enoki exhibit high pressure stability due to the few micron-scale spacing between our nanostructures, which provides for a large energy barrier to water infiltration. The spacing between our nanostructures is the closest in the literature that we are aware of for re-entrant superomniphobic structures. Our nano-enoki structures exhibit no evidence of water breakthrough at pressures over 900 Pa, which demonstrates the high metastability of Cassie-Baxter state wetting. Furthermore, the nano-enoki PET exhibits high transmission and ultrahigh haze of 86.4% and 96.4%, respectively, at a wavelength of 550 nm, which may be suitable for some optical applications.

The surfaces exhibit stain-resistance for a variety of liquids including mustard and blood, where the transparency of the original plastic is recovered after staining. Dried mustard and blood both flake off the samples without any residue, indicating no infiltration of the liquid and poor adhesion to the surface.

We also performed durability experiments that demonstrate these nanostructured PET substrates are robust from bending and show similar transmission, haze, contact angle and hysteresis values after 5,000 cycles of bending.

4.2.2 Results and Discussion

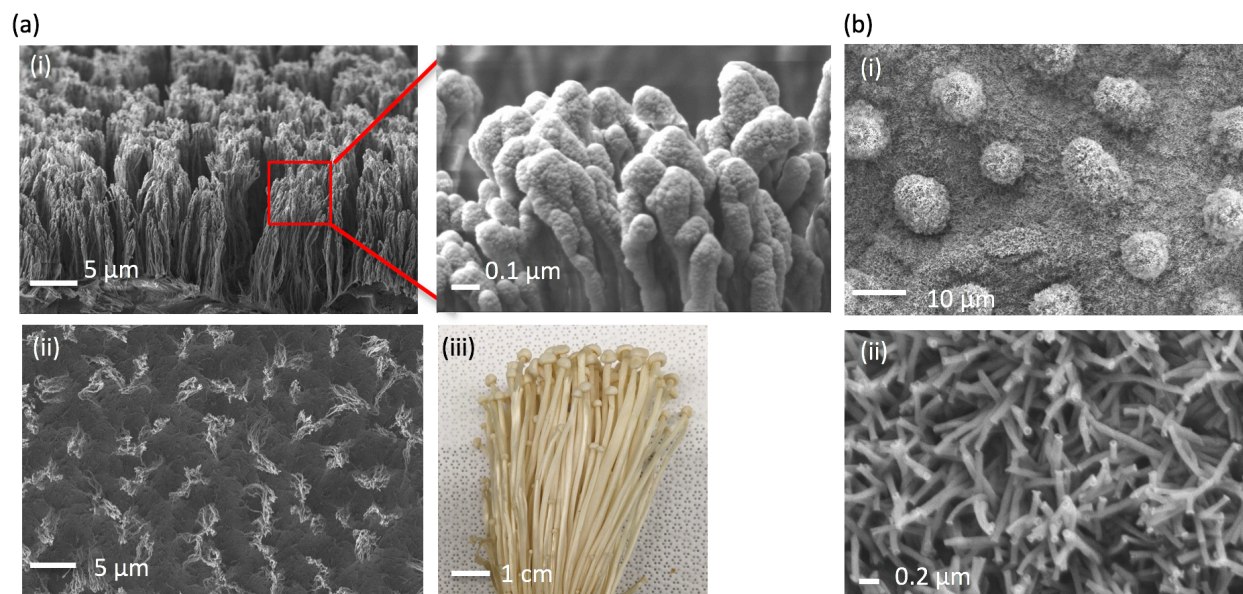


Figure 28 (a) Nano-enoki mushroom structures on PET. (i) 20° tilted cross section SEM images and (ii) overhead SEM images. (iii) Optical image of enoki mushrooms. (b) SEM images of lotus leaf surface at different resolutions demonstrating (i) microstructure bumps and (ii) nanostructures.

Figure 28 shows details and results of the nano-enoki mushroom structures on PET and compares them to that of the *Nelumbo nucifera* or sacred lotus leaf surface. Fig. 28(a) shows results of the enoki mushroom-like nanostructures. The structures are formed by first etching the PET with a maskless reactive ion etching (RIE) process [64], then coating the nanostructures with a silica layer by plasma enhanced chemical vapor deposition (PECVD) and finally, treating the structures with a low surface energy fluorosilane. The PECVD process tends to deposit silica on top of the nanostructures instead of the bottom, thus creating the re-entrant enoki mushroom-like nanostructures. The subsequent fluorosilane treatment forms a monolayer of fluorosilane on the structure [138]. Figure 28(a)(i) shows 20° tilted cross section SEM images and (ii) shows an overhead SEM image. The nanostructures shown here are initially 18 μm in height after etching for 60 minutes. The structures have a diameter of about 50-100 nm at the bottom which gradually increases to 200-500 nm at the top. The overhead SEM image shows some coalescence of nanostructures during the SiO₂ deposition.

Figure 28(a)(iii) shows a picture of actual enoki for comparison, where the mushrooms have larger tops and a long string-like appearance. For comparison purposes, we provide SEM images of the lotus leaf.

The lotus leaf surface consists of micron-sized papillae (Fig. 28(b)(i)) with nanometer-size protrusions (Fig. 28(b)(ii)) and a surface layer of epicuticular wax. Superhydrophobic surfaces are inspired by the leaves of the sacred lotus plant, which are both anti-fouling and self-cleaning due to this combination of hierarchical surface morphology and hydrophobic epicuticular wax [7].

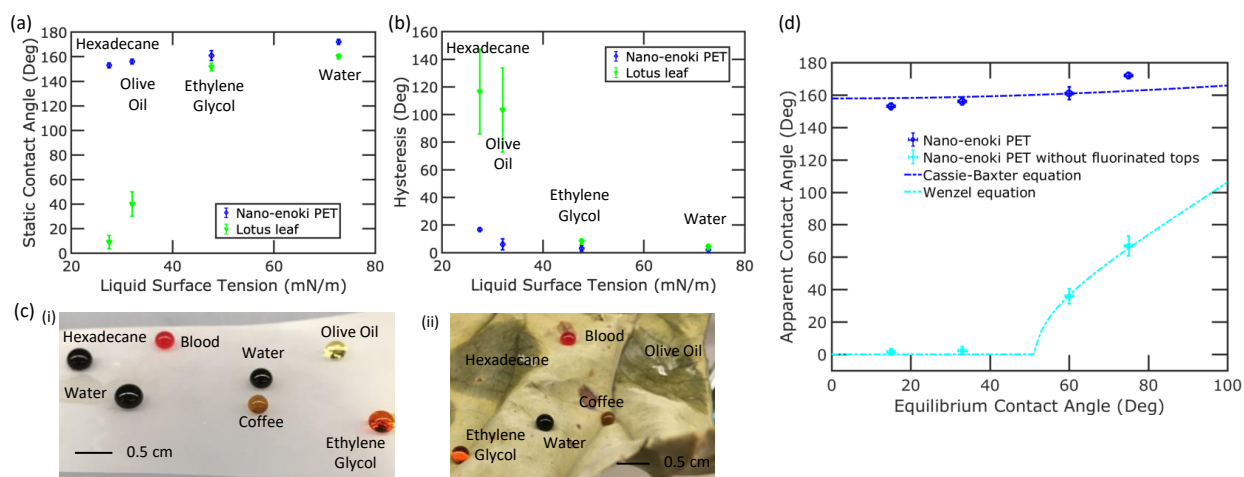


Figure 29 Surface wetting results. (a) The apparent contact angle variation of 18 μm tall nano-enoki PET and lotus leaf for water, ethylene glycol, olive oil, and hexadecane. (b) Hysteresis of different liquids with different surface tension on the 18 μm tall nano-enoki PET and lotus leaf. (c) Optical picture of various liquids on the (i) plastic demonstrating superomniphobicity and (ii) lotus leaf demonstrating superhydrophobicity, but inability to repel lower surface tension liquids of olive oil and hexadecane. (d) Plot of apparent contact angle versus equilibrium contact angle of four different liquids for nano-enoki and nano-enoki without fluorinated tops. The Cassie-Baxter equation and Wenzel equation are also plotted with estimates of the solid-liquid area fraction and roughness. The dotted lines come from standard error estimates.

Wetting characterization of the nano-enoki PET and lotus leaf were performed with water (surface tension of 72.8 mN/m), ethylene glycol (47.7 mN/m), olive oil (32.0 mN/m), and hexadecane (27.5 mN/m).

Figure 29(a) shows the static contact angles of these four liquids for the 18 μm tall nano-enoki PET as compared to the lotus leaf. The lotus leaf is superhydrophobic with a

static contact angle of $160 \pm 2^\circ$ for water. However, lower surface tension liquids tend to spread more easily and have lower static contact angles. The contact angles are $40 \pm 3^\circ$, and $7 \pm 2^\circ$ for olive oil and hexadecane, respectively, which tend to spontaneously spread on the lotus leaf surface. Not only does the nano-enoki PET exhibit high static water contact angles, but also high contact angles for the other liquids tested above 150° . The nano-enoki PET exhibits contact angle values of $172 \pm 1.5^\circ$, $161 \pm 1.6^\circ$, $156 \pm 1.5^\circ$ and $153 \pm 1.7^\circ$, for water, ethylene glycol, olive oil and hexadecane, respectively.

Figure 29(b) plots the contact angle hysteresis for the four liquids for both the lotus leaf and the nano-enoki. The contact angle hysteresis is the difference between the advancing and receding contact angle. The large hysteresis values of the olive oil and hexadecane on the lotus leaf are indicative of strong adhesion to the surface. For the nano-enoki PET, the contact angle hysteresis for the four liquids are $2.0 \pm 0.6^\circ$, $3.0 \pm 0.5^\circ$, $6.0 \pm 2.0^\circ$ and $17.0 \pm 1.2^\circ$, respectively. The high apparent contact angles and small hysteresis angles of the re-entrant nano-enoki mushrooms for a wide range of liquids demonstrate the superomniphobicity of these structures. The droplets of different liquids easily roll off the surface due to the repellency of the liquids. Figure 29(c)(i) shows an optical image of different liquids on the $18 \mu\text{m}$ superomniphobic Enoki mushroom-like nanostructured PET. The superomniphobic surface demonstrates repellency for a wide variety of liquids beyond those evaluated, including blood and coffee. Figure 29(c)(ii) shows an optical image of different liquids on a lotus leaf. The lotus leaf shows high apparent contact angles for water, ethylene glycol, blood and coffee. However, the olive oil and hexadecane droplets spread spontaneously on the leaf.

To examine the importance of re-entrant structures and fluorination in promoting Cassie-Baxter state wetting, we compared the wetting properties of our $18 \mu\text{m}$ tall nano-enoki PET to the same structures without fluorinated tops. The nano-enoki without fluorinated tops are the structures just after the RIE process, without the additional PECVD and fluorination. Fig. 29(d) plots the experimentally measured apparent contact angles of the nano-enoki PET as well as the nano-enoki PET without the fluorinated tops for water, ethylene glycol, olive oil and hexadecane.

The apparent contact angles of the four liquids on the nano-enoki PET were compared with that predicted from the Cassie-Baxter equation:

$$\cos(\theta^*) = f_{SL} \cos(\theta_E) - f_{LV} \quad (4.1)$$

where f_{SL} is the areal fraction of the solid-liquid interface, f_{LV} is the areal fraction of the liquid-vapor interface, θ^* is apparent contact angle, and θ_E is the equilibrium contact angle. $f_{SL} + f_{LV} = 1$. f_{SL} was treated as a fitting parameter, and the curve fit shown is with $f_{SL} = 0.04$, which is consistent with estimates from overhead SEM pictures.

The θ_E values are the contact angles of different liquids on plain PET. θ_E was measured to be $75.0 \pm 1.0^\circ$, $60.0 \pm 1.0^\circ$, $33.0 \pm 1.0^\circ$ and $15.0 \pm 1.0^\circ$ for water, ethylene glycol, olive oil and hexadecane, respectively.

The prediction from the equation agrees well with the measured apparent contact angles indicating that the liquids are indeed in the Cassie-Baxter state of wetting.

We further compare the experimentally measured apparent contact angles for the nano-enoki PET without fluorinated tops with the predicted apparent contact angles from the Wenzel equation:

$$\cos(\theta^*) = r \cos(\theta_E) \quad (4.2)$$

where the value of surface roughness r is estimated as $r = 1.5$ for the $18 \mu\text{m}$ tall nano-enoki PET without fluorinated tops with a diameter of 225 nm and pitch of $5 \mu\text{m}$.

As can be seen from the plot, our experimental data agrees well with that predicted from the Wenzel equation. For liquids with an equilibrium contact angle less than 50° , such as hexadecane and olive oil, the liquid completely spreads over the nanostructured surface. In the cases where the surface has an affinity for the liquid (equilibrium contact angle less than 90°), Wenzel wetting state is enhanced by nanostructuring and decreases the wetting contact angle[29]. The fluorinated tops of the nano-enoki are critical for creating low surface energy re-entrant structures that promote Cassie-Baxter state wetting as opposed to the Wenzel state. The low contact angle fraction between the droplets and plastic in the Cassie-Baxter wetting state enable the high apparent contact angles and low contact angle

hysteresis. To characterize the stability of the metastable Cassie-Baxter wetting state of droplets on our nano-enoki nanostructures, we characterized the breakthrough pressure of nano-enoki of different heights. Different height nano-enoki were fabricated by varying the RIE etch time, while the PECVD and fluorination process were kept the same. A 5 μl drop of water was placed on each substrate and evaporated while monitoring the decrease of contact angle. Fig. 30(a) plots the evolution of the contact angle as a function of time and Fig. 30(b) plots the contact angle as a function of the baseline diameter. In all surfaces, the contact angle decreased continuously without any evidence of pinning due to the low contact angle hysteresis of the surfaces and without any sudden discontinuities in contact angle. The decreasing contact angle is indicative of gradual infiltration of the water into the structures. However, only the 4 μm tall nano-enoki exhibited a decrease in contact angle without a concomitant decrease in baseline diameter, indicative of breakthrough into the Wenzel wetting state. In these shorter nano-enoki, the droplet may transition into the Wenzel state at lower pressures as it is easier for the droplet to droop and touch the bottom of the space between nano-enoki as the pressure increases [91]. The breakthrough pressure is the maximum external pressure that the surface can tolerate before transition from the Cassie-Baxter state to the Wenzel state. [182]. The robustness factor A^* is a measure of the metastability of the Cassie-Baxter state for a given surface[182, 55, 103]:

$$A^* = P_{\text{breakthrough}}/P_{\text{ref}} \quad (4.3)$$

where $P_{\text{breakthrough}}$ is the breakthrough pressure at which the surface wetting transitions to the Wenzel state, and P_{ref} is a reference pressure given by

$$P_{\text{ref}} = 2\gamma_{LV}/\sqrt{\gamma_{LV}/\rho g} \quad (4.4)$$

where ρ is the liquid density, and g is the gravitational acceleration [182].

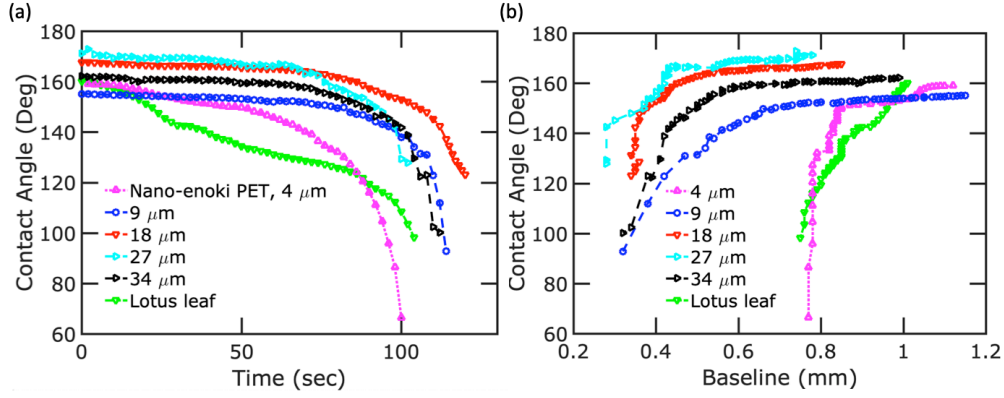


Figure 30 Stability characterization of Cassie-Baxter state wetting. Contact angle as a function of (a) time and (b) baseline for nano-enoki of different heights and lotus leaf.

When A^* is less than 1, the composite solid-liquid-air interface cannot be supported and the Cassie-Baxter state is not metastable. A minimum 160 μm droplet radius was observed in the nano-Enoki PET without any breakthrough. This corresponds to a breakthrough pressure over 900 Pa and robustness factor more than 17. Other studies in the literature such as mushroom-shaped micropillar arrays [19] or hierarchical structures [55] exhibit lower breakthrough pressures or lower robustness factors as those structures are over 20 microns apart from each other. In contrast, the spacing of our nano-enoki structures is only approximately 5 μm and thus provides for a much larger energy barrier for water infiltration that increases the robustness of the Cassie-Baxter wetting state and superhydrophobicity. The spacing of the nano-enoki structures is the smallest in the literature that we are aware of for superomniphobic re-entrant structures. Back of the envelope calculations with a spacing of 5 μm , and 9 μm height and diameter of 300 nm suggest the water droplet will only contact the bottom of the cavity when the radius of the droplet is smaller than the spacing or 5 μm [91]. A droplet of radius 5 μm would have a breakthrough pressure of 28 kPa.

The nano-enoki exhibit high transparency and high haze, which make them suitable as an optical plastic. Compared to the initial bare plastic, the nano-enokis demonstrate comparable transmission values (86.4% versus 88.4% at wavelength of 550 nm) and ultrahigh haze values (96.4% versus 1.1%). The transparency and haze are similarly high

between 400 and 1200 nm wavelengths. The sub-wavelength nature of the nano-enoki provide for the high scattering and high transparency that is not possible with larger structures. High transparency, high haze optical substrates are important for solar cells and light emitting diodes where they increase the incoupling and outcoupling of light, respectively [71, 136, 134, 88].

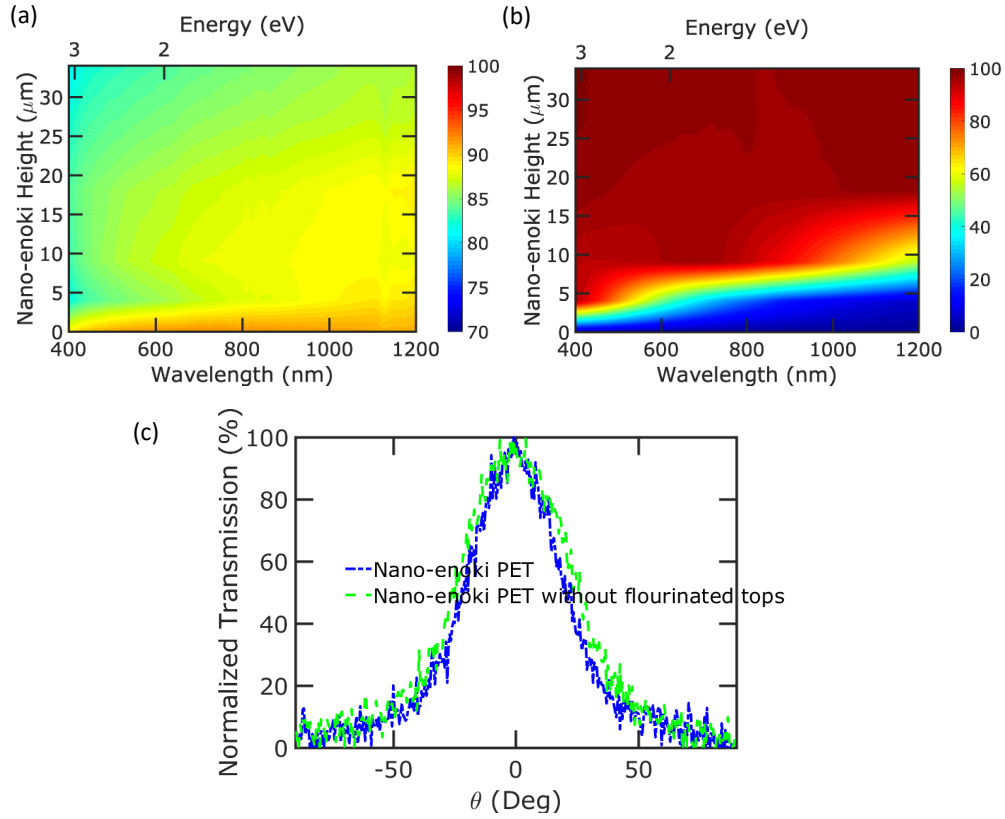


Figure 31 Contour plots of (a) total transmission and (b) haze of nano-Enoki PET as a function of wavelength and height. (c) shows the scattering angular distribution of transmission for nano-enoki with and without fluorinated tops.

Figure 31 summarize the optical results of the samples. Figure 31(a) shows the total transmission of the nano-enoki as a function of height from 400 to 1200 nm. The transmission at a height of 0 μm corresponds to flat PET. Initial creation of the nano-enoki PET corresponds to a reduction in transmission as the creation of the enoki tops increases the reflection. However, additional increases in the height only slightly decrease the transmission.

Figure 31(b) plots the haze from 400 to 1200 nm as a function of nanostructure height for various structures. The optical haze increases monotonically with the height of the nano-enoki PET.

We next characterized the angular distribution of the transmission through various substrates. Figure 31(c) shows the scattering angular distribution of transmission for nano-enoki with and without flourinated tops. The scattering angle range of both samples are more than 170° which shows the strong light scattering capabilities and is much more than the scattering angles of ultrahigh haze nanostructured paper [34]. This figure also shows that the fluorination of the nano-enoki does not effect on the scattering angle since it only forms a monolayer [180, 125, 138, 198].

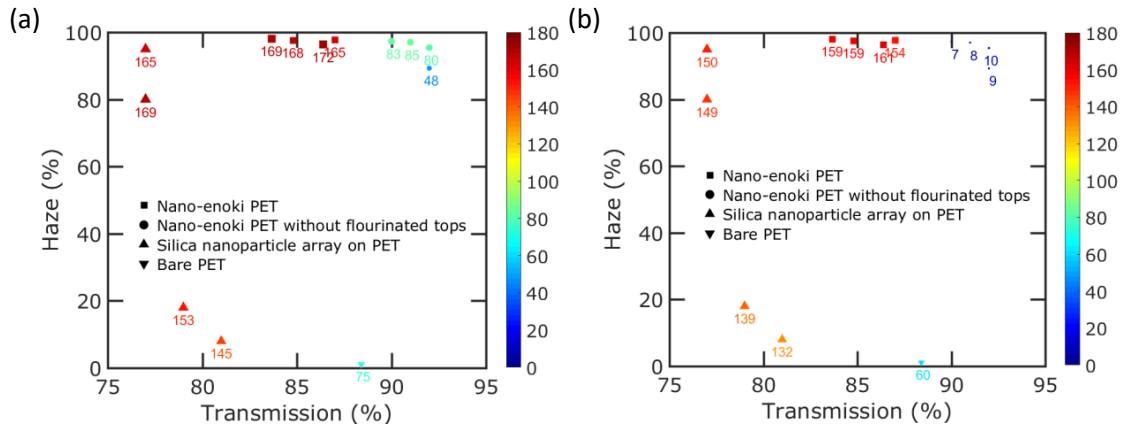


Figure 32 Comparison of transparency (at wavelength 550 nm), haze (also at 550 nm) and (a) water and (b) ethylene glycol contact angle (in degrees) of our re-entrant nano-enoki PET, plain PET and silica nanoparticle array on PET [88]. The color and size of the data points correspond to the contact angle, which is also used to label each data point. The shape of each data point corresponds to the type of surface.

Figure 32 plots the wetting and photon management properties of the nano-enoki PET. In particular, Figure 32(a) compares the water contact angle, transmission and haze, and Figure 32(b) plots the ethylene glycol contact angle, transmission and haze of our nano-enoki PET in comparison with the data reported in Jeong *et. al* [88]. As can be seen from these figures, the water contact angle, oil contact angle, transparency and haze for our $18 \mu\text{m}$ height nano-enoki structure are $172 \pm 1.5^\circ$, $161 \pm 1.6^\circ$, 86.4%, and 96.4%, respectively, while the corresponding values for best sample in their work are 165° , 150° ,

77%, and 95%. Therefore, our work not only improves optical properties significantly, but also shows higher water and ethylene glycol contact angle. The hexadecane contact angle for our nano-enoki structures is $153 \pm 1.7^\circ$, which is higher than the 126° reported in this previous work.

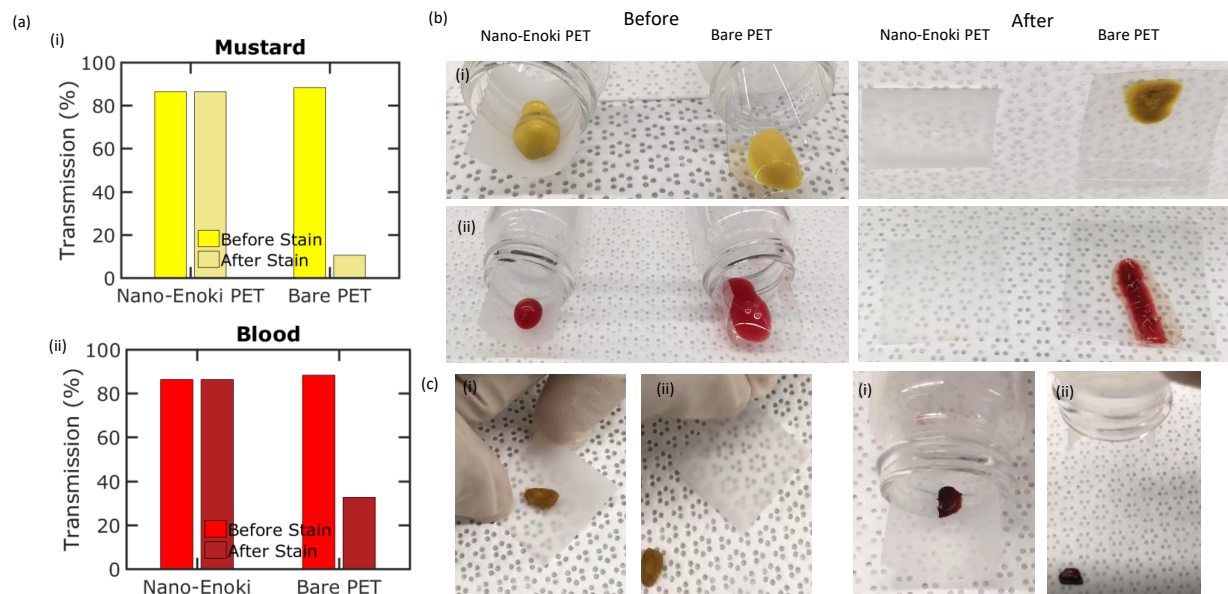


Figure 33 (a) Transparency at 550 nm for nano-enoki PET and bare PET before and after staining of (i) mustard, and (ii) blood. (b) Optical images of (i) mustard, and (ii) blood stain before and after evaporation. (c) Optical pictures of dried mustard and blood droplets on nano-enoki (i) after drying and (ii) after tilting the substrate where the droplet simply flakes off the surface.

Next, we characterized the stain-resistance ability of our nano-enoki structures. Figure 33(a) shows the stain test results for (i) mustard, and (ii) blood. The transparency at 550 nm for nano-enoki samples do not change after stain test. In contrast, the transparency of bare PET reduces significantly after the stain test for mustard and blood. Figure 33(b) shows optical images of the (i) mustard, and (ii) blood. The mustard and blood tend to dry into small spots and easily flake off the nano-enoki PET surface after the sample is tilted due to the low infiltration of the liquid and repellency even after drying. In contrast, the mustard and blood spread over the bare PET and stay adhered to the surface. Figure 33(c) shows dried mustard and blood droplets on nano-enoki (i) after drying and (ii) after tilting the sample where the dried drop simply flakes off the surface.

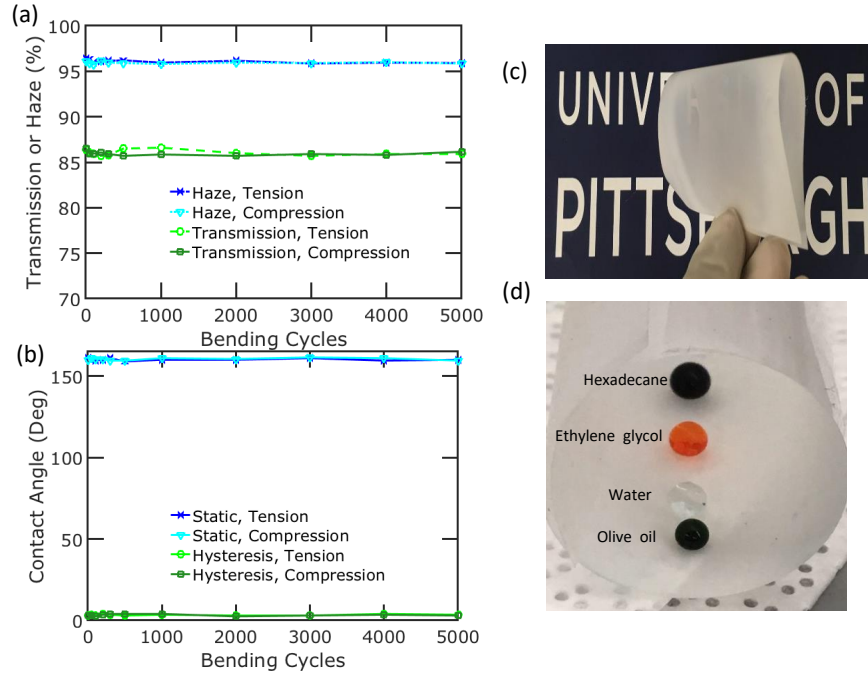


Figure 34 (a) Transparency and Haze at 550 nm and (b) oil contact angle and hysteresis as a function of bending cycle, for tension (left y axis) and compression (right y axis). (c) Optical image of flexibility of substrate (d) Optical image of different liquid droplets on curved PET. Food colors added to liquids in order to enhance visibility.

Figure 34 plots the (a) transmission and haze at 550 nm wavelength and (b) ethylene glycol contact angle and hysteresis as a function of bending cycle of the 18 μm nano-enoki PET, under tension (left y axis) and compression (right y axis). Bending tests were conducted by bending the PET substrate around a stainless steel rod with a 1 inch diameter. Two samples with identical size, 3 cm \times 3 cm, were placed under bending compression and tension by bending the etched surface towards and away from the steel rod, respectively. Figure 34 (c) and (d) show optical images of flexibility of nano-enoki PET and different liquid droplets on curved substrate. Neither the transmission, haze nor oil contact angle and hysteresis are changed significantly after 5000 cycles of bending, for either tension or compression. This suggests that the re-entrant enoki mushroom-like nanostructured PET is robust under bending and may be useful for flexible optoelectronic applications.

4.2.3 Conclusions

In conclusion, we demonstrate stain-resistant superomniphobic flexible optical PET based on nano-enoki structures. The nano-enoki demonstrate apparent contact angles over 150° and low contact angle hysteresis for a wide range of fluids with different surface tensions. This is in contrast with lotus leaf surfaces, which demonstrate low apparent contact angles and high contact angle hysteresis for olive oil and hexadecane. The fluorination and re-entrant tops of the nano-enoki provide for stable Cassie-Baxter state wetting, where the low contact angle fraction between the droplets and PET enable the high apparent contact angle and low contact angle hysteresis. The Cassie-Baxter state wetting is highly stable as breakthrough is not observed at pressures over 900 Pa, which correspond to a robustness factor over 17. In particular, the close spacing between nanostructures, which is smallest of all re-entrant structures in the literature that we are aware of, provides for high thermodynamic stability of the wetting. The nano-enoki demonstrate stain-resistance, where dried mustard and blood flake off the surface after tilting and the original transmission is recovered. The nano-enoki PET substrates are robust from bending and show similar transmission, haze, oil contact angle and hysteresis values after 5000 cycles of bending. This characteristics make the re-entrant nanograss PET a strong candidate to use in optoelectronic applications such as solar cells and LEDs which combination of flexibility, high transmission, high haze, and stain-resistance are important requirements.

5.0 Toward Finding Perfect Antireflection and Superomniphobic Structures

In the first section of this chapter, we review our works on using machine learning to fabricate highly transparent and superomniphobic glass substrates[67]. In the second section we evaluate different nanostructures to find the best antireflection functionality [66]. In the third section, we study the effect of the shape and geometry of the microstructures on the liquid repellency and mechanical durability by using 3D-printing technology[63].

5.1 Creating Glasswing-Butterfly Inspired Glass Through Bayesian Learning and Optimization

5.1.1 Introduction

Natural surfaces such as lotus leaves, moth eyes, and butterfly wings have evolved over millions of years to optimize different surface functionalities related to survival and adaptation in different environments. Various unique micro- and nanostructures may be found in these natural surfaces that provide for functionalities such as anti-soiling, self-cleaning, bacterial resistance, anti-fogging, and water harvesting [203, 175, 171, 72, 96, 86]. Inspired by nature, researchers have sought to understand how different micro- and nanostructures provide for desired functionalities and utilized this knowledge to demonstrate a multitude of synthetic surfaces with novel functionalities [133, 197, 226, 223, 114].

Many self-cleaning surfaces have been demonstrated [65, 138, 125] that are inspired by the superhydrophobic leaves of the *Nelumbo nucifera* (sacred lotus), which exhibit both high wetting contact angle (superhydrophobicity) and low contact angle hysteresis (adhesion) due to the combination of hierarchical surface morphology and hydrophobic epicuticular wax [7]. Superhydrophobic surfaces may be created through low-surface energy micro-/nanostructures which promote Cassie-Baxter wetting [15], where the water droplet contacts a small fraction of the surface due to air being trapped with the structures. This is

in contrast to Wenzel wetting, where the water homogeneously contacts the surface [196]. Water droplets easily roll or bounce off superhydrophobic surfaces, while removing dust particles with them.

While these surfaces effectively repel water, there is also great interest in surfaces that repel more types of liquids than just water. The ability to repel many liquids is referred to as *superomniphobicity*, where surfaces demonstrate a static contact angle greater than 150° and low contact angle hysteresis for a variety of liquids [149, 20, 4, 103, 181]. Creating surfaces that are superomniphobic is significantly more challenging than creating ones that are superhydrophobic. This is because the surface tensions of oil and other organic liquids are lower than water and thus, they tend to spontaneously spread across surfaces and past trapped air [174, 120, 164, 84, 19]. Springtail insects are the only known surface in nature that display apparent wetting contact angles $\theta > 150^\circ$ and low hysteresis for a wide range of fluids [19]. Recent research has suggested that the key to obtaining superomniphobicity is re-entrant structures or surfaces with concave topographic features, which provide for robust metastable trapped air interfaces [181].

While synthetic microscale superomniphobic surfaces have been demonstrated [215, 202, 131, 19, 120], major challenges exist in the creation of superomniphobic surfaces with *optical* functionality such as (i) lack of scalability in nanomanufacturing processes, (ii) low optical transmission, (iii) poor optical clarity due to light scattering, (iv) condensation failure, and (v) poor abrasion resistance. Creating superomniphobic surfaces through scalable manufacturing processes is a challenge due to the more demanding requirements for re-entrant micro-/nanostructures that are needed to achieve omniphobicity. Re-entrant structures have generally been achieved by complex micropatterning of a mask followed by some isotropic etch to provide for undercutting [202, 131, 19, 120]. The various re-entrant microstructures that have been demonstrated for superomniphobicity are far too large to provide for antireflection. Subwavelength structures such as the 200 to 300 nm sized pillars in moth eyes are needed for antireflection [176]. Poor optical clarity due to high haze is also a major issue. The large difference in refractive index at the solid–air interface of these surfaces results in significant light scattering[64]. Condensation on glass or so-called fogging can result in poor visibility [133] and destroy the superhydrophobicity

of surfaces [197]. Nanostructures with high height over pitch aspect ratios as well as close spacing are desirable for stable Cassie-Baxter wetting [151]. However, the need for high aspect ratio structures leads to poor abrasion resistance as tall, thin nanostructures can be easily scratched off. Indeed, many natural surfaces such as insect wings or eyes tend to be very fragile under abrasion [170].

In this study, we address these challenges by creating a new self-healing, durable superomniphobic glass with ultrahigh transparency and ultralow haze. Inspired by recent analysis of glasswing butterfly wings [171], this research focuses on random nanostructures as opposed to highly ordered sub-wavelength structure arrays that may exhibit undesirable optical diffraction patterns. The glass is demonstrated through a simple, scalable two-step maskless reactive ion etching and fluorination process, which we demonstrate on 4 inch diameter glass wafers. Single-side nanostructured glass exhibits 97.0% total transparency while double-side nanostructured glass exhibits 99.5% at 550 nm wavelength and less than 0.1% haze for both at the same wavelength. The glass shows broadband antireflection ($< 20\%$) even at high incidence angles of 70° . The specular reflection for single-side nanostructured glass and double-side nanostructured glass are 5.8% and 4.4% at 45° incident angle, respectively, while normal glass shows 8.3% reflection at the same incident angle. In addition, static water and ethylene glycol contact angles of $162.1 \pm 2.0^\circ$ and $155.2 \pm 2.2^\circ$, respectively, for fused silica glass were demonstrated. The glass exhibits resistance to condensation or *antifogging* properties. The glass we reported here shows antifogging efficiency[133] more than 90% and demonstrates water departure of droplets smaller than $2 \mu\text{m}$. The glass shows *self-healing* behavior after 500 mechanical abrasion cycles. The abraded glass can recover its high water and oil contact angle after heating for 15 minutes.

Identifying a fabrication process for such a high performance and multifunctionalized substrate with random nanostructures requires allowing great freedom in the possible fabrication process. Consequently, the number of process parameters for creating these nanostructures is often high-dimensional, with many etching and deposition process parameters that may be varied. Searching this space of possible fabrication strategies is often limited to grid-like search methods where a particular process parameter is systematically varied

based on physical intuition. That research approach is only effective to very small localized regions of the input parameter space and only in low dimensional spaces.

In contrast, this study combines a statistical machine learning procedure with the physical intuition of the authors to create a new high performance glass. To create this new glass, we demonstrate a design process that utilizes Bayesian learning and optimization [168, 39, 148] to facilitate an efficient search of this high-dimensional fabrication space. To balance the photon management and wettability properties, we posed a multiobjective optimization problem, where a subset of the Pareto efficient frontier is explored subject to pre-defined threshold values (as stated using expert physical intuition). Gaussian processes are built using existing experimental data, and then updated after each 5 experimental fabrications (which are conducted in parallel batches of 5 to facilitate a faster search). These batches of 5 fabrication strategies were devised to maximize a modified form of expected improvement, which defines the utility of identifying high performing fabrication parameters subject to their viability of satisfying the thresholds.

5.1.2 Fabrication Strategy

The nanofabrication process is performed in two steps: (a) reactive ion etching (RIE) and (b) plasma enhanced chemical vapor deposition (PECVD) and surface treatment with fluorination. This fabrication process scalably creates the nanostructures directly into the fused silica glass without the need for patterning or an external mask[64]. Fig. 35(a) depicts the input and output parameters under analysis, and suggests how we will efficiently optimize this process (which we discuss in greater detail later in this section).

The first fabrication step focuses on RIE to create sub-wavelength nanostructures in the fused silica in order to maximize the total transparency and minimize the haze at the wavelength of 550 nm. In the RIE process, the etch chamber is pumped down to high vacuum and then an etching gas is flowed into the chamber. Next, a 13.56 MHz radio-frequency (RF) power is applied to a pair of parallel electrodes which generates a plasma. Reactive species, such as ions and radicals, and monomers are formed when the etch gas is dissociated in this plasma. These reactive species and monomers are transported

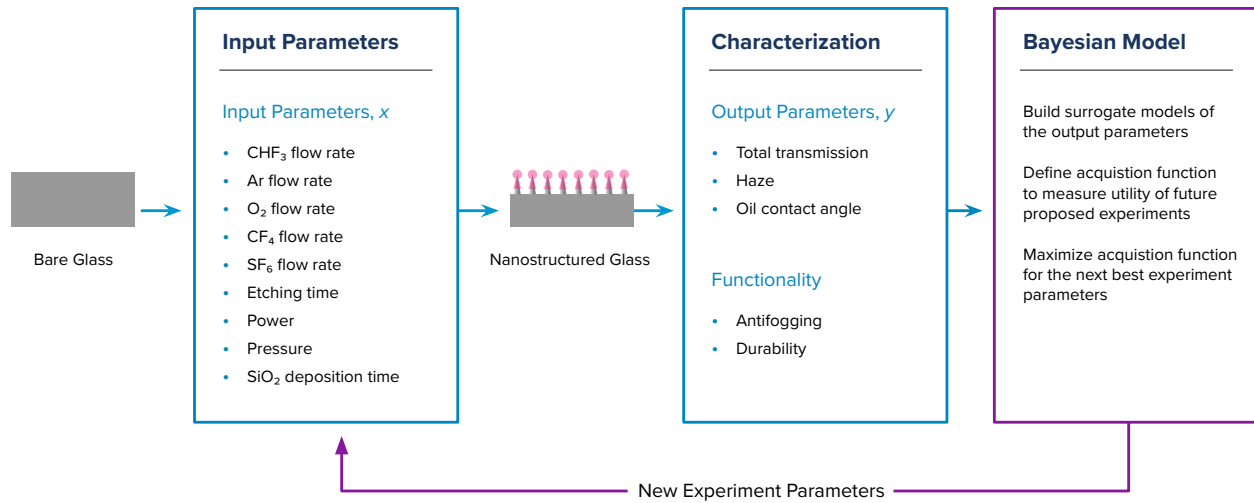


Figure 35 Schematic of experimental fabrication and Bayesian learning optimization process for nanostructured glass.

onto the substrate surface by the electric field and react with the etch target material and competitive reactions of etching and deposition take place near the surface [145]. The morphology of the etched nanostructures depend strongly on the RIE process parameters such as the pressure, gas chemistry, and RF power.

The second processing step focuses on creating re-entrant structures and a low energy surface. In this processing step, we consider the deposition of silicon dioxide (SiO₂) by PECVD on top of the sub-wavelength nanostructures in order to make the structure re-entrant followed by fluorination. We focus on varying the deposition time, which affects the amount of silicon dioxide deposited, while all the other processing parameters are fixed. Previous research has demonstrated that a concave (re-entrant) surface formed by roughness upon microscale features results in local energy minimization and these surfaces are capable of pinning the liquid-air interface. These structures stabilize the Cassie-Baxter wetting state, which results in high contact angle for different liquids with various surface energy [181, 182]. In PECVD, the pressure of the chamber and the power were set at 900 mTorr and 60 Watt, respectively. The flow rate of silane/nitrogen (SiH₄/N₂) and dinitrogen monoxide (N₂O) were both 140 sccm. The thickness of the SiO₂ layer can be

controlled by the deposition time. In our process, the deposition rate was approximately 110 nm/min. The temperature of the PECVD chamber was fixed at 400 °C. The structures were modified with fluoro-silane after SiO₂ deposition to create a low surface energy surface by spin coating method. Tridecafluorooctyl triethoxysilane (FAS, Dynasylan F 8261) was mixed with trimethoxy silane (with ratio of 5:1 vol %) and the solution was dispersed in ethanol (5:1 vol %)[181]. The final solution was spin coated on the glass substrates for 60 s at 1500 rpm, followed by annealing at 95 °C for 10 min. The substrates were then cleaned with acetone and dried with nitrogen.

Fig. 35 shows the schematic of fabrication and optimization process. Nine input process parameters were considered: (1) the CHF₃ flow rate, (2) the Ar flow rate, (3) the O₂ flow rate, (4) the CF₄ flow rate, (5) the SF₆ flow rate, (6) the etch time, (7) the radio frequency (RF) power, (8) the pressure of the etch chamber, and (9) the SiO₂ deposition time. The first eight parameters are associated with the first processing step, while the last parameter is associated with the second processing step. We focused on optimizing three output parameters: (1) maximize oil static contact angle, (2) maximize transparency, and (3) minimize haze.

The optical properties were characterized using a spectrophotometer (PerkinElmer, Lambda 750), equipped with a 60 mm integrating sphere. The angle-resolved reflection spectra was measured on an Agilent UV-Vis-NIR Cary-series spectrophotometer system. A large (6°) detector aperture was used to ensure all light was collected from the narrow source beam (1° apertures) at high incident angle. At each angle the reflection spectra was collected in a narrow band around 550 nm (±5 nm) in 1-nm increments and averaged. This process was performed for both TE- and TM-polarizations. The unpolarized spectra were calculated from the average of the TE and TM polarized light.

The liquid contact angles were measured using an Attension Theta optical tensiometer. For the condensation test, a humidifier and dehumidifier were used to control and set the humidity of the system to specific values. Samples were held vertically, while a humidity control was used to set the humidity of the surrounding area to 80%. The Attension Theta optical tensiometer was used to observe the formation of droplets on the substrates. The relative humidity was sustained for 45 minutes.

5.1.3 Experimental design methodology

We consider the fabrication of nanostructured substrates as defined in the previous section, where we simultaneously want high performance photon management and wetting properties (Fig. 35), as a multiobjective optimization problem with solution x^* ,

$$x^* \text{ satisfies } \begin{cases} x^* = \arg \max_{x \in \mathcal{X}} \theta_o(x), \\ x^* = \arg \max_{x \in \mathcal{X}} T_{\text{total}}(x), \text{ and} \\ x^* = \arg \min_{x \in \mathcal{X}} H(x) \end{cases} \quad (5.1)$$

where \mathcal{X} is the space of all possible choices of the process parameters. We denote x to be both the fabrication process parameters and the resulting nanostructure from using those parameters. $\theta_o(x)$ is the oil contact angle, T_{total} is the total transmission, and H is the haze.

The total transmission and haze are optimized for wavelength $\lambda = 550$ nm, which is in the middle of the visible spectrum, and ethylene glycol was chosen as the oil.

In general, there is no unique structure x^* that is simultaneously optimal in all the objectives in (5.1). In lieu of such a point, the solution to such a multiobjective problem is often defined as the Pareto-optimal set, or Pareto-efficient frontier $\mathcal{P} \in \mathcal{X}$. Pareto optimal parameters $x \in \mathcal{P}$ evince a “balance” between objective function values, such that no $x' \in \mathcal{X}$ can yield better performance across *all* objective functions; any improvements in one metric would necessitate a loss in performance in at least one other metric (thus the sense of balance). A more thorough explanation of the topic can be found in multicriteria literature[31].

5.1.4 Standard Bayesian optimization

The substrate fabrication process described above is quite time-consuming, which necessitates an effective experimental design so as to quickly search the space \mathcal{X} for input parameters which perform well for all three objective functions. Bayesian optimization is a sample-efficient iterative search framework, where the relationship between process parameters and objective function values is unknown, and function evaluations (executing the fabrication and characterizing the resulting substrate) are expensive or time consum-

ing. Standard Bayesian optimization consists of two components: a probabilistic *surrogate model*, to model the objective function f , and an *acquisition function*, to determine which x parameters to next sample.

In a typical single objective Bayesian optimization setting, the objective function f is assumed to be a realization of a Gaussian process (GP) with mean function μ and a positive definite covariance kernel K , i.e., $f \sim \mathcal{GP}(\mu, K)$ [161, 35]. The mean and covariance functions are often defined to have certain free parameters which are fit to the data using strategies such as maximum likelihood estimation (which was our strategy of choice in this process). In all of our modeling, we assume our GPs to have $\mu \equiv 0$ and a square-exponential K with independent length-scales in each dimension. A Tikhonov parameter is fixed to be 10^{-3} , primarily to ease ill-conditioning concerns.

An acquisition function is a utility function that measures the value of sampling at different points within \mathcal{X} , given what data has already been observed. Acquisition functions balance the trade-off between *exploitation*, suggesting input parameters near where we have the best results so far, and *exploration*, suggesting input parameter in regions where we have not tried out. After n different input parameters have been tested, the n th surrogate model can be created, which allows the formation of the acquisition function, which is then maximized to determine the x_{n+1} input parameter selection at which to run the fabrication process.

5.1.5 Modifications to Bayesian optimization

We describe our adaptation of Bayesian optimization to efficiently search for input parameters which address (5.1). The strategy has some decisions unique to this scenario, but can be generalized to an arbitrary number of objectives.

First, unlike the traditional sequential nature of Bayesian optimization, we chose to run 5 simultaneous fabrication processes. This allowed us to accelerate the parameter search, which was valuable because the fabrication process can take more than a couple hours. The specifics of this parallel Bayesian optimization [201] are explained later.

The strategy is derived from the ϵ -constraint method [83]. We transform the multi-objective optimization problem (5.1) to three constrained scalar optimization problems:

$$\max_{x \in \mathcal{X}} T_{\text{total}}(x), \quad \text{s.t. } H(x) \leq \hat{H} \quad \text{and } \theta_o(x) \geq \hat{\theta}_o, \quad (5.2a)$$

$$\min_{x \in \mathcal{X}} H(x), \quad \text{s.t. } T_{\text{total}}(x) \geq \hat{T}_{\text{total}} \quad \text{and } \theta_o(x) \geq \hat{\theta}_o, \quad (5.2b)$$

$$\max_{x \in \mathcal{X}} \theta_o(x), \quad \text{s.t. } T_{\text{total}}(x) \geq \hat{T}_{\text{total}} \quad \text{and } H(x) \leq \hat{H}, \quad (5.2c)$$

where \hat{T}_{total} , \hat{H} and $\hat{\theta}_o$ are pre-defined thresholds. These quantities define *viability* for this experimental setting – we only consider parameter choices x to be viable if all three constraints are satisfied, i.e.,

$$\theta_o(x) \geq \hat{\theta}_o \text{ and } T_{\text{total}}(x) \geq \hat{T}_{\text{total}} \text{ and } H(x) \leq \hat{H}. \quad (5.3)$$

For the parameter search conducted here, $\hat{\theta}_o = 60^\circ$, $\hat{T}_{\text{total}} = 88.5\%$, and $\hat{H} = 1.1\%$.

Another modification to the standard Bayesian optimization methodology accounts for the physical limitations in the precision of executing a proposed fabrication strategy. The parameters defining \mathcal{X} are fundamentally continuous (e.g., the etching time can be any positive real number), but the actual tooling and machinery used in the fabrication process have limited precision and small changes in the input parameters do not result in quantifiable differences in the created structure. As a result, the actual domain under analysis is a discrete domain designed to account for a minimum difference (distance in parameter space) between proposed fabrication strategies. That space is:

- CHF₃ flow rate: $\{0, 5, \dots, 80\}$ sccm,
- Ar flow rate: $\{0, 5, \dots, 100\}$ sccm,
- O₂ flow rate: $\{0, 5, \dots, 100\}$ sccm,
- CF₄ flow rate: $\{0, 5, \dots, 80\}$ sccm,
- SF₆ flow rate: $\{0, 5, \dots, 80\}$ sccm,
- Etching time: $\{0, 60, \dots, 5400\}$ seconds,
- Power: $\{20, 30, \dots, 300\}$ watts,
- Pressure: $\{50, 100, \dots, 250\}$ mtorr,
- SiO₂ deposition time: $\{8, 10, \dots, 500\}$ seconds.

Because the circumstances of (5.2) are more complicated than a standard Bayesian optimization setting, we require more complicated models and a modified acquisition function. We adapt methods from constrained Bayesian optimization literature[51]. After k fabrications have been conducted, Gaussian process models $s_{T,k}$, $s_{H,k}$ and $s_{\theta,k}$ are created for the transmission, haze and contact angles, respectively. These are modeled independently, though in future work we could consider a joint model.

Using these models, an acquisition function is defined for each component of (5.2). This acquisition function is modified from the expected parallel improvement[53] to account for the desire for viability. Considering, at first, only the solution to (5.2a), imposing the viability requires us to consider not only the distribution of $t \sim s_{T,k}(x)$ (a Gaussian distribution), but the joint distribution $t, h, z \sim s_{T,k}(x), s_{H,k}(x), s_{\theta,k}(x)$, more succinctly denoted by $t, h, z \sim s_k(x)$. The acquisition function (without parallel suggestions) would be defined as

$$a_{T,k}(x) = \mathbb{E}_{t,h,z \sim s_k(x)}[(t - \tilde{t}_k)_+ I_{h < \hat{H} \cap z > \hat{\theta}_o}], \quad (5.4)$$

where \tilde{t}_k is the highest T_{total} value observed thus far, $(\xi)_+$ denotes $\max(\xi, 0)$, and $I_\nu = 1$ if the condition ν is satisfied and 0 otherwise (the indicator function). This is semantically equivalent to maximizing the *expected improvement* attainable for viable points; points which do not satisfy our thresholds contribute zero improvement.

To account for the desire for 5 parallel suggested parameters, we expand on the base structure of (5.4). This requires taking draws of our models at 5 different input parameter $x_1, \dots, x_5 \in \mathcal{X}$ values. We denote this with the shorthand notation

$$\mathbf{t}, \mathbf{h}, \mathbf{z} \sim s_k(\mathbf{x}) \iff t_1, h_1, z_1, \dots, t_5, h_5, z_5, \sim s_k(x_1), \dots, s_k(x_5),$$

which allows us to write the expected parallel improvement, attenuated by viability, as

$$a_{T,k,5} \begin{pmatrix} x_1 \\ \vdots \\ x_5 \end{pmatrix} = \mathbb{E}_{\mathbf{t}, \mathbf{h}, \mathbf{z} \sim s_k(\mathbf{x})} \left[\max_{1 \leq i \leq 5} (t_i - \tilde{t}_k)_+ I_{h_i < \hat{H} \cap z_i > \hat{\theta}_o} \right]. \quad (5.5)$$

In practice, the quantity (5.5) is estimated through 4000 Monte Carlo iterations, utilizing our ability to independently draw from Gaussian distributions $s_{T,k}(x)$, $s_{H,k}(x)$, $s_{\theta,k}(x)$; the probability of viability impacts (5.5) implicitly through the indicator function, and thus no explicit model of viability probability is required. Analogous acquisition functions to (5.5) allow for optimizing H and θ_o subject to their viability constraints. We used the CMA-ES[74] optimization strategy (adapted to the aforementioned discrete parameter domain) to maximize all acquisition functions; the evolutionary population is 25, with 100 full iterations and 10 uniform random restarts.

Fig. 36 depicts the Bayesian optimization process in a sample problem reduced to one dimension for ease of understanding. In the first row, 6 locations have already been sampled of the three objectives. In the second row we demonstrate the Gaussian process models that have been built, and the resulting predictions. In the third row, we show the acquisition function (5.5) when considering sampling 3 points in parallel (instead of the 5 used for the 9 dimensional problem); we also show the explicit probability of viability estimated through Monte Carlo sampling (which is presented simply for display and is not required to compute (5.5)). In the final row, we show the Gaussian process models after being updated with data sampled at the 3 suggested points, which would then be used to generate 3 new points at which to sample.

5.1.6 Results and Discussion

Fig. 37 plots a summary of the experimental design and Bayesian optimization process. Sixty four experimental runs were conducted in total. The left component of Fig. 37 shows the three 2D plots depicting the objective values observed during the Bayesian optimization. In the optimization of the photon management properties (direct transmission vs. haze), only a single process condition or structure was determined to be Pareto efficient (the blue star). This indicates that the total transmission and haze are strongly correlated[44]. As a baseline, smooth glass has 93.5% transmission and 1.5% haze at 550 nm wavelength. After 22 experimental runs, the transparency increased to 97.0% while the haze value was reduced to 0.1%.

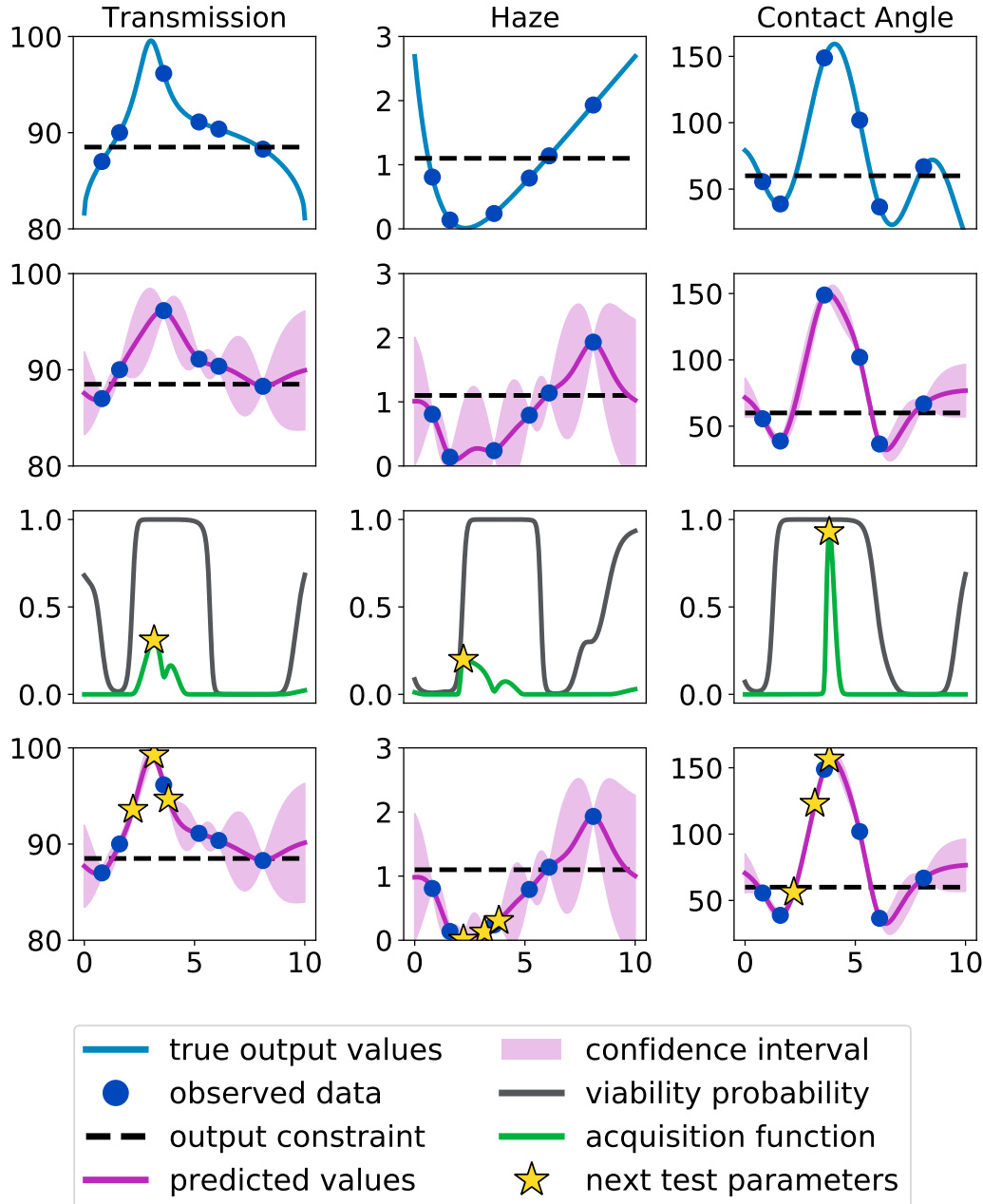


Figure 36 Sample depiction of our proposed Bayesian optimization process; each column represents one of the three output parameters under consideration. These are artificial profiles in one dimension for explanatory purposes only.

First row: The “true” output parameter to be optimized.

Second row: Statistical models built from the observed data.

Third row: The probability of an input parameter being viable (satisfying the constraints for the other two output parameters) and the associated acquisition function values along with the points which maximize the acquisition function.

Fourth row: The new observations achieved by sampling at the “next test parameters” and the new models which result from this new data.

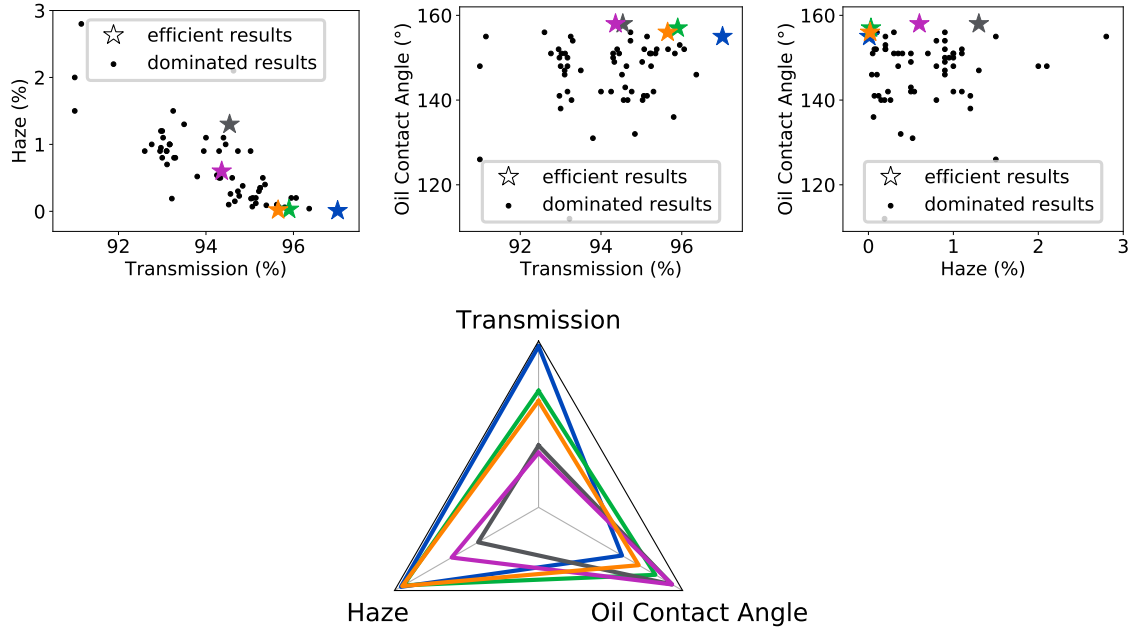


Figure 37 Depictions of the experimental design driven by our Bayesian optimization methodology. *left*: Three 2D feasible region plots of the three objectives under consideration. *right*: Radar plot of the 5 viable efficient outcomes identified during the parameter search (plot qualitatively exaggerated to account for the different scales of the three objectives).

The remaining 42 experimental runs conducted were spent balancing high performance of the photon management properties against the substrate's omniphobicity. By the end, 5 sets of input parameters were identified which are considered viable (satisfy the stated constraints) and Pareto efficient. The trade-off between the objectives is depicted in the rightmost graph of Fig. 37.

5.1.7 Characterizing the nanostructured glass properties

We further characterize the optimally performing nanostructured glass identified from our parameter search. We focus on characterizing the nanostructured glass associated with the blue star in Fig. 37, which has the best optical properties compared with other Pareto efficient data points. Fig. 38(a) shows SEM images of the sub-wavelength, re-entrant structure. Fig. 38(a)(i) shows 20° tilted SEM image and Fig. 38(a)(ii) and Fig. 38(a)(iii) show

cross sectional SEM images with different magnifications. The height of the pillars are approximately 100-500 nm and the distance between the pillars are between 20-100 nm. The diameter of the pillars are between 30-40 nm at top and 10-20 nm at bottom. The randomness in the height and spacing provide for broadband and omnidirectional antireflection like the glasswing butterfly wings [171]. Furthermore, this randomness also provides for robustness against abrasion as will be discussed later. By depositing the SiO_2 , the surface area at the top of the pillars increase which provide the re-entrant structures required for omniphobicity.

To investigate the omniphobic property, we deposited drops of different liquids with different surface tensions, from water (72.8 mN/m) to ethylene glycol (47.7 mN/m), on both bare and nanostructured substrates. The volume of droplets was 5 μl . Three measurements were made for each sample and the mean and standard deviation for each sample are reported. Fig. 38(b)(i) shows the static contact angle of a variety of liquids on top of normal glass. The bare fused silica has $42.9 \pm 1.1^\circ$ and $18.7 \pm 0.7^\circ$ contact angle for water and oil, respectively, with $35.5 \pm 2.7^\circ$ hysteresis value for water. The hysteresis value for oil is not measurable, because it is very close to the contact angle. By creating re-entrant structure on the bare fused silica, the water and contact angles increase significantly to $162.1 \pm 2.0^\circ$ and $155.2 \pm 2.2^\circ$ with $3.2 \pm 0.7^\circ$ and $9.4 \pm 3.6^\circ$ hysteresis, respectively (Fig. 38(b)(ii)). The contact angle for milk, coffee, blood, cranberry juice, orange juice, and water are all more than $158.0 \pm 3.0^\circ$ with hysteresis less than $8.0 \pm 2.0^\circ$. Also, as shown in Fig. 38(b)(ii), the transparency of the nanostructured glass is high enough that the text beneath the substrate is clearly visible. Fig. 38(c)(i) and Fig. 38(c)(ii) show the total transmission and haze results for glass as a function of wavelength. As shown in Fig. 38(c)(i), the total transmission for bare fused silica is 93.5% and increases to 97.0% at 550 nm. The transmission spectra for both the bare glass and single-side nanostructured glass are fairly flat across the entire range of 280 to 1000 nm wavelength. The total transmission for the bare glass is between 93.1% to 94.0%, and the total transmission for the nanostructured glass is between 95.9% to 97.1%. The total transmission of double-side nanostructured glass at 550 nm is 99.5%. The transmission spectra for the double-sided glass are also fairly flat with total transmission between 98.1% to 99.9%. The corresponding values for haze

are shown in Fig. 38(c)(ii). In both single-side and double-side nanostructured glass, the haze value reduces to less than 0.1% across a broadband range of wavelength. For normal glass the haze value is between 2.2% and 0.9%; however, for nanostructured glass the haze value is fairly flat for the spectrum.

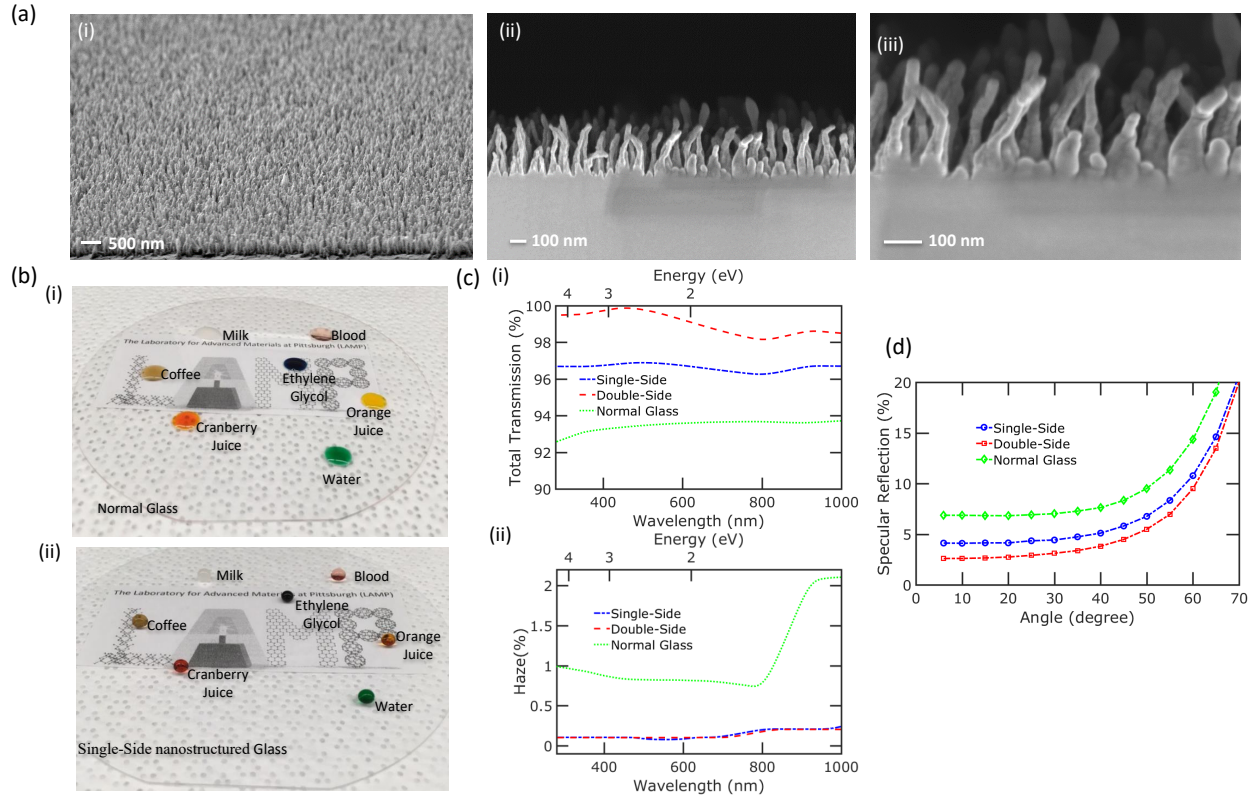


Figure 38 (a) shows (i) 20° tilted, (ii) and (iii) cross sectional SEM images of fabricated glass with different magnifications. (b) shows the droplet of different liquids on (i) normal and (ii) our superomniphobic glass. (c) (i) show transmission and (ii) haze plots as a function of wavelength for bare, single side and double side etched glass (d) Angle-resolved spectra for reflection at 550 nm wavelength for bare, single side and double side etched glass.

Angle-resolved spectra of specular reflection was recorded at 550 nm wavelength. Fig. 38(d) shows the angle dependent specular reflection for normal glass, single side, and double side nanostructured glass. All the values of reflection for etched glass are less than 5% for both single side and double side etched glass up to 45°. However the reflection values are always less than glass even for a high incidence angle of 70°, which reveals the high omnidirectional, anti-reflective performance of our fabricated glass.

5.1.8 Characterizing the nanostructured glass functionality

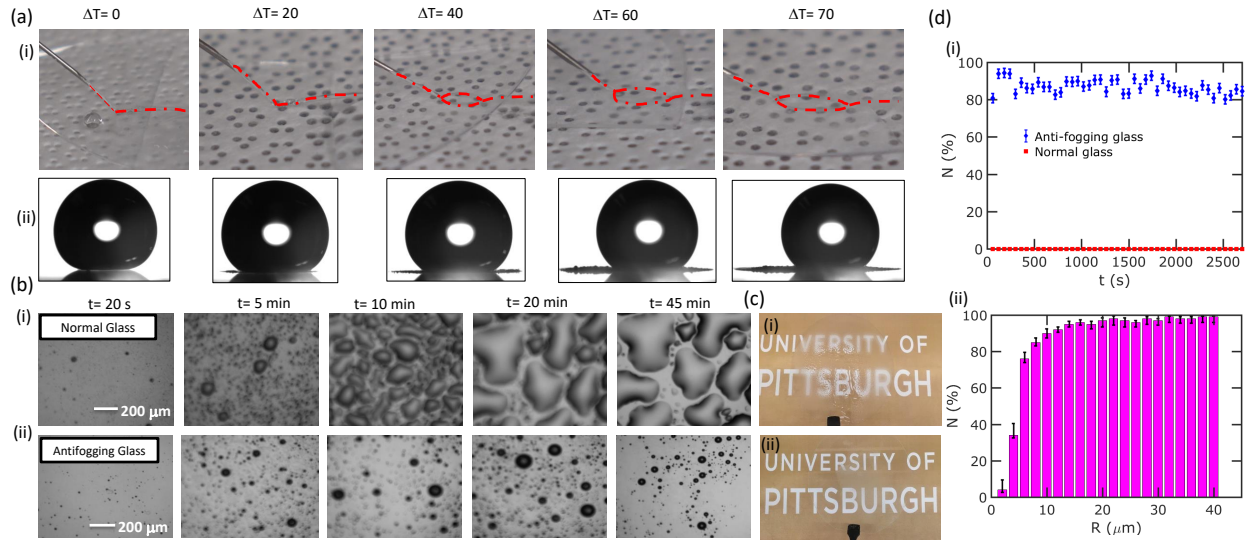


Figure 39 (a) (i) shows water jet behaviour as a function of temperature ΔT . (a)(ii) shows the water contact angle at different ΔT on anti-fogging glass. Condensation versus time optical images of (b)(i) normal glass and (b) (ii) anti-fogging glass. (c) shows optical image of (i) normal and (ii) anti-fogging glass after 45 min of condensation. (d) (i) plot of percentage of jumping droplets after coalescences versus time. (c)(ii) Relationship of percentage of coalescences droplets jumping and radius of the droplet at the moment of jumping.

We characterized the water-repellency of the nanostructured glass when exposed to fog. The nucleation of small droplets in the structure may destroy the superhydrophobicity of the surface [188]. However, nanostructured texturing as well as reentrant structures may provide for efficient antifogging by preventing nucleating droplets from growing within the structure and transition to a Wenzel state of wetting [133, 197]. To produce condensation, we dispense water at an elevated temperature T_L compared to a constant surface temperature T_S . Water evaporates and condenses on the surface. By increasing the difference between the temperature of the water and surface ($\Delta T = T_L - T_S$, where T_L and T_S are the temperature of liquid and surface, respectively), the amount of condensation increases. Fig. 39(a) shows water jets dispensed with different ΔT on our nanostructured glass (the rate of dispense estimated as 20 ml/min). The results shows that by increasing the ΔT , when the jet reaches the sample, the wetting area increases (Fig. 39(a)(i)) and

a number of small water nuclei form (Fig. 39(a)(ii)). However, even with $\Delta T = 70$, the surface retains its superrepelency of water as the droplet can move easily by blowing it off, even without tilting the sample. The small water nuclei retain their spherical shape even as they evaporate and easily roll along the surface even at the minimum observable diameter of $5 \pm 1.0 \mu\text{m}$. The corresponding breakthrough pressure associated with this diameter is $30 \pm 6.0 \text{ kPa}$ [19].

We also characterized the anti-fogging properties of nanostructured glass by placing the samples in high relative humidity conditions of 80%, which were enough to create fog on the glass. Fig. 39(b)(i) and Fig. 39(b)(ii) show the evolution of fog formation on normal and our nanostructured glass, respectively. In a short time, high density micro-droplets nucleate on both substrates. The difference between normal and anti-fogging glass, however, becomes apparent after few minutes. While the nucleated droplets grow and coalescence on the normal glass, without jumping out of the substrate, the water droplets on the anti-fogging glass merge together fast and they jump out of the substrate, which provide new nucleation sites for new droplets. This process continues for the whole recorded time. The optical images of normal glass and antifogging glass after 45 min condensation are shown in Fig. 39(c)(i) and (ii), respectively.

To quantify the anti-fogging efficiency, we measured the proportion N of drops jumping off the glass after coalescence[133]. After approximately 5000 coalescences, N versus time is plotted in Fig. 39(d)(i) by counting the jumping droplets in one minute. For the normal glass, N is essentially zero for all time because no droplets jump after coalescence. However, for the nanostructured glass, more than 90% of the coalesced droplets jump off the surface when the size of droplets becomes large enough. The antifogging properties of our nanostructured glass is comparable with the reported values for nanocones with remarkable antifogging abilities [133]. Fig. 39(d)(ii) shows N as a function of droplet radius at the moment of jumping. The droplets start to jump as soon as their size is as small as $2 \mu\text{m}$. The percentage of jumping droplets increase with size of droplet and 99% of droplets above $12 \mu\text{m}$ jump of the sample. Almost all of the droplets ($N \approx 99\%$) with larger size have jumped out of the substrate.

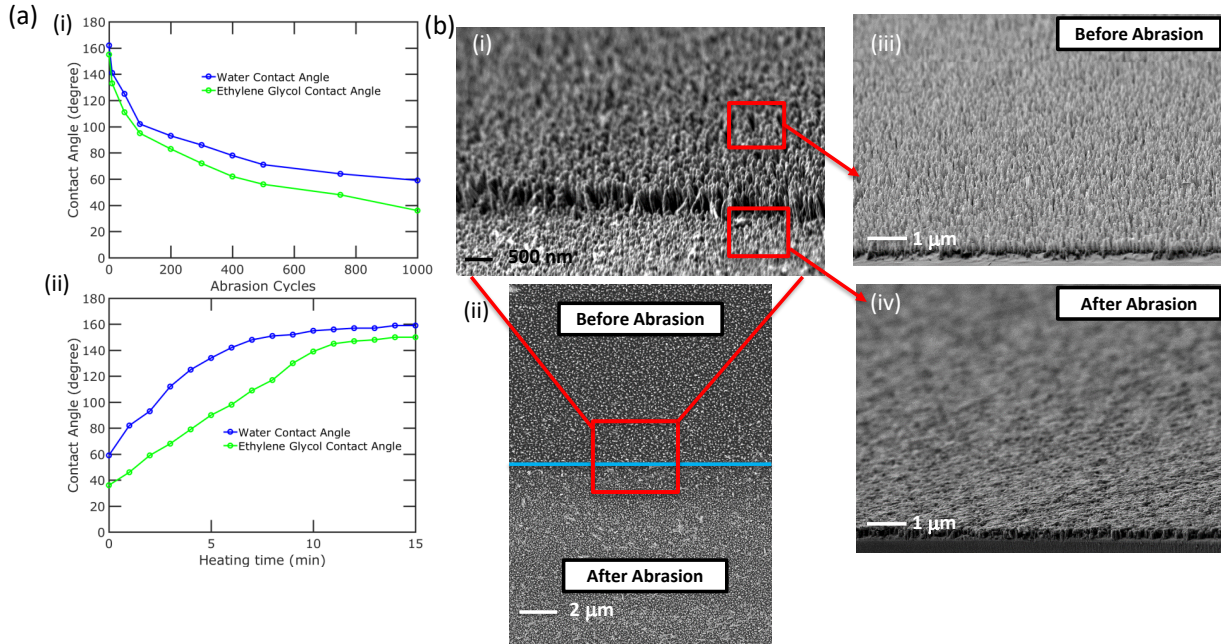


Figure 40 (a) Water and oil contact angle versus (i) abrasion cycle and (ii) after heating the abraded samples. (b) Shows SEM images of (i) 20° tilted and (ii) overhead view of abraded and non-abraded structure with wider view of (iii) non-abraded and (iv) abraded area.

The mechanical durability of our glass surface comes from two features: its randomness and self-similar structure and ability to self-heal. A Taber Linear Abraser (model 5750) with weighted SCOTCHBRITE abrasive pad was used for abrasion of the samples on a constant surface area of $4 \times 10^{-3} \text{ m}^2$. Fig. 40(a)(i) shows the behavior of water and ethylene glycol contact angle during repeated abrasion cycles with pressure of 1225 N/m^2 . For both water and oil, the contact angles decrease to less than 90° after approximately 400 cycles of abrasion. However, the mobility of fluorine molecules provides a path for self-healing, similar to that of epicuticular wax in plant cuticles [139]. Fig. 40(a)(ii) shows how the water and oil contact angle increase after a heat treatment at 95°C . After only 15 minutes of heating, the contact angles for both liquids recover. Fig. 40(b)(i) and (ii) show SEM images of tilted and overhead view of the interface between abraded and non-abraded areas of the sample after 500 cycles of abrasion with 1225 N/m^2 of pressure. The height of the nanostructures decrease, but their reentrant shape is similar to the structure before the abrasion. The randomness of the structures and self-similarity are such that

abraded surfaces are similar in texture to the non-abraded surfaces. Fig. 40(b)(iii) and (iv) show the uniformity of the structures over a wide area for non-abraded and abraded samples.

5.1.9 Conclusion

In conclusion, we report superomniophobic, high transmission re-entrant nanostructured on glass substrates created using a Bayesian optimization powered experimental design process. The antireflective, superomniphobic glass showed 97.0% and 99.5% total transparency at 550 nm wavelength, for single side and double side nanostructured glass, respectively. In addition, static water and ethylene glycol contact angles of $162.1 \pm 2.0^\circ$ and $155.2 \pm 2.2^\circ$ for fused silica glass have been achieved. The hysteresis for these liquids on glass are $3.2 \pm 0.7^\circ$ and $9.4 \pm 3.6^\circ$, respectively. Also, the superomniphobic glass can recover its characteristics and heal itself after abrasion through a brief period of heating. The nanostructured glass showed $N \approx 99\%$ antifogging efficiency for broad range of water condensation droplets. In using Bayesian optimization, we explored a complex input parameter space with competing goals to identify and fabricate multifunctional substrates with a very small number of experiments. These substrates can be used in large variety of optoelectronic applications.

5.2 Discovering Near-Perfect Broadband and BroadAngle Antireflection Surfaces for Optoelectronics by Machine Learning

5.2.1 Introduction

Optoelectronic devices such as touch screens, phones, tablets, laptops, and light emitting diodes (LEDs) typically consist of a top glass sheet that protects the device from the environment. Antireflection is important in this glass for improving the outcoupling efficiency of light in displays or LEDs, augmenting the responsivity of sensors, or increasing the power conversion efficiencies of solar modules. AR is often needed across a range of

wavelengths such as the visible range or the solar spectrum and is often desired across a wide range of incidence angles. Broad angle AR may increase viewing angles in displays or LEDs or increase power conversion efficiencies in solar modules.

A single layer (SL) thin film of AR coating can provide for perfect AR at one particular wavelength and normal incidence. However, these thin films cannot demonstrate high AR across a wide range of wavelengths and incidence angles. An alternative approach is to use sub-wavelength nanostructures [73]. Extensive research efforts have been devoted to construct nanostructured AR materials to reduce light reflection [85, 150, 185]. These nanostructures have included nanowires (NW) [185] and nanocones (NC) [222]. Groep *et al.* showed that NW arrays can reduce normal reflection to 0.97% across the solar spectrum when the NWs are fabricated on a both sides of the glass substrate, but did not measure reflection at higher angles across a broad range of wavelengths [185]. Many NC-like structures have also been fabricated in the literature by methods such as maskless reactive ion etching (MRIE) followed by plasma enhanced chemical vapor deposition [67], metal dewetting [85], interference lithography [150], soft imprint [185], nanoparticle dip-coating and precursor-derived one-step assembly [89], as well as ultrasonic-assisted sol-gel [219]. The performance of the NC-like structures from these various fabrication methods will be discussed in more detail later on in the text. These studies demonstrate some of the potential of NW and NC arrays in providing broadband and broad angle AR. However, there has yet to be a comprehensive study on the fundamental performance limits of these nanostructures for broadband and broad angle AR.

In this project, we studied the optimal AR characteristics of SL films, NW arrays, and NC arrays for minimizing solar integrated reflection across a broad range of wavelengths and incidence angles. A Bayesian learning and optimization method was combined with electrodynamic simulations to rapidly search through the parameter space of various structures and determine optimal and near-optimal structures. We demonstrate that NC arrays exhibit the best performance for both broadband and broad angle AR. NW arrays only demonstrate performance comparable to SL thin films, where NWs function as an effective medium with index of refraction about the same as the optimal thin film. The NCs grade the index of refraction and have the best performance when the bottom of the nanocones

fill out the surface to provide for a smooth change in index of refraction with the flat glass. The NCs have a narrow optimal or near-optimal angle of 76 to 87°. Our simulations suggest that NC arrays can demonstrate a minimum solar-integrated reflection of 0.15% at normal incidence and 1.25% at 65° incidence or solar-integrated reflection of 0.78% at 65° and 0.23% at normal incidence. We demonstrate and validate the simulation results by fabricating NC structures with MRIE as well as nanosphere lithography and compare their performance. NC arrays fabricated by MRIE on both sides showed a solar integrated reflection of 0.9% for normal incidence and reflection of 6.7% at 65° incidence.

5.2.2 Results and discussion

The first part of our study focused on electrodynamic simulations to study solar integrated reflection. We focused on minimizing two objective functions: the solar integrated reflection across the wavelengths 280-1200 nm at (1) normal incidence ($R_{solar,0^\circ}$) and (2) 65° incidence angle ($R_{solar,65^\circ}$). The solar integrated reflection R_{solar} is calculated from

$$R_{solar} = \frac{\int b_s(\lambda)R(\lambda)d\lambda}{\int b_s(\lambda)d\lambda} \quad (5.6)$$

where $R(\lambda)$ is the reflection spectrum or the reflection as a function of wavelength λ and $b_s(\lambda)$ is the photon flux density of the AM1.5 global solar spectrum [1]. $R_{solar,65^\circ}$ is calculated by averaging the solar-integrated reflection for transverse electric (TE)-incident light and transverse magnetic (TM)-incident light at 65°. Assuming normal incidence light at solar noon, an incidence angle of 65° corresponds to 4 hours 20 minutes before and after solar noon.

Fig. 41(a) shows schematics of the three types of structures studied: (i) SL films, (ii) NW arrays, and (iii) NC arrays. The SL film is defined by only its thickness t . For the SL film, the material was assumed to have a wavelength-independent index of refraction that is the geometric mean of the materials on its sides, $n_1 = \sqrt{n_0 n_2}$. $n_1 = 1.21$ was used for the SL film, since $n_0 = 1$ for air and $n_2 = 1.46$ for glass. The NW array is defined by its pitch (a), height (h) and diameter (d). The NC arrays are defined by the four variables, pitch (a), height (h), top diameter (d_{top}), and bottom diameter (d_{bot}). In the special

case, $d_{top} = d_{bot}$, the NC array is a NW array. The domains over which the optimization took place for the NW array was $a \in [1, 400]$ nm, $d \in [1, 400]$ nm, and $h \in [1, 800]$ nm with the constraint $d \leq a$. For the NC array, the domains were $a \in [1, 400]$ nm, $d_{bot} \in [1, 400]$ nm, $d_{top} \in [1, 400]$ nm, and $h \in [1, 800]$ nm with the following constraints: $d_{bot} \leq a$ and $d_{top} \leq d_{bot}$.

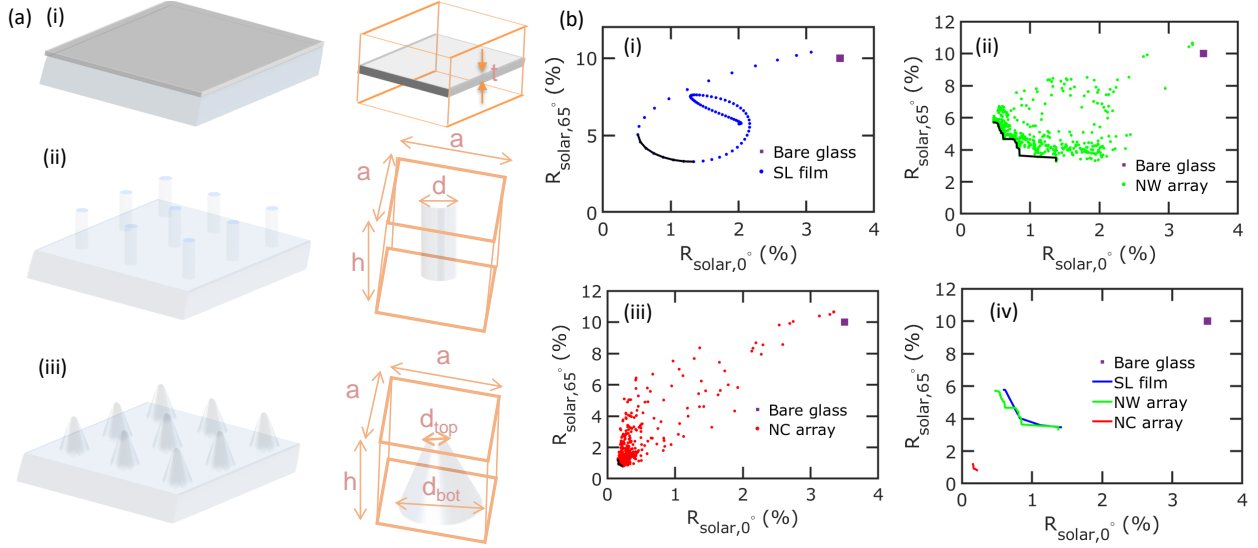


Figure 41 Bayesian learning and optimization of electrodynamic simulation results. (a) Schematic of (i) SL thin films, (ii) NW arrays, and (iii) NC arrays. (b) Scatter plots and Pareto frontier of $R_{solar,0^\circ}$ and $R_{solar,65^\circ}$ for (i) SL films, (ii) NW and (iii) NC arrays. (iv) Comparison of the Pareto frontier for all structures.

The finite difference time domain (FDTD) method [213] was used for optical simulations. Simulations were set up so that the reflection from only a single air/glass interface was measured. Please see Appendix B for simulation details. To search for the Pareto efficient frontier which minimizes both $R_{solar,0^\circ}$ and $R_{solar,65^\circ}$, we employ Bayesian optimization [40]. Bayesian optimization is an active machine learning-based strategy which attempts to efficiently balance a desire to learn how the structure parameters influence the reflection with a desire to more completely refine the knowledge regarding the minimal reflection values. In this setting, where there are two competing metrics, we leverage a multiobjective Bayesian optimization strategy powered by constrained Bayesian optimization [51].

Fig. 41(b) shows the scatter plot and Pareto frontier of $R_{solar,0^\circ}$ (x -axis) and $R_{solar,65^\circ}$ (y -axis) for (i) SL films, (ii) NW arrays, and (iii) NC arrays. The performance of bare glass is shown for reference in each of these plots with a purple box. For the NW and NC arrays, Bayesian learning and optimization was performed with a budget of 500 simulations. For the SL film, the thickness of the films was changed from 0 nm to 800 nm in 10 nm increments. Fig. 41(b)(iv) compares the Pareto frontier of the SL films, NW arrays, and NC arrays. The SL films, NW arrays, and NC arrays all show better performance than bare glass. The Pareto points for the SL films and NW arrays show comparable performance and there is no significant difference between the Pareto line for these two systems. Overall, NC arrays demonstrate the best and near perfect broadband and broad angle AR properties. NC arrays can demonstrate a minimum $R_{solar,0^\circ} = 0.15\%$ with corresponding $R_{solar,65^\circ} = 1.25\%$ or minimum $R_{solar,65^\circ} = 0.78\%$ with corresponding $R_{solar,0^\circ} = 0.23\%$.

Next, we performed some post-hoc analysis of the computations conducted during the search for the efficient frontier; we analyze the effect of geometry on optimal or near-optimal as defined by Pareto efficiency. Here, near-optimality refers to the points being close to a point on the efficient frontier and accounts for some of the numerical error in the simulations due to finite grid size and simulation time. Fig. 42(a) presents the post-hoc analysis of NW array simulations, where (i) a parallel axes plot, (ii) feasible outcomes plot, and (iii) scatter plot are shown. For the NW arrays, efficient solutions only appear with h in the domain $[140, 220]$, despite the full problem domain being $[0, 800]$. The combination of low height h plus larger diameter d (in consistent proportion to pitch a) suggests that the structures with lowest reflection tend to have more of a flat disk shape than a high aspect ratio wire shape. These structures occupy approximately 41% of the surface of the glass. This fill factor makes the effective index of refraction of these NW arrays (using the effective medium approximation) about 1.28, which is close to 1.21 of an ideal SL film. The NWs function as an effective medium and thus, overall, can only give about the same performance as an SL film.

Fig. 42(b) presents the post-hoc analysis of the NC array simulations with (i) parallel axes plot, (ii) feasible outcomes, and (iii) scatter plots, which have a very different spread of Pareto efficient outcomes compared to NWs. Of greatest note when looking at Fig. 42

is $d_{bot} = a$ for all efficient configurations. This implies that the reflection is minimized by maximizing the amount of material at the interface between the bottom of the NCs and the glass.

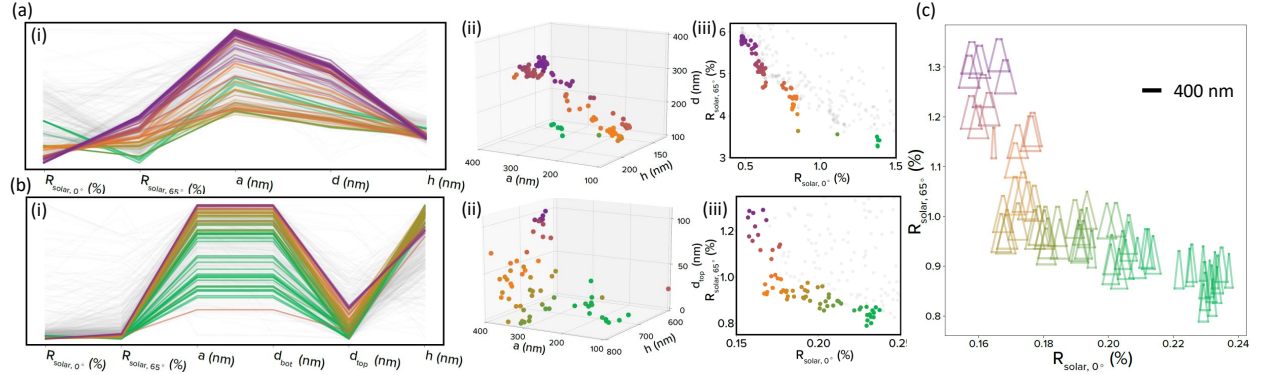


Figure 42 Post-hoc analysis of optimal and near-optimal (a) NW and (b) NC arrays with (i) parallel axes plot, (ii) feasible outcomes, and (iii) scatter plots. The colors are dictated by the location of nearly efficient outcomes along the Pareto frontier. (c) Nearly efficient outcomes for NC arrays, with the cross-sections of the NCs placed along the frontier.

From an effective medium analysis, this minimizes the discontinuity between the bottom of the cone with fill fraction $\pi/4$ and the top surface of the glass. This contrasts with the NW case where about 41% of the surface is covered. Fig. 42(b)(i) shows a strong negative correlation (although not a linear relationship) between a/d_{top} and $R_{solar,0^\circ}$. Having a smaller a/d_{top} reduces the discontinuity in the effective index of refraction between the air and the top of the NCs.

Fig. 42(c) shows a plot of the nearly efficient outcomes, but with cross-sections of the NCs placed along the frontier. In contrast with the NWs, is that all of the nearly efficient results have a height h in the domain of [600, 790] (note the range was 0 to 800 nm). Also, the nearly efficient results cluster around very small d_{top} values (less than 100 nm). These two factors combine to produce NCs which are taller and more pointed (unlike the NWs which were short and stout). Additionally, these NCs have a relatively consistent angle. While, mostly fatter NCs tend to demonstrate lower $R_{solar,0^\circ}$, slimmer NCs tend to reduce the $R_{solar,65^\circ}$. In both cases, when we fit a line relating d_{bot} to the angle of the NCs of the nearly Pareto efficient outcomes, we see the angles all fall within 76° to 87° .

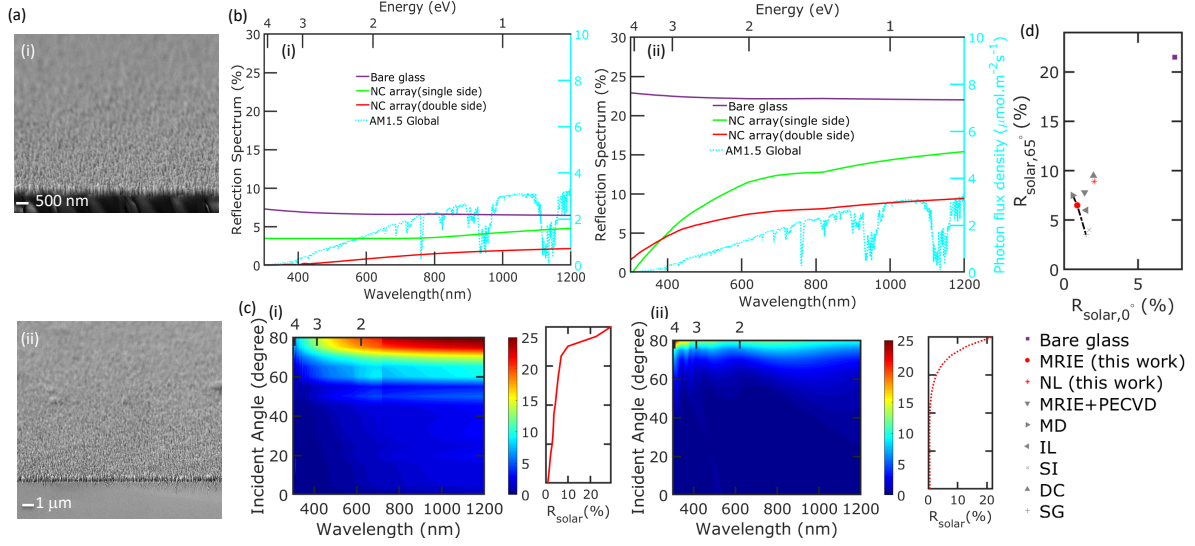


Figure 43 Experimental NC array results. (a) SEM images of NC array fabricated by MRIE. (b) Experimentally measured (i) $R_{0^\circ}(\lambda)$ and (ii) $R_{65^\circ}(\lambda)$ for bare glass and NC arrays. (c) R as a function of wavelength and incidence angle for (i) experiments and (ii) simulations. $R_{solar,0^\circ}$ versus $R_{solar,65^\circ}$ for bare glass and AR substrates fabricated by MRIE and nanosphere lithography (NL) (this work) compared with other NC-like structures in the literature. This includes MRIE followed by plasma enhanced chemical vapor deposition (MRIE+PECVD) [67], metal dewetting (MD) [85], interference lithography (IL) [150], soft imprint (SI)[185], nanoparticle dip-coating and precursor-derived one-step assembly (DC) [89], as well as ultrasonic-assisted sol-gel (SG) [219] .

NC arrays with a morphology similar to near-optimal simulated structures were fabricated on a single side as well as both sides of fused silica glass using MRIE methods developed by the authors [67, 64] (see Appendix A). Fig. 43(a)(i) and (ii) show SEM images of a fabricated NC array at different magnifications. The AR properties of fabricated samples were characterized by spectrophotometer. Fig. 43(b)(i) compares $R_{0^\circ}(\lambda)$ for bare glass and fabricated NC array on single side and double side of the glass. The photon flux density $b_s(\lambda)$ is plotted on the right y -axis. It should be noted that the experimentally measured reflection results are much higher than simulation results as experiments can only measure reflection through the entire substrate and two glass/air interfaces as oppose to our simulations which only characterize reflection from a single glass/air interface. The bare glass shows flat behavior in the wavelength range with $R_{solar,0^\circ} = 7.4\%$. The double side NC array shows excellent AR properties with $R(\lambda)$ between 0.3% to 2.6% for

λ between 400 and 1200 nm, with $R_{solar,0^\circ} = 0.9\%$. The $R_{solar,0^\circ}$ for single side NC array is equal to 3.3%. Figure 43(b)(ii) shows $R_{65^\circ}(\lambda)$ for bare glass and NC arrays on glass. Bare glass shows more than 21% reflection in the wavelength range, with $R_{solar,65^\circ} = 21.4\%$. The fabricated NC array on double side glass shows $R(\lambda)$ between 4.9% to 8.2% for the wavelength range, with $R_{solar,65^\circ} = 6.7\%$. $R_{solar,65^\circ}$ for single side NC array is 10.5%.

Fig. 43(c) shows contour plots of the reflection spectrum as a function of wavelength and incidence angle for (i) fabricated double side NC array samples and (ii) simulated similar structure, with $d_{top} = 120$ nm, $d_{bot} = 200$ nm, $a = 200$ nm, and $h = 620$ nm. Also, $R_{solar}(\%)$ as a function of angle plots are shown. For a wide range of angles and wavelength, for both simulation and experimental data, the plots are in blue range, which means that the reflection is less than 5% and there is a good agreement between simulation and experimental results.

We evaluate and compare the optical performance of our fabricated NC array, with other similar NC-like structures in the literature. Fig. 43(d) plots $R_{solar,0^\circ}$ and $R_{solar,65^\circ}$ for our experimental NC arrays as well as the other NC-like AR structures in the literature fabricated by different methods. All the data shown are from NC-like structures fabricated on both sides of the glass. The AR properties of other NC-like structures in the literature are not necessarily measured over the same wavelength range (280 - 1200 nm) and same incidence angles (0° and 65°), so the comparisons in Fig. 18(d) were made using the most comparable data provided. Table 1 in Appendix A provides the wavelength ranges and incidence angles used from each reference for creating Fig. 18(d). Our experimental data is plotted with a red circle for MRIE and a red star for nanosphere lithography. The Pareto frontier is shown with a black dotted line. Our NC array fabricated by MRIE is Pareto optimal. NC arrays were also fabricated by nanosphere lithography (NL). While NL offers some tunability in terms of NC size and spacing, the fabrication of NC arrays with very small inter-spacing distance as suggested by simulations is not possible by this method as the nanospheres must be etched first. In addition, NC-like AR structures formed from metal dewetting [85] and ultrasonic-assisted sol-gel [219] are also Pareto optimal where the first offers better normal reflection but worse broadband high incidence angle reflection and the second offers better high incidence angle reflection, but worse normal reflection.

5.2.3 Conclusion

In conclusion, we report using machine learning to find the best AR geometry for different AR coatings of SL films, NW arrays, and NC arrays. We showed that NC arrays have the best broadband and broad angle AR performance, where the NW arrays and SL films are comparable. Simulated NC arrays can demonstrate a minimum solar-integrated reflection of 0.15% at normal incidence and 1.25% at 65° incidence or solar-integrated reflection of 0.78% at 65° and 0.23% at normal incidence. We also provide physical insight into the performance of the different structures. MRE fabricated NC arrays on both sides of glass showed a solar integrated reflection of 0.9% for normal incidence and reflection of 6.7% at 65° incidence.

5.3 3D Printed Superomniphobic Structures With Ultra-Low Hysteresis, and High Abrasion Resistance

5.3.1 Introduction

Superomniphobic substrates defined as a surface with high contact angle ($> 150^\circ$) for water and various oils (with different surface tension), as well as small hysteresis angle ($< 10^\circ$) [149, 20, 4, 103, 181]. For having such a high liquid contact angle, based on the Cassie-Baxter model[15], the solid-liquid contact area needs to be minimized:

$$\cos \theta_{CB} = f_1 \cos \theta_{Y_1} + f_2 \cos \theta_{Y_2} \quad (5.7)$$

$$= f_1 \cos \theta_{Y_1} + f_1 - 1_{cassie} \quad (5.8)$$

where f_1 is the fraction of the surface that is in contact with the liquid. $f_1 + f_2 = 1$ and $\theta_{Y_2} = 180^\circ$ for air. Typically, Cassie-Baxter states show low adhesion at the solid-liquid interface. It is important to note that the contact angle in the equations is determined by the infinitesimal region at the contact line and independent of external factors such as pressure, drop size, gravity, curvature of a surface, or defects [167]. Generally, very

large amount of air mats under the droplet ($f_1 < 0.1$) creates both superhydrophobic and superoleophobic surfaces [126, 23]. Combination of hierarchical micro/nanostructures and hydrocarbon/fluorocarbon compounds are a common strategy for this purpose[67, 68].

Re-entrant geometry are demonstrated as the most efficient shape for repelling low surface tension liquids [116, 19]. A variety of re-entrant geometry structures have been demonstrated that can effectively impede penetration by various liquids, such as T-shaped microstructures [202], mushroom-like pillars [131, 19, 120], porous membranes[232], and springtail-inspired surfaces [217].

Fabrication of complicated re-entrant geometry usually involves multi steps. Recently 3D printing was used widely to make re-entrant geometry with high precision[120, 209, 81, 119]. However, multiple drawbacks such as poor mechanical durability and high rolling angles of the printed microstructures limit their application. Small rolling angle is a must for superomniphobic surfaces. While there are some applications for high rolling angle superomniphobic substrates[119], however, for a wide variety of applications such as self-cleaning [65, 138, 125], anti-fogging and condensation resistant substrates [67, 197, 133], stain resistant[68], and anti-icing [192, 129] substrates, low hysteresis (and low rolling angle) is a critical need.

Poor mechanical robustness, also, is a major challenge in superomniphobic surfaces in general, including 3D printed re-entrant pillars, which limits the implication of pillar-based surfaces in commercial applications. We observed that the printed pillar are destroyed after just a few cycles of abrasion and superomniphobicity is lost. While there are some effort on making self-compensating liquid-repellent surfaces[81], there is still an absolute need for fabrication of high mechanical durable surfaces for real life applications.

In this study, we address these challenges by introducing re-entrant walls in triangular array. To create this new re-entrant surface, we used two-photon polymerization based 3D printing technology that allows the fabrication of the micro re-entrant structures with high resolution. By using theoretical calculation for solid-liquid fraction and breakthrough pressure, we determined the feasible dimension for re-entrant walls geometry. For comparison purposes, we also fabricated re-entrant pillars with the same dimension reported

in Liu *et. al.* [120] work. Both re-entrant walls and pillars then coated with oleophobic nanoparticles to reduce the rolling angle. Our re-entrant walls showed static contact angle for water and ethylene glycol (EG) oil as $172.0 \pm 1.5^\circ$ and $161.0 \pm 2.5^\circ$, respectively. The hysteresis values for water and EG were $2.5 \pm 1.5^\circ$ and $4.5 \pm 2.0^\circ$, respectively. The abrasion experiments for re-entrant walls showed that the water and EG contact angle after 100 cycles of abrasion were $52.0 \pm 3.5^\circ$ and $145.0 \pm 5.5^\circ$, respectively, with $7.1 \pm 2.5^\circ$ and $13.0 \pm 6.5^\circ$, hysteresis, respectively. However, re-entrant pillars array, almost destroyed after the very first cycle of abrasion. The fabricated re-entrant wall array can find potential applications in various industries including but not limited to electronic devices, medical devices, and optoelectronics.

5.3.2 Results and Discussion

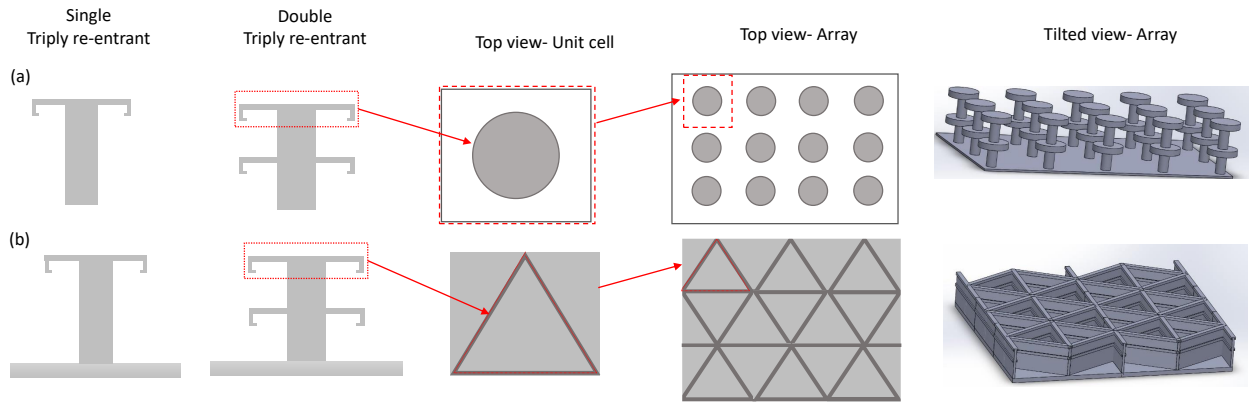


Figure 44 Schematic of Single, and double triply re-entrant configuration as (a) triangular walls array and (b) pillar array

Fig. 44 shows schematic of re-entrant (a) pillars and (b) walls. Liu *et. al.* [120] demonstrated that having double re-entrant parts, one at the top of the pillar and one at the middle of the height of the pillar, can improve the repellency for lower surface tension liquids, therefore we made double re-entrant part for both pillar and wall array. Also triply re-entrant shapes was used to enhance the liquid repellency. the unit cell, top view and side view of the pillars and walls arrays are also shown in the Fig. 44.

Two-photon absorption polymerization based 3D printing system (Photonic Professional GT, Nanoscribe GmbH) was used for printing the microstructures. Polished silicon wafer (thickness = 500 μm) used as substrates. The substrates were cleaned by ultrasonic rinse in acetone, isopropanol (IPA) and distilled water for 5 mins each, and then dried by nitrogen. The negative photoresist, IP-S (Nanoscribe GmbH) with a refractive index of 1.48 at 780 nm were used in the Dip-in Laser Lithography (DiLL) configuration. After printing, the samples were developed in SU-8 developer for 20 mins, followed by rinsing in IPA for 5 mins. Ultimately the samples were dried by gently blowing of nitrogen. To increase the adhesion of the walls to the silicon surface, first, a film (10 μm) of the resist printed on the silicon substrate then the wall array was printed on the resist film, as it is shown in Fig. 44(b). To reduce the rolling angle of different liquids, the printed structures were coated by Teflon oleophobic nanoparticles by nanosphere lithography[44], followed by drying on a hot plate at 100°C for 30 mins. The preparation of the nanoparticle solution is as follows: Tetraethyl orthosilicate, silica precursor (TEOS) (5ml), together with an appropriate amount of fluoroalkylsilane, perfluorinated compound (FAS), was dissolved in 25 ml ethanol. The solution was mixed with ammonium hydroxide/ethanol solution (6ml 28% $\text{NH}_3 \cdot \text{H}_2\text{O}$ in 25 ml ethanol), and stirred intensively at room temperature for 12 hr. The milky mixture solution was then ultrasonicated (VCX750 Sonics Materials Inc.) for 30 min to produce a homogeneous suspension prior to the coating onto substrates. Upon drying at room temperature, the treated substrate was further cured at 110°C for 1 hr. For design consideration, breakthrough pressure and solid fraction (f_1) are two determining parameters. The maximum breakthrough pressure ($P_{\text{Breakthrough}}$) can be calculated as the ratio of the unit maximum surface energy to the unit stress area[116]. For triply re-entrant pillar surfaces, the breakthrough pressure can be calculated as[120]:

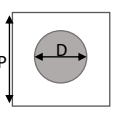

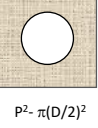
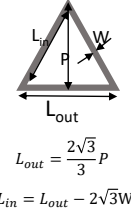


$$P_{\text{Breakthrough-pillars}} = \frac{4\pi D}{4P^2 - \pi D^2} \gamma \quad (5.9)$$

where γ is liquid surface energy, D is the diameter of the re-entrant top and P is the pitch size, as described in the first row of Fig. 45(a). the solid fraction for this geometry is:

$$f_1 = \frac{\pi D^2}{4P^2} \quad (5.10)$$

In our study, similar to *et. al.*[120], we assumed the diameter of re-entrant top, D , is constant as $30\mu\text{m}$. Therefore by changing the pitch, P , the breakthrough pressure and the f_1 can be adjusted, as it is shown in Fig. 45(b) by blue line. For this study pitch size for pillars selected as $P= 80 \mu\text{m}$, similar to above mentioned article. The corresponding values for breakthrough pressure and solid fraction area for this geometry are $P_{Breakthrough-pillars} = 1.2\text{kpa}$, and $f_1 = 0.11$.

(a)

Unit Cell	Circumference	Maximum Surface Energy	Unit Stress Area	Breakthrough Pressure	Solid area fraction (f)
	 $C=\pi D$	$\pi D\gamma$	 $P^2 - \pi(D/2)^2$	$P = \frac{4\pi D}{4P^2 - \pi D^2} \gamma$	$f = \frac{\pi D^2}{4P^2}$
 $L_{out} = \frac{2\sqrt{3}}{3}P$ $L_{in} = L_{out} - 2\sqrt{3}W$	 $C=3(L_{in}+L_{out})$	$3(L_{in}+L_{out})\gamma = \sqrt{3}(4P - W)\gamma$	 $\frac{\sqrt{3}}{4}(L_{out}^2 - L_{in}^2) = \frac{\sqrt{3}}{4}(2PW - 3W^2)$	$P = \frac{4P - W}{2PW - 3W^2} \gamma$	$f = \frac{2PW - 3W^2}{P^2}$

(b)

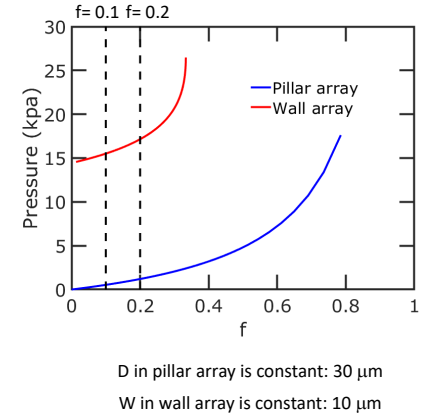


Figure 45 (a) calculation of breakthrough pressure and f value for re-entrant pillar and triangular walls unit cells. Pressure versus f plots for (b) re-entrant pillar and (c) re-entrant triangular walls unit cell.

For wall array, the breakthrough pressure can be calculated as (Fig. 45(a), second row):

$$P_{Breakthrough-walls} = \frac{4P - W}{2PW - 3W^2} \gamma \quad (5.11)$$

where γ is liquid surface energy, W is the width of the re-entrant top and P is the pitch size. The solid fraction also can be calculated as:

$$f_1 = \frac{2PW - 3W^2}{P^2} \quad (5.12)$$

To have the smaller value of f_1 , thinner walls and larger P is required. However, larger P causes lower breakthrough pressure. Therefore values for wall width at the top, W , and the pitch size were intentionally selected to have f_1 between 0.1 to 0.2 and breakthrough pressure larger than 15 kPa. From Fig. 45(b), it can be seen that the breakthrough pressure

range for wall array is larger than pillar array because of the geometry. In this study we selected $W = 10 \mu\text{m}$ and $P = 120 \mu\text{m}$, which correspond to $P_{Breakthrough-walls} = 16.1 \text{ kPa}$, and $f_1 = 0.15$.

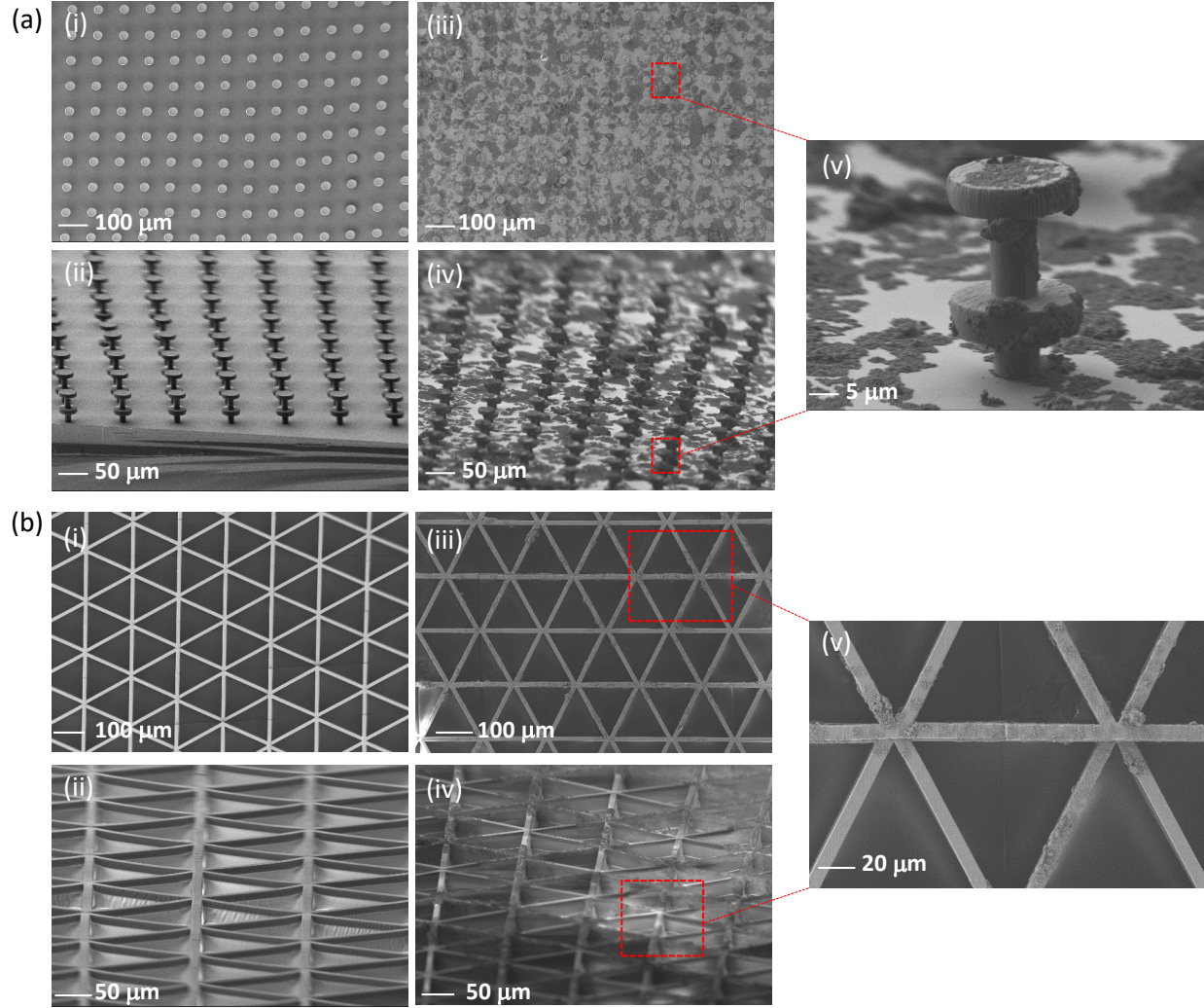


Figure 46 SEM images of 3D printed (a) pillars and (b) walls, before ((i) overhead, (ii) tilted side view) and after ((iii) overhead , (iv) tilted side view) PTFE coating. (v) shows the PTFE nanoparticles on the structures with larger magnification

Fig. 46(a) shows SEM images from (i) top and (ii) side view of the fabricated pillar array, before PTFE coating. The pillar array, before PTFE coating shows high contact angle ($> 150^\circ$) for both water (72.8 mN/m) and EG (47.7 mN/m), however the hysteresis value for those liquids are large, $35.0 \pm 5.5^\circ$ for water and $58.0 \pm 10.0^\circ$ for oil, which means that pillars are cannot be used for self-cleaning and many more applications. However, after PTFE coating, as it is shown in Fig. 46(a) (ii), (iv) and (v), the hysteresis values reduced significantly to $1.5 \pm 0.5^\circ$ for water and $3.0 \pm 1.5^\circ$ for oil. The oleophobic nanoparticles helps the pillar array be more useful for practical application.

Fig. 46(b) shows SEM images of wall array, from (i) top and (ii) side view before PTFE coating. The water contact angle for wall array before coating is $147.0 \pm 2.0^\circ$, with hysteresis of $53.0 \pm 4.5^\circ$. The oil contact angle for wall array before coating is $135.0 \pm 3.5^\circ$, with $85.0 \pm 6.5^\circ$ hysteresis. By PTFE coating, the water and oil contact angle increased to $172.0 \pm 1.5^\circ$ and $161.0 \pm 2.5^\circ$, respectively. The water and hysteresis values reduced to $2.5 \pm 1.5^\circ$, and $4.5 \pm 2.^\circ$, after PTFE coating. Fig. 46(b) (iii) , (v) shows top head SEM images of wall array, and (iv) shows side view of wall array after PTFE coating. By using the PTFE nanoparticles, both high contact angle ($> 150^\circ$) and low hysteresis ($< 10^\circ$) for superomniphobic structures achieved for wall arrays which makes them suitable for several applications.

A Taber Linear Abraser (model 5750) with weighted SCOTCHBRITE abrasive pad was used for abrasion of the samples on a constant surface area of $4 \times 10^{-3} \text{ m}^2$. Fig. 47(a)(i) shows the behavior of water and EG contact angle during repeated abrasion cycles with pressure of 1225 N/m^2 , on wall array, coated with PTFE nanoparticles. After 100 cycles of abrasion, the water contact angle was $152.0 \pm 3.5^\circ$, with hysteresis of $7.1 \pm 2.5^\circ$. The contact angle for EG oil after 100 cycles of abrasion was $145.0 \pm 5.5^\circ$, with hysteresis of $13.0 \pm 6.5^\circ$. We need to mention that abrasion with SCOTCHBRITE abrasive pad simulates very harsh abrasion situation, however even with these condition the wall array remain superhydrophobic and has very high oil contact angle. Fig. 47(a)(ii) shows the SEM image of the abraded sample after 100 cycles. The wall array is still in good shape, however some residue from SCOTCHBRITE abrasive pad left on the microstructures.

In comparison, pillar array almost destroyed after the first cycle (more realistically the first touch of abrasive pad) of abrasion. Fig. 47(b)(i) shows the contact angle changes with the abrasion cycle for pillar array. After the very first run of abrasion, the water contact angle dropped significantly to $91.0 \pm 8.0^\circ$, and hysteresis increased to the maximum value, which mean that the droplets stayed on the structure and cannot be repelled. The oil contact angle also dropped to $74.0 \pm 12.0^\circ$. Fig. 47(b)(ii) shows a SEM image of pillar array after the very first touch of abrasive pad. Majority of the pillars are fallen and destroyed and repellency lost with the first touch. This fact shows that pillar array are not appropriate for real life application, while wall array shows much better mechanical durability.

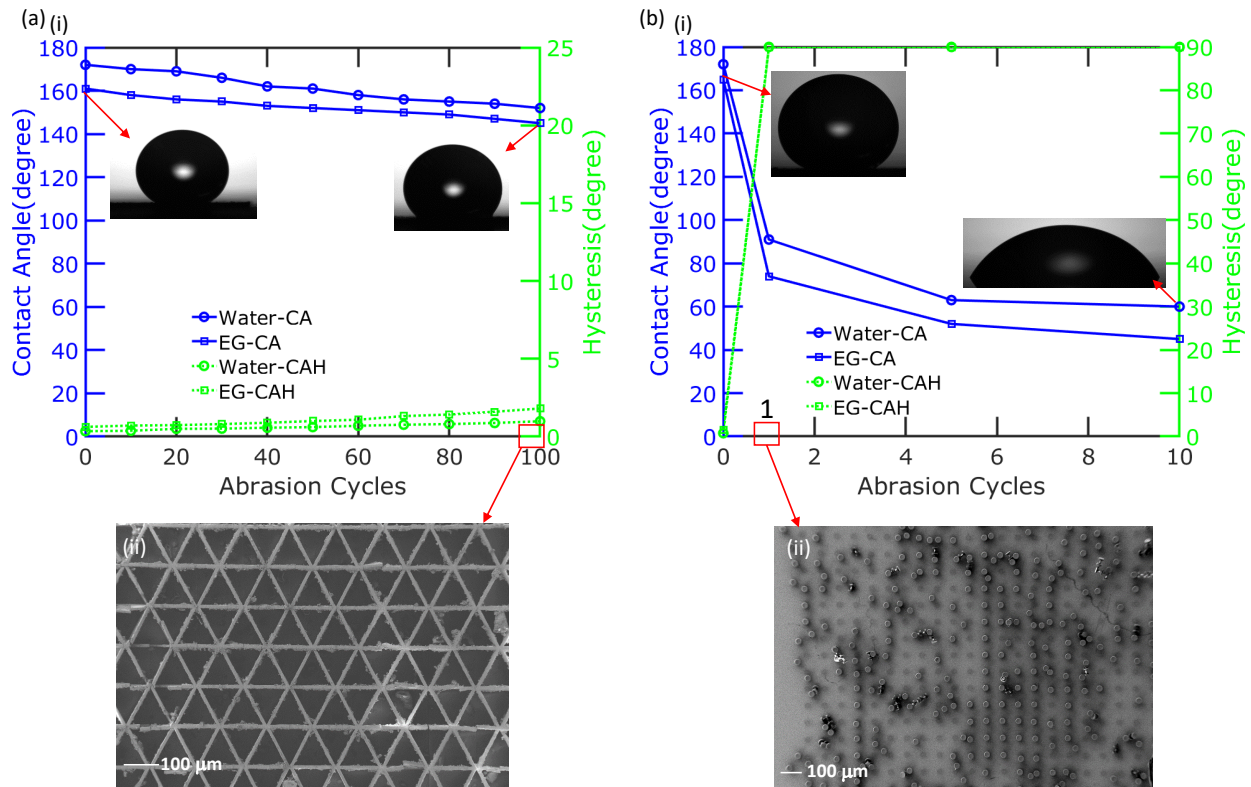


Figure 47 Water and EG contact angle and hysteresis as a function of abrasion for (a)(i) re-entrant walls and (b)(i) re-entrant pillars. (a)(ii) shows SEM images of re-entrant wall after 100 cycles of abrasion. (b)(ii) shows SEM image of re-entrant pillar after just one cycle of abrasion.

5.3.3 Conclusion

In conclusion, we report superomniphobic re-entrant wall array with low hysteresis and high mechanical durability. Re-entrant wall array showed the water and oil contact angle of $172.0 \pm 1.5^\circ$ and $161.0 \pm 2.5^\circ$, respectively, with $2.5 \pm 1.5^\circ$, and $4.5 \pm 2.0^\circ$, hysteresis, after being coated by PTFE nanoparticles. Also the abrasion resistant test demonstrated that the wall array has very good mechanical durability. The water and oil contact angle for wall array after 100 cycle of abrasion by SCOTCHBRITE abrasive pad were $152.0 \pm 3.5^\circ$, $145.0 \pm 5.5^\circ$, respectively, with hysteresis of $7.1 \pm 2.5^\circ$ and $13.0 \pm 6.5^\circ$, respectively. On the other side, re-entrant pillar array, lost their liquid repellency performance after the very first touch of the abrasive pad. The wall array can find very wide application in medical devices, electronic devices. optoelectronics and many more.

6.0 Conclusions and prospects

Micro/nano fabrication offers exciting new possibilities in material design and opportunities for high performance and multi-functional substrates for optoelectronic applications. In this project, I tried to develop new functionalities for regular optical substrates including glass and plastics, by using simulations and experiments.

At the first step, we evaluated the fundamental optical performance for transparent conductor and we showed that there is a reverse relationship between transparency and haze. At the second step, we developed optical substrates with both high transparency and high haze, simultaneously. These functionalities enabled by fabrication of nanoglass structures on glass and plastic substrates. Many optoelectronic applications such as solar cells, backlit liquid crystal displays, and LEDs would benefit from optical substrates with both high transparency and high haze. Substrates with high haze can increase how much light scatters into or out of the underlying photoactive layers and may increase the solar cell power conversion efficiency or LED extraction efficiency, respectively.

At the second phase, we focused on adding self-cleaning and liquid repellency capability to high transparent, high haze optical substrates. We introduced self-cleaning glass with high optical properties and superomniphobic plastic PET, with the ability of liquid repellency for a wide variety of liquids from water (72.8 mN/m) to hexadecane (27.5 mN/m). We demonstrated that adding repellency does not negatively affect the optical properties of these optical substrates. Our Nano Enoki PET substrate exhibit stain-resistance for a variety of liquids including mustard and blood, where the transparency of the original plastic is recovered after staining. Dried mustard and blood both flake off the samples without any residue, indicating no infiltration of the liquid and poor adhesion to the surface.

At the next step, we studied the fabrication of antireflection and liquid repellent for high transparent applications such as displays. We demonstrated a design process that combines Bayesian learning and optimization with the physical intuition of the authors to create a new high-performance, multi-functional glass. The integration of machine learning methods and physical intuition enables us to efficiently search a high-dimensional

fabrication space for creating random re-entrant nanostructures inspired by those on the glasswing butterfly. In particular, we pose a multiobjective optimization problem where we seek to balance the photon management and wettability properties of the surface, and determine a subset of the Pareto efficient frontier that is subject to pre-defined threshold values. We report on a self-healing supertransmissive and superclear nanostructured glass with high liquid repellency and antifogging properties. We envision that these surfaces will be useful in a variety of optical and optoelectronic applications where self-cleaning, anti-fouling, and anti-fogging are important.

Eliminating light reflection from the top glass sheet in optoelectronic applications is often desirable across a broad range of wavelengths and large variety of angles. Next, we report on a combined simulation and experimental study of single layer films, nanowire arrays, and nanocone arrays to meet these antireflection (AR) needs. We demonstrate the application of Bayesian learning to the optimization of these structures for broadband and broad angle AR. We demonstrate that nanocone structures have the best AR performance and additionally provide physical insight into the AR performance of different structures. Simulations suggest nanocone arrays are able to achieve a solar integrated normal and 65° incidence angle reflection of 0.15% and 1.25%, respectively.

Finally, we used novel two-photon polymerization based 3D printing technology to fabricate re-entrant wall structure to address the poor mechanical durability of superomniphobic structures as well as high rolling angle of previously reported 3D printed re-entrant pillars. The abrasion resistant test demonstrated that the wall array has very good mechanical durability. The water and oil contact angle for wall array after 100 cycle of abrasion by SCOTCHBRITE abrasive pad were $152.0 \pm 3.5^\circ$, $145.0 \pm 5.5^\circ$, respectively, with hysteresis of $7.1 \pm 2.5^\circ$ and $13.0 \pm 6.5^\circ$, respectively.

Despite much work has been done so far to improve the performance of optoelectronic substrates, there are still challenges. For example, fabrication of mechanically durable superomniphobic structure on transparent substrate without negative effect on optical properties need to be systematically investigated. Besides, more device-integrated substrates need to be designed and tested, as the sole use of figure of merit for substrate may not adequately reveal how good the surfaces really are.

Appendix

Additional Details For: Discovering Perfect Broadband and Broad Angle Antireflection Surfaces for Optoelectronics by Machine Learning

A.1 Experimental

A.1.1 Fabrication process

Samples were fabricated on 2 cm by 2 cm glass substrates using nanosphere lithography and maskless reactive ion etching (MRIE) techniques. A polystyrene (PS) nanoparticle solution (Sigma-Aldrich) was deposited on glass substrates by dip coating, followed by a plasma etching using reactive ion etching with O_2 at 5 sccm flow rate, for various times based on desired final sphere size. The total pressure of chamber was kept at 150 mTorr and the power was 150 W. Subsequently, dry etching was carried out in a mixture of CF_4 and O_2 gases at 45 and 5 sccm flow rates, respectively, for 10 mins. The power and pressure of the chamber was set on 150 W and 150 mTorr, respectively. Finally, the residuals and the remaining nanoparticles on the surface were removed by O_2 plasma treatment with same chamber power and pressure, for 3 min, followed by ultrasonication in acetone for 5 min. In this method, the distance between pillars can be controlled by size of nanospheres and plasma etching parameters. Figure 48 (a)(i) and (ii) show the SEM images of the fabricated NC array at different magnifications.

Based on Bayesian optimization of numerical simulations, the best optical performance may be achieved by fabricating very close nanocones with pitch size equal to bottom diameter. In order to fabricate these kind of nanostructures, MRIE was used. The process is maskless in that no external mask, such as metal nanoparticles or nanospheres, is used to create the structures. Instead, nanoscale polymer particles randomly deposit on the surface of the substrate during the etching and provide for the etch selectivity needed to

create various high aspect ratio structures. Figure 48 (b)(i) and (ii) shows the SEM image of a fabricated sample by this method. The inter-space of fabricated NCs in this method is very small in the range of 5-50 nm.

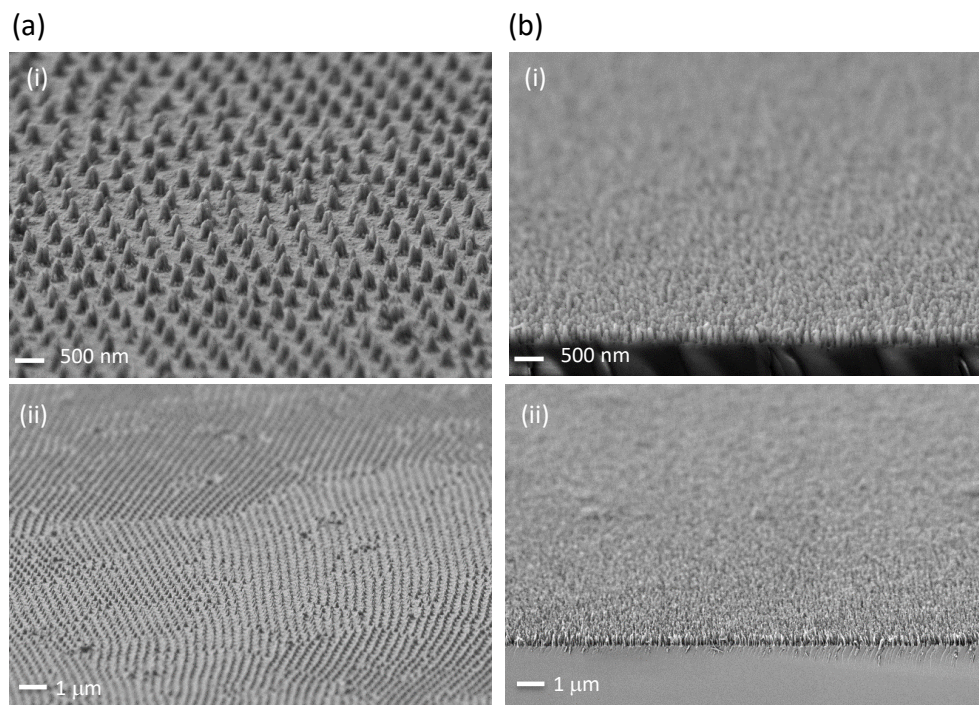


Figure 48 (a) SEM images of NC array fabricated by (a) nanosphere lithography and (b) MRIE. (i) and (ii) shows different magnifications.

The fused silica is etched by CF_4 and O_2 at 45 and 5 sccm flow rates, respectively. The total pressure of chamber was kept at 200 mTorr and the power was 125 W. During the etching process, polymer particles are deposited on the surface of the fused silica substrate, which acts as a micro-mask [145]. The height of the nanostructures can be controlled by varying the etch in time and the etch chemistry can be used to control the degree of vertical versus lateral etching.

A.1.2 Optical characterization

A spectrophotometer (PerkinElmer, Lambda 750) equipped with a 100 mm integrating sphere was used for measuring the total reflection of the sample between 280 and 1200

nm wavelengths. The angle-resolved reflection spectra was measured on an Agilent UV-Vis-NIR Cary-series spectrophotometer system. A large (6) detector aperture was used to ensure all light was collected from the narrow source beam (1 apertures) at high incident angle. At each angle the reflection spectra was collected in a wide band around from 280 to 1200 nm in 1 nm increments and averaged. This process was performed for both TE- and TM-polarizations and averaged for non-normal incident light.

A.1.3 Simulation

The finite difference time domain (FDTD) [213, 177] was used to solve Maxwell's equations and simulate the optical reflection of the different AR structures on glass substrate. Perfectly matched layer (PML) boundary conditions were used for the upper and lower boundary of the simulation cell [8], while periodic boundary conditions with appropriate symmetries were used for the side boundaries to model the interaction between the periodic structure and the polarized incident light. The glass substrate extends past the lower boundary of the simulation cell and thus, only the reflection from the top air/glass interface is measured. Any light going into the substrate is absorbed by the lower PML boundary condition.

A.2 Results and discussion

In this section, we provide additional investigation into the geometry of the nearly efficient outcomes shows predictable behavior in nanostructures which minimize reflection.

A.2.1 NW array

For the NW array, there seems to be a relatively consistent linear relationship between pitch a and diameter d of efficient points (most noticeably in Fig. 49 where the points all roughly fall on a plane); the line of best fit through the nearly efficient points is

$$\text{Diameter} = (0.726)\text{Box Size} + 3.489, \quad R^2 = 0.980.$$

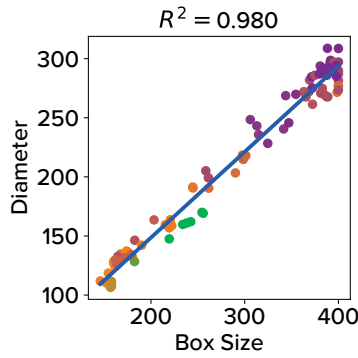


Figure 49 All nearly efficient NW array satisfy a linear relationship between Box Size and Diameter.

A.2.2 NC array

For NC arrays, the optimal or near-optimal cones have a relatively consistent angle, computed with

$$\text{Cone Angle} = \tan^{-1} \left(\frac{(2) \times \text{Height}}{\text{Diameter Bottom} - \text{Diameter Top}} \right).$$

When we fit a line relating the Diameter Bottom to the angle of the nearly Pareto efficient outcomes, we see the fit

$$\text{Cone Angle} = (-5.52 \times 10^{-4})\text{Diameter Bottom} + 1.56,$$

with $R^2 = 0.965$. These angles all fall within 76° to 87° . This result is plotted in Fig. 50. In all cases shown, $d_{bot} \simeq a$.

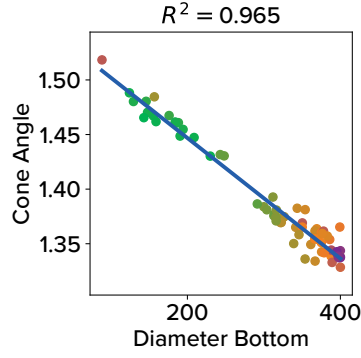


Figure 50 All nearly efficient NC array satisfy a linear relationship between Box Size and Diameter.

A.2.3 Literature data on fabricated NC array

Table 1 Fabricated NC array details in literature.

Fabrication method	R_{0°	R_{65°		Ref
	Wavelength range	Wavelength range	Incidence angle	
Maskless reactive ion etching (MRIE)	280-1200 nm	280-1200 nm	65°	This work
Nanosphere Lithography (NL)	280-1200 nm	280-1200 nm	65°	This work
MRIE+ PECVD	280-1000 nm	550 nm	65°	[67]
Metal dewetting (MD)	390-800 nm	530 nm	65°	[85]
Interference lithography (IL)	300-1300 nm	300-1300 nm	65°	[150]
Soft imprint (SI)	420-1000 nm	532 nm	65°	[185]
Dip-coating and precursor-derived assembly (DC)	400-1200 nm	400-1200 nm	60°	[89]
Ultrasonic-assisted sol-gel (SG)	450-800 nm	450-800 nm	60°	[219]

We compared our fabricated NC array with NC-like structures in the literature (See Tab.S1), fabricated by MRIE followed by plasma enhanced chemical vapor deposition (MRIE+PECVD) [67], metal dewetting (MD) [85], interference lithography (IL) [150], soft imprint (SI)[185], ultrasonic-assisted sol-gel (SG), [219], as well as nanoparticle dip-

coating and precursor-derived one-step assembly (DC) [89]. The wavelength ranges for R_{65° and R_{65° that used in each paper are shown in Table S1. Since some of the reported references do not have the reflection value for 65° incidence angle, we used the closest angle to 65° in order to make a fair comparison. These incident angles are also shown in Table S1. In some references, for example [150], we calculated the reflection from the $R(\lambda) = 100\% - T(\lambda)$, where $T(\lambda)$ is provided in the paper. This assumes absorbance of the glass substrate is 0%.

Bibliography

- [1] Solar spectral irradiance: Air mass 1.5.
- [2] Hugo Águas, Tiago Mateus, António Vicente, Diana Gaspar, Manuel J. Mendes, Wolfgang A. Schmidt, Luís Pereira, Elvira Fortunato, and Rodrigo Martins. Thin Film Silicon Photovoltaic Cells on Paper for Flexible Indoor Applications. *Advanced Functional Materials*, 25(23):3592–3598, 2015.
- [3] Jaeho Ahn, Ji-Won Seo, Tae-Ik Lee, Donguk Kwon, Inkyu Park, Taek-Soo Kim, and Jung-Yong Lee. Extremely Robust and Patternable Electrodes for Copy-Paper-Based Electronics. *ACS Applied Materials & Interfaces*, 8(29):19031–19037, July 2016.
- [4] A. Ahuja, J. A. Taylor, V. Lifton, A. A. Sidorenko, T. R. Salamon, E. J. Lobaton, P. Kolodner, and T. N. Krupenkin. Nanonails: A Simple Geometrical Approach to Electrically Tunable Superlyophobic Surfaces. *Langmuir*, 24(1):9–14, January 2008.
- [5] Amir Asadpoordarvish, Andreas Sandström, Christian Larsen, Roger Bollström, Martti Toivakka, Ronald Österbacka, and Ludvig Edman. Light-Emitting Paper. *Advanced Functional Materials*, 25(21):3238–3245, 2015.
- [6] T. M. Barnes, X. Wu, J. Zhou, A. Duda, J. van de Lagemaat, T. J. Coutts, C. L. Weeks, D. A. Britz, and P. Glatkowski. Single-wall carbon nanotube networks as a transparent back contact in CdTe solar cells. *Applied Physics Letters*, 90(24):243503, 2007.
- [7] W. Barthlott and C. Neinhuis. Purity of the sacred lotus, or escape from contamination in biological surfaces. *Planta*, 202(1):1–8, 1997.
- [8] Jean-Pierre Berenger. A perfectly matched layer for the absorption of electromagnetic waves. *Journal of Computational Physics*, 114(2):185–200, October 1994.
- [9] Stephen M. Bergin, Yu-Hui Chen, Aaron R. Rathmell, Patrick Charbonneau, Zhi-Yuan Li, and Benjamin J. Wiley. The effect of nanowire length and diameter on the properties of transparent, conducting nanowire films. *Nanoscale*, 4(6):1996, 2012.

- [10] Bharat Bhushan, Yong Chae Jung, and Kerstin Koch. Self-Cleaning Efficiency of Artificial Superhydrophobic Surfaces. *Langmuir*, 25(5):3240–3248, March 2009.
- [11] Lisa Brown, Julie M Wolf, Rafael Prados-Rosales, and Arturo Casadevall. Through the wall: extracellular vesicles in gram-positive bacteria, mycobacteria and fungi. *Nature Reviews Microbiology*, 13(10):620, 2015.
- [12] P. D. Burton, A. Hendrickson, S. S. Ulibarri, D. Riley, W. E. Boyson, and B. H. King. Pattern Effects of Soil on Photovoltaic Surfaces. *IEEE Journal of Photovoltaics*, 6(4):976–980, July 2016.
- [13] Linyou Cao, Justin S. White, Joon-Shik Park, Jon A. Schuller, Bruce M. Clemens, and Mark L. Brongersma. Engineering light absorption in semiconductor nanowire devices. *Nat Mater*, 8(8):643–647, 2009.
- [14] C. K. Carniglia. Scalar Scattering Theory for Multilayer Optical Coatings. *OE, OPEGAR*, 18(2):182104, April 1979.
- [15] A. B. D. Cassie and S. Baxter. Wettability of porous surfaces. *Transactions of the Faraday Society*, 40:546, 1944.
- [16] Fevzi Ç. Cebeci, Zhizhong Wu, Lei Zhai, Robert E. Cohen, and Michael F. Rubner. Nanoporosity-Driven Superhydrophilicity: A Means to Create Multifunctional Antifogging Coatings. *Langmuir*, 22(6):2856–2862, March 2006.
- [17] Ying-Chu Chen, Zhe-Sheng Huang, and Hongta Yang. Cicada-Wing-Inspired Self-Cleaning Antireflection Coatings on Polymer Substrates. *ACS Applied Materials & Interfaces*, 7(45):25495–25505, November 2015.
- [18] Dong Yun Choi, Yong Suk Oh, Donggeon Han, Seunghyup Yoo, Hyung Jin Sung, and Sang Soo Kim. Highly conductive, bendable, embedded ag nanoparticle wire arrays via convective self-assembly: Hybridization into ag nanowire transparent conductors. *Advanced Functional Materials*, 25(25):3888–3898, 2015.
- [19] Jaeho Choi, Wonhee Jo, Seung Yeol Lee, Yeon Sik Jung, Shin-Hyun Kim, and Hee-Tak Kim. Flexible and Robust Superomniphobic Surfaces Created by Localized Photofluidization of Azopolymer Pillars. *ACS Nano*, 11(8):7821–7828, August 2017.

- [20] Wonjae Choi, Anish Tuteja, Shreerang Chhatre, Joseph M. Mabry, Robert E. Cohen, and Gareth H. McKinley. Fabrics with Tunable Oleophobicity. *Advanced Materials*, 21(21):2190–2195, June 2009.
- [21] Hung-Tao Chou, Ying-Chieh Chen, Chi-Young Lee, Hwan-You Chang, and Nyan-Hwa Tai. Switchable transparency of dual-controlled smart glass prepared with hydrogel-containing graphene oxide for energy efficiency. *Solar Energy Materials and Solar Cells*, 166:45–51, July 2017.
- [22] Wei-Ping Chu, Jian-Shian Lin, Tien-Chai Lin, Yu-Sheng Tsai, Chen-Wei Kuo, Ming-Hua Chung, Tsung-Eong Hsieh, Lung-Chang Liu, Fuh-Shyang Juang, and Nien-Po Chen. Using high haze (>90%) light-trapping film to enhance the efficiency of a-Si:H solar cells. *Optics Communications*, 285(15):3325–3328, July 2012.
- [23] Zonglin Chu and Stefan Seeger. Superamphiphobic surfaces. *Chemical Society Reviews*, 43(8):2784–2798, March 2014.
- [24] Fan Cui, Yi Yu, Letian Dou, Jianwei Sun, Qin Yang, Christian Schildknecht, Kerstin Schierle-Arndt, and Peidong Yang. Synthesis of ultrathin copper nanowires using tris(trimethylsilyl)silane for high-performance and low-haze transparent conductors. *Nano Letters*, 15(11):7610–7615, 2015. PMID: 26496181.
- [25] Daniela Cupelli, Fiore Pasquale Nicoletta, Sabrina Manfredi, Giovanni De Filpo, and Giuseppe Chidichimo. Electrically switchable chromogenic materials for external glazing. *Solar Energy Materials and Solar Cells*, 93(3):329–333, March 2009.
- [26] ASTM D1003-13. Standard test method for haze and luminous transmittance of transparent plastics. *ASTM International*.
- [27] Sukanta De, Thomas M. Higgins, Philip E. Lyons, Evelyn M. Doherty, Peter N. Nirmalraj, Werner J. Blau, John J. Boland, and Jonathan N. Coleman. Silver nanowire networks as flexible, transparent, conducting films: Extremely high DC to optical conductivity ratios. *ACS Nano*, 3(7):1767–1774, July 2009.
- [28] Letian Dou, Fan Cui, Yi Yu, Garo Khanarian, Samuel W. Eaton, Qin Yang, Joaquin Resasco, Christian Schildknecht, Kerstin Schierle-Arndt, and Peidong Yang. Solution-processed copper/reduced-graphene-oxide core/shell nanowire transparent conductors. *ACS Nano*, 0(0):null, 2016. PMID: 26820809.

- [29] Jaroslaw Drelich and Emil Chibowski. Superhydrophilic and Superwetting Surfaces: Definition and Mechanisms of Control. *Langmuir*, 26(24):18621–18623, December 2010.
- [30] Daniel Ebert and Bharat Bhushan. Transparent, Superhydrophobic, and Wear-Resistant Coatings on Glass and Polymer Substrates Using SiO₂, ZnO, and ITO Nanoparticles. *Langmuir*, 28(31):11391–11399, August 2012.
- [31] Matthias Ehrgott. *Multicriteria optimization*, volume 491. Springer Science & Business Media, 2005.
- [32] Zhiqiang Fang, Hongli Zhu, Wenzhong Bao, Colin Preston, Zhen Liu, Jiaqi Dai, Yuanyuan Li, and Liangbing Hu. Highly transparent paper with tunable haze for green electronics. *Energy & Environmental Science*, 7(10):3313–3319, 2014.
- [33] Zhiqiang Fang, Hongli Zhu, Colin Preston, Xiaogang Han, Yuanyuan Li, Seongwoo Lee, Xinsheng Chai, Gang Chen, and Liangbing Hu. Highly transparent and writable wood all-cellulose hybrid nanostructured paper. *Journal of Materials Chemistry C*, 1(39):6191–6197, September 2013.
- [34] Zhiqiang Fang, Hongli Zhu, Yongbo Yuan, Dongheon Ha, Shuze Zhu, Colin Preston, Qingxia Chen, Yuanyuan Li, Xiaogang Han, Seongwoo Lee, Gang Chen, Teng Li, Jeremy Munday, Jinsong Huang, and Liangbing Hu. Novel Nanostructured Paper with Ultrahigh Transparency and Ultrahigh Haze for Solar Cells. *Nano Lett.*, 14(2):765–773, February 2014.
- [35] Gregory E. Fasshauer and Michael J. McCourt. *Kernel-based Approximation Methods Using Matlab*. World Scientific, 2015.
- [36] Jin-Xian Feng, Qi Li, Xue-Feng Lu, Ye-Xiang Tong, and Gao-Ren Li. Flexible symmetrical planar supercapacitors based on multi-layered MnO₂/Ni/graphite/paper electrodes with high-efficient electrochemical energy storage. *Journal of Materials Chemistry A*, 2(9):2985–2992, February 2014.
- [37] Jin-Xian Feng, Sheng-Hua Ye, Xue-Feng Lu, Ye-Xiang Tong, and Gao-Ren Li. Asymmetric Paper Supercapacitor Based on Amorphous Porous Mn₃O₄ Negative Electrode and Ni(OH)₂ Positive Electrode: A Novel and High-Performance Flexible Electrochemical Energy Storage Device. *ACS Applied Materials & Interfaces*, 7(21):11444–11451, June 2015.

- [38] Susana C. M. Fernandes, Lúcia Oliveira, Carmen S. R. Freire, Armando J. D. Silvestre, Carlos Pascoal Neto, Alessandro Gandini, and Jacques Desbrières. Novel transparent nanocomposite films based on chitosan and bacterial cellulose. *Green Chemistry*, 11(12):2023–2029, December 2009.
- [39] P. I. Frazier. A Tutorial on Bayesian Optimization. *ArXiv e-prints*, July 2018.
- [40] Peter I. Frazier. Bayesian optimization. In Esma Gel and Lewis Ntamo, editors, *Recent Advances in Optimization and Modeling of Contemporary Problems*, pages 255–278. INFORMS, 2018.
- [41] Hayaka Fukuzumi, Tsuguyuki Saito, Tadahisa Iwata, Yoshiaki Kumamoto, and Akira Isogai. Transparent and High Gas Barrier Films of Cellulose Nanofibers Prepared by TEMPO-Mediated Oxidation. *Biomacromolecules*, 10(1):162–165, January 2009.
- [42] Reiner Fürstner, Wilhelm Barthlott, Christoph Neinhuis, and Peter Walzel. Wet-ting and self-cleaning properties of artificial superhydrophobic surfaces. *Langmuir*, 21(3):956–961, February 2005.
- [43] Kezheng Gao, Ziqiang Shao, Xue Wu, Xi Wang, Jia Li, Yunhua Zhang, Wenjun Wang, and Feijun Wang. Cellulose nanofibers/reduced graphene oxide flexible transparent conductive paper. *Carbohydrate Polymers*, 97(1):243–251, August 2013.
- [44] Tongchuan Gao, Sajad Haghanifar, Maxwell G. Lindsay, Ping Lu, Md Imrul Kayes, Bradley D. Pafchek, Ziyu Zhou, Paul R. Ohodnicki, and Paul W. Leu. Fundamental performance limits and haze evaluation of metal nanomesh transparent conductors. *Advanced Optical Materials*, 6(9):1700829, 2018.
- [45] Tongchuan Gao, Po-Shun Huang, Jung kun Lee, and Paul W. Leu. Hierarchical metal nanomesh/microgrid structures for ordered and uniform transparent electrodes. *RSC Advances*, 5(87):70713–70717, Aug 2015.
- [46] Tongchuan Gao and Paul W. Leu. Copper nanowire arrays for transparent electrodes. *Journal of Applied Physics*, 114(6):063107–063107–6, August 2013.
- [47] Tongchuan Gao and Paul W. Leu. The role of propagating modes in silver nanowire arrays for transparent electrodes. *Optics Express*, 21(S3):A419, April 2013.

- [48] Tongchuan Gao, Zhiting Li, Po-shun Huang, Ganesh J Shenoy, David Parobek, Susheng Tan, Jung-kun Lee, Haitao Liu, and Paul W Leu. Hierarchical graphene/metal grid structures for stable, flexible transparent conductors. *Acc Nano*, 9(5):5440–5446, 2015.
- [49] Tongchuan Gao, Baomin Wang, Bo Ding, Jung-kun Lee, and Paul W Leu. Uniform and ordered copper nanomeshes by microsphere lithography for transparent electrodes. *Nano letters*, 14(4):2105–2110, 2014.
- [50] Sean M. Garner. *Flexible Glass: Enabling Thin, Lightweight, and Flexible Electronics*. John Wiley & Sons, August 2017. Google-Books-ID: HkkzDwAAQBAJ.
- [51] Michael Adam Gelbart. *Constrained Bayesian optimization and applications*. PhD thesis, Harvard University, 2015.
- [52] Gerwin H. Gelinck, H. Edzer A. Huitema, Erik van Veenendaal, Eugenio Cantatore, Laurens Schrijnemakers, Jan B. P. H. van der Putten, Tom C. T. Geuns, Monique Beenhakkers, Jacobus B. Giesbers, Bart-Hendrik Huisman, Eduard J. Meijer, Estrella Mena Benito, Fred J. Touwslager, Albert W. Marsman, Bas J. E. van Rens, and Dago M. de Leeuw. Flexible active-matrix displays and shift registers based on solution-processed organic transistors. *Nature Materials*, 3(2):106, February 2004.
- [53] David Ginsbourger, Rodolphe Le Riche, and Laurent Carraro. A Multi-points Criterion for Deterministic Parallel Global Optimization based on Gaussian Processes. Technical report, Ecole Nationale Supérieure des Mines, March 2008.
- [54] Stefan Glatzel, Zoë Schnepf, and Cristina Giordano. From Paper to Structured Carbon Electrodes by Inkjet Printing. *Angewandte Chemie International Edition*, 52(8):2355–2358, 2013.
- [55] Kevin Golovin, Duck H. Lee, Joseph M. Mabry, and Anish Tuteja. Transparent, Flexible, Superomniphobic Surfaces with Ultra-Low Contact Angle Hysteresis. *Angewandte Chemie International Edition*, 52(49):13007–13011, December 2013.
- [56] Eliot F. Gomez and Andrew J. Steckl. Improved Performance of OLEDs on Cellulose/Epoxy Substrate Using Adenine as a Hole Injection Layer. *ACS Photonics*, 2(3):439–445, March 2015.
- [57] Xiuqing Gong, Jiaying Li, Shuyu Chen, and Weijia Wen. Copolymer solution-based “smart window”. *Appl. Phys. Lett.*, 95(25):251907, December 2009.

- [58] Dirk Goossens and Emmanuel Van Kerschaever. Aeolian dust deposition on photovoltaic solar cells: the effects of wind velocity and airborne dust concentration on cell performance. *Solar Energy*, 66(4):277–289, July 1999.
- [59] Paula Gould. Smart, clean surfaces. *Materials Today*, 6(11):44–48, November 2003.
- [60] D. Ha, J. Murray, Z. Fang, L. Hu, and J. N. Munday. Advanced Broadband Antireflection Coatings Based on Cellulose Microfiber Paper. *IEEE Journal of Photovoltaics*, 5(2):577–583, March 2015.
- [61] Dongheon Ha, Zhiqiang Fang, Liangbing Hu, and Jeremy N. Munday. Paper-Based Anti-Reflection Coatings for Photovoltaics. *Advanced Energy Materials*, 4(9):1301804, 2014.
- [62] Dongheon Ha, Zhiqiang Fang, and Nikolai B. Zhitenev. Paper in Electronic and Optoelectronic Devices. *Advanced Electronic Materials*, 4(5):1700593, 2018.
- [63] Sajad Haghanifar, Anthony J Galante, Jun Chen, and Paul W. Leu. 3d printed superomniphobic condensation resistant structures with ultra-low hysteresis, and high abrasion resistance. 2020. (submitted to ACS Nano).
- [64] Sajad Haghanifar, Tongchuan Gao, Rafael T. Rodriguez De Vecchis, Bradley Pafchek, Tevis D. B. Jacobs, and Paul W. Leu. Ultrahigh-transparency, ultrahigh-haze nanograss glass with fluid-induced switchable haze. *Optica*, 4(12):1522–1525, December 2017.
- [65] Sajad Haghanifar, Ping Lu, Md Imrul Kayes, Susheng Tan, Ki-Joong Kim, Tongchuan Gao, Paul Ohodnicki, and Paul W. Leu. Self-cleaning, high transmission, near unity haze OTS/silica nanostructured glass. *Journal of Materials Chemistry C*, 6(34):9191–9199, 2018.
- [66] Sajad Haghanifar, Michael McCourt, Bolong Cheng, Jeffrey Wuenschell, Paul Ohodnicki, and Paul W. Leu. Discovering near-perfect broadband and broad angle antireflection surfaces for solar energy conversion by machine learning. 2019. (submitted to Optica).
- [67] Sajad Haghanifar, Michael McCourt, Bolong Cheng, Jeffrey Wuenschell, Paul Ohodnicki, and Paul W. Leu. Creating glasswing butterfly-inspired durable antifog-

- ging superomniphobic supertransmissive, superclear nanostructured glass through Bayesian learning and optimization. *Materials Horizons*, 6(8):1632–1642, 2019.
- [68] Sajad Haghanifar, Luke M. Tomasovic, Anthony J. Galante, David Pekker, and Paul W. Leu. Stain-resistant, superomniphobic flexible optical plastics based on nano-enoki mushroom-like structures. *Journal of Materials Chemistry A*, 7(26):15698–15706, 2019.
 - [69] Sajad Haghanifar, Rafael T. Rodriguez De Vecchis, Ki-Joong Kim, Jeffrey Wuen-schell, Sooraj P. Sharma, Ping Lu, Paul Ohodnicki, and Paul W. Leu. Flexible nanograss with highest combination of transparency and haze for optoelectronic plastic substrates. *Nanotechnology*, 29(42):42LT01, 2018.
 - [70] Guifang Han, Sam Zhang, Pablo P. Boix, Lydia Helena Wong, Lidong Sun, and Shui-Yang Lien. Towards high efficiency thin film solar cells. *Progress in Materials Science*, 87:246–291, June 2017.
 - [71] Tae-Hee Han, Youngbin Lee, Mi-Ri Choi, Seong-Hoon Woo, Sang-Hoon Bae, Byung Hee Hong, Jong-Hyun Ahn, and Tae-Woo Lee. Extremely efficient flexible organic light-emitting diodes with modified graphene anode. *Nature Photonics*, 6(2):105–110, February 2012.
 - [72] Z. W. Han, Z. Wang, X. M. Feng, B. Li, Z. Z. Mu, J. Q. Zhang, S. C. Niu, and L. Q. Ren. Antireflective surface inspired from biology: A review. *Biosurface and Biotribology*, 2(4):137–150, December 2016.
 - [73] Zhiwu Han, Zhibin Jiao, Shichao Niu, and Luquan Ren. Ascendant bioinspired antireflective materials: Opportunities and challenges coexist. *Progress in Materials Science*, 103:1–68, June 2019.
 - [74] Nikolaus Hansen, Sibylle D Müller, and Petros Koumoutsakos. Reducing the time complexity of the derandomized evolution strategy with covariance matrix adaptation (cma-es). *Evolutionary computation*, 11(1):1–18, 2003.
 - [75] Shuijian He, Chunxiang Hu, Haoqing Hou, and Wei Chen. Ultrathin MnO₂ nanosheets supported on cellulose based carbon papers for high-power supercapacitors. *Journal of Power Sources*, 246:754–761, January 2014.

- [76] David S. Hecht, Liangbing Hu, and Glen Irvin. Emerging transparent electrodes based on thin films of carbon nanotubes, graphene, and metallic nanostructures. *Advanced Materials*, 23(13):1482–1513, 2011.
- [77] David S. Hecht, David Thomas, Liangbing Hu, Corinne Ladous, Tom Lam, Youngbae Park, Glen Irvin, and Paul Drzaic. Carbon-nanotube film on plastic as transparent electrode for resistive touch screens. *Journal of the Society for Information Display*, 17(11):941–946, 2009.
- [78] Ming-Chun Hsieh, Changjae Kim, Masaya Nogi, and Katsuaki Suganuma. Electrically conductive lines on cellulose nanopaper for flexible electrical devices. *Nanoscale*, 5(19):9289–9295, September 2013.
- [79] Po-Chun Hsu, Shuang Wang, Hui Wu, Vijay K. Narasimhan, Desheng Kong, Hye Ryoung Lee, and Yi Cui. Performance enhancement of metal nanowire transparent conducting electrodes by mesoscale metal wires. *Nature Communications*, 4(1):1–7, September 2013.
- [80] Liangbing Hu, Guangyuan Zheng, Jie Yao, Nian Liu, Ben Weil, Martin Eskilsson, Erdem Karabulut, Zhichao Ruan, Shanhui Fan, Jason T. Bloking, Michael D. McGehee, Lars Wågberg, and Yi Cui. Transparent and conductive paper from nanocellulose fibers. *Energy & Environmental Science*, 6(2):513–518, July 2013.
- [81] Songtao Hu, Xiaobao Cao, Tom Reddyhoff, Debashis Puhon, Sorin-Cristian Vladescu, Qian Wang, Xi Shi, Zhike Peng, Andrew J. deMello, and Daniele Dini. Self-Compensating Liquid-Repellent Surfaces with Stratified Morphology. *ACS Applied Materials & Interfaces*, 12(3):4174–4182, January 2020. Publisher: American Chemical Society.
- [82] Arved Hübner, Bystrík Trnovec, Tino Zillger, Moazzam Ali, Nora Wetzold, Markus Mingebach, Alexander Wagenpfahl, Carsten Deibel, and Vladimir Dyakonov. Printed Paper Photovoltaic Cells. *Advanced Energy Materials*, 1(6):1018–1022, 2011.
- [83] C.L. Hwang and A.S.M. Masud. *Multiple objective decision making, methods and applications: a state-of-the-art survey*. Lecture notes in economics and mathematical systems. Springer-Verlag, 1979.
- [84] Yunhyeok Im, Yogendra Joshi, Carter Dietz, and Seung S. Lee. Enhanced boiling of a dielectric liquid on copper nanowire surfaces. *Int. J. Micro-Nano Scale Transp.*, 1(1):79–95, 2010.

- [85] Daniel Infante, Karl W. Koch, Prantik Mazumder, Lili Tian, Albert Carrilero, Domenico Tulli, David Baker, and Valerio Pruneri. Durable, superhydrophobic, antireflection, and low haze glass surfaces using scalable metal dewetting nanostructuring. *Nano Research*, 6(6):429–440, June 2013.
- [86] Elena P Ivanova, Jafar Hasan, Hayden K Webb, Vi Khanh Truong, Gregory S Watson, Jolanta A Watson, Vladimir A Baulin, Sergey Pogodin, James Y Wang, Mark J Tobin, et al. Natural bactericidal surfaces: mechanical rupture of pseudomonas aeruginosa cells by cicada wings. *Small*, 8(16):2489–2494, 2012.
- [87] S. Iwamoto, A.N. Nakagaito, and H. Yano. Nano-fibrillation of pulp fibers for the processing of transparent nanocomposites. *Applied Physics A*, 89(2):461–466, November 2007.
- [88] Eunwook Jeong, Guoqing Zhao, Myungkwan Song, Seung Min Yu, Jongjoo Rha, Jongmoon Shin, Young-Rae Cho, and Jungheum Yun. Simultaneous improvements in self-cleaning and light-trapping abilities of polymer substrates for flexible organic solar cells. *Journal of Materials Chemistry A*, 6(5):2379–2387, 2018.
- [89] Binbin Jin and Junhui He. Self-Templated Fabrication of Robust Moth-Eye-Like Nanostructures with Broadband and Quasi-Omnidirectional Antireflection Properties. *ACS Photonics*, 4(1):188–196, January 2017.
- [90] Mi-Hee Jung and Ho-Suk Choi. Characterization of octadecyltrichlorosilane self-assembled monolayers on silicon (100) surface. *Korean Journal of Chemical Engineering*, 26(6):1778–1784, November 2009.
- [91] Yong Chae Jung and Bharat Bhushan. Wetting transition of water droplets on superhydrophobic patterned surfaces. *Scripta Materialia*, 57(12):1057–1060, December 2007.
- [92] Malgorzata Jurak and Emil Chibowski. Wettability and Topography of Phospholipid DPPC Multilayers Deposited by Spin-Coating on Glass, Silicon, and Mica Slides. *Langmuir*, 23(20):10156–10163, September 2007.
- [93] Gumin Kang, Kyuyoung Bae, Minwoo Nam, Doo-Hyun Ko, Kyoungsik Kim, and Willie J. Padilla. Broadband and ultrahigh optical haze thin films with self-aggregated alumina nanowire bundles for photovoltaic applications. *Energy & Environmental Science*, 8(9):2650–2656, August 2015.

- [94] Sung H. Kang, Boaz Pokroy, L. Mahadevan, and Joanna Aizenberg. Control of Shape and Size of Nanopillar Assembly by Adhesion-Mediated Elastocapillary Interaction. *ACS Nano*, 4(11):6323–6331, November 2010.
- [95] Ladislav Kavan, Paul Liska, Shaik M. Zakeeruddin, and Michael Grätzel. Low-temperature fabrication of highly-efficient, optically-transparent (fto-free) graphene cathode for co-mediated dye-sensitized solar cells with acetonitrile-free electrolyte solution. *Electrochimica Acta*, 195:34 – 42, 2016.
- [96] Md Imrul Kayes, Anthony J. Galante, Nicholas A. Stella, Sajad Haghanifar, Robert M. Q. Shanks, and Paul W. Leu. Stable lotus leaf-inspired hierarchical, fluorinated polypropylene surfaces for reduced bacterial adhesion. *Reactive and Functional Polymers*, 128:40–46, July 2018.
- [97] Eunhye Kim, Hyunsu Cho, Kyoo Hyun Kim, Tae-Wook Koh, Jin Chung, Jonghee Lee, YongKeun Park, and Seunghyup Yoo. A Facile Route to Efficient, Low-Cost Flexible Organic Light-Emitting Diodes: Utilizing the High Refractive Index and Built-In Scattering Properties of Industrial-Grade PEN Substrates. *Adv. Mater.*, 27(9):1624–1631, March 2015.
- [98] Tae-Soo Kim, Seok-In Na, Seok-Soon Kim, Byung-Kwan Yu, Jun-Suk Yeo, and Dong-Yu Kim. Solution-processible polymer solar cells fabricated on a papery substrate. *physica status solidi (RRL) – Rapid Research Letters*, 6(1):13–15, 2012.
- [99] Yura Kim, Dayeon Jung, Seyoon Jeong, Kwangyoon Kim, Woosuk Choi, and Yongho Seo. Optical properties and optimized conditions for polymer dispersed liquid crystal containing UV curable polymer and nematic liquid crystal. *Current Applied Physics*, 15(3):292–297, March 2015.
- [100] Hirotaka Koga, Masaya Nogi, Natsuki Komoda, Thi Thi Nge, Tohru Sugahara, and Katsuaki Suganuma. Uniformly connected conductive networks on cellulose nanofiber paper for transparent paper electronics. *NPG Asia Mater*, 6:e93–, 03 2014.
- [101] Hirotaka Koga, Tsuguyuki Saito, Takuya Kitaoka, Masaya Nogi, Katsuaki Suganuma, and Akira Isogai. Transparent, Conductive, and Printable Composites Consisting of TEMPO-Oxidized Nanocellulose and Carbon Nanotube. *Biomacromolecules*, 14(4):1160–1165, April 2013.

- [102] Tae-Wook Koh, Joshua A. Spechler, Kyung Min Lee, Craig B. Arnold, and Barry P. Rand. Enhanced Outcoupling in Organic Light-Emitting Diodes via a High-Index Contrast Scattering Layer. *ACS Photonics*, 2(9):1366–1372, September 2015.
- [103] Arun K. Kota, Yongxin Li, Joseph M. Mabry, and Anish Tuteja. Hierarchically Structured Superoleophobic Surfaces with Ultralow Contact Angle Hysteresis. *Advanced Materials*, 24(43):5838–5843, 2012.
- [104] Hemant Kumar Raut, V. Anand Ganesh, A. Sreekumaran Nair, and Seeram Ramakrishna. Anti-reflective coatings: A critical, in-depth review. *Energy & Environmental Science*, 4(10):3779–3804, 2011.
- [105] B. Lamprecht, R. Thünauer, M. Ostermann, G. Jakopic, and G. Leising. Organic photodiodes on newspaper. *physica status solidi (a)*, 202(5):R50–R52, 2005.
- [106] Phillip Lee, Jooyeun Ham, Jinhwan Lee, Sukjoon Hong, Seungyong Han, Young Duk Suh, Sang Eon Lee, Junyeob Yeo, Seung Seob Lee, Dongjin Lee, and Seung Hwan Ko. Highly stretchable or transparent conductor fabrication by a hierarchical multiscale hybrid nanocomposite. *Advanced Functional Materials*, 24(36):5671–5678, 2014.
- [107] Youngwoo Lee, Won-Yong Jin, Kuk Young Cho, Jae-Wook Kang, and Jihoon Kim. Thermal pressing of a metal-grid transparent electrode into a plastic substrate for flexible electronic devices. *Journal of Materials Chemistry C*, 4(32):7577–7583, 2016.
- [108] C. Legnani, C. Vilani, V. L. Calil, H. S. Barud, W. G. Quirino, C. A. Achete, S. J. L. Ribeiro, and M. Cremona. Bacterial cellulose membrane as flexible substrate for organic light emitting devices. *Thin Solid Films*, 517(3):1016–1020, December 2008.
- [109] Boxun Leng, Zhengzhong Shao, Gijsbertus de With, and Weihua Ming. Superoleophobic Cotton Textiles. *Langmuir*, 25(4):2456–2460, February 2009.
- [110] Lucia Leonat, Matthew Schuette White, Eric Daniel Glowacki, Markus Clark Scharber, Tino Zillger, Julia Rühling, Arved Hübner, and Niyazi Serdar Sariciftci. 4% Efficient Polymer Solar Cells on Paper Substrates. *The Journal of Physical Chemistry C*, 118(30):16813–16817, July 2014.

- [111] Shaohui Li, Dekang Huang, Bingyan Zhang, Xiaobao Xu, Mingkui Wang, Guang Yang, and Yan Shen. Flexible Supercapacitors Based on Bacterial Cellulose Paper Electrodes. *Advanced Energy Materials*, 4(10):1301655, 2014.
- [112] Lu Lian, Dan Dong, Shuai Yang, Bingwu Wei, and Gufeng He. Highly conductive and uniform alginate/silver nanowire composite transparent electrode by room temperature solution processing for organic light emitting diode. *ACS Applied Materials & Interfaces*, 9(13):11811–11818, 2017. PMID: 28290197.
- [113] David R Lida. CRC Handbook of Chemistry and Physics, 88th Edition, June 2007.
- [114] Xing Yi Ling, In Yee Phang, G. Julius Vancso, Jurriaan Huskens, and David N. Reinhoudt. Stable and Transparent Superhydrophobic Nanoparticle Films. *Langmuir*, 25(5):3260–3263, March 2009.
- [115] Shilin Liu and Lina Zhang. Effects of polymer concentration and coagulation temperature on the properties of regenerated cellulose films prepared from LiOH/urea solution. *Cellulose*, 16(2):189–198, April 2009.
- [116] Tingyi “Leo” Liu and Chang-Jin “CJ” Kim. Turning a surface superrepellent even to completely wetting liquids. *Science*, 346(6213):1096–1100, November 2014.
- [117] Xiao Liu, Ying Xiong, Jiabin Shen, and Shaoyun Guo. Fast fabrication of a novel transparent PMMA light scattering materials with high haze by doping with ordinary polymer. *Optics Express*, 23(14):17793–17804, July 2015.
- [118] Xiao Liu, Ziru Zhao, Ying Xiong, Ping Yi, and Shaoyun Guo. Cost-effective way to improve the optical properties of poly(methyl methacrylate)/poly(ethylene terephthalate) light scattering materials: drop coalescence. *Applied Optics*, 57(9):2107–2114, March 2018.
- [119] Xiaojiang Liu, Hongcheng Gu, Haibo Ding, Xin Du, Zhenzhu He, Liangdong Sun, Junlong Liao, Pengfeng Xiao, and Zhongze Gu. Programmable Liquid Adhesion on Bio-Inspired Re-Entrant Structures. *Small*, 15(35):1902360, 2019. _eprint: <https://onlinelibrary.wiley.com/doi/pdf/10.1002/sml.201902360>.
- [120] Xiaojiang Liu, Hongcheng Gu, Min Wang, Xin Du, Bingbing Gao, Abdelrahman Elbaz, Liangdong Sun, Julong Liao, Pengfeng Xiao, and Zhongze Gu. 3d Printing of Bioinspired Liquid Superrepellent Structures. *Advanced Materials*, 30(22):1800103, March 2018.

- [121] J. Lomga, P. Varshney, D. Nanda, M. Satapathy, S. S. Mohapatra, and A. Kumar. Fabrication of durable and regenerable superhydrophobic coatings with excellent self-cleaning and anti-fogging properties for aluminium surfaces. *Journal of Alloys and Compounds*, 702:161–170, April 2017.
- [122] Crystal Shaojuan Luo, Pengbo Wan, Hui Yang, Sayyed Asim Ali Shah, and Xiaodong Chen. Healable transparent electronic devices. *Advanced Functional Materials*, 2017.
- [123] Shaoyi Lyu, Huanjun Chang, Feng Fu, La Hu, Jingda Huang, and Siqun Wang. Cellulose-coupled graphene/polypyrrole composite electrodes containing conducting networks built by carbon fibers as wearable supercapacitors with excellent foldability and tailorability. *Journal of Power Sources*, 327:438–446, September 2016.
- [124] W. A. MacDonald, M. K. Looney, D. MacKerron, R. Eveson, R. Adam, K. Hashimoto, and K. Rakos. Latest advances in substrates for flexible electronics. *Journal of the Society for Information Display*, 15(12):1075–1083, 2007.
- [125] Satish A. Mahadik, Mahendra S. Kavale, S. K. Mukherjee, and A. Venkateswara Rao. Transparent Superhydrophobic silica coatings on glass by sol–gel method. *Applied Surface Science*, 257(2):333–339, November 2010.
- [126] Abraham Marmur. From Hygrophilic to Superhydrophobic: Theoretical Conditions for Making High-Contact-Angle Surfaces from Low-Contact-Angle Materials, June 2008.
- [127] Prantik Mazumder, Yongdong Jiang, David Baker, Albert Carrilero, Domenico Tulli, Daniel Infante, Andrew T. Hunt, and Valerio Pruneri. Superomniphobic, Transparent, and Antireflection Surfaces Based on Hierarchical Nanostructures. *Nano Letters*, 14(8):4677–4681, August 2014.
- [128] Aaron D. Mazzeo, William B. Kalb, Lawrence Chan, Matthew G. Killian, Jean-Francis Bloch, Brian A. Mazzeo, and George M. Whitesides. Paper-Based, Capacitive Touch Pads. *Advanced Materials*, 24(21):2850–2856, 2012.
- [129] Adam J. Meuler, Gareth H. McKinley, and Robert E. Cohen. Exploiting Topographical Texture To Impart Icephobicity. *ACS Nano*, 4(12):7048–7052, December 2010.

- [130] Sang-Hong Min, Chang Kyo Kim, Ho-Nyeon Lee, and Dae-Gyu Moon. An OLED Using Cellulose Paper as a Flexible Substrate. *Molecular Crystals and Liquid Crystals*, 563(1):159–165, September 2012.
- [131] Seong Min Kang, Sang Moon Kim, Hong Nam Kim, Moon Kyu Kwak, Dong Ha Tahk, and Kahp Y. Suh. Robust superomniphobic surfaces with mushroom-like micropillar arrays. *Soft Matter*, 8(33):8563–8568, 2012.
- [132] Melinda Mohl, Aron Dombovari, Robert Vajtai, Pulickel M. Ajayan, and Krisztian Kordas. Self-assembled large scale metal alloy grid patterns as flexible transparent conductive layers. *Scientific Reports*, 5:13710 EP –, 09 2015.
- [133] Timothée Mouterde, Gaëlle Lehoucq, Stéphane Xavier, Antonio Checco, Charles T. Black, Atikur Rahman, Thierry Midavaine, Christophe Clanet, and David Quéré. Antifogging abilities of model nanotextures. *Nature Materials*, 16(6):658–663, June 2017.
- [134] Lars Müller-Meskamp, Yong Hyun Kim, Teja Roch, Simone Hofmann, Reinhard Scholz, Sebastian Eckardt, Karl Leo, and Andrés Fabián Lasagni. Efficiency Enhancement of Organic Solar Cells by Fabricating Periodic Surface Textures using Direct Laser Interference Patterning. *Advanced Materials*, 24(7):906–910, February 2012.
- [135] James R. Nagel and Michael A. Scarpulla. Enhanced absorption in optically thin solar cells by scattering from embedded dielectric nanoparticles. *Opt. Express, OE*, 18(102):A139–A146, June 2010.
- [136] E. Najafabadi, K. A. Knauer, W. Haske, C. Fuentes-Hernandez, and B. Kippelen. Highly efficient inverted top-emitting green phosphorescent organic light-emitting diodes on glass and flexible substrates. *Applied Physics Letters*, 101(2):023304, July 2012.
- [137] E. Najafabadi, Y. H. Zhou, K. A. Knauer, C. Fuentes-Hernandez, and B. Kippelen. Efficient organic light-emitting diodes fabricated on cellulose nanocrystal substrates. *Applied Physics Letters*, 105(6):063305, August 2014.
- [138] D. Nanda, P. Varshney, M. Satapathy, S. S. Mohapatra, and A. Kumar. Self-assembled monolayer of functionalized silica microparticles for self-cleaning applications. *Colloids and Surfaces A: Physicochemical and Engineering Aspects*, 529:231–238, September 2017.

- [139] C. Neinhuis, K. Koch, and W. Barthlott. Movement and regeneration of epicuticular waxes through plant cuticles. *Planta*, 213(3):427–434, July 2001.
- [140] Masaya Nogi, Keishin Handa, Antonio Norio Nakagaito, and Hiroyuki Yano. Optically transparent bionanofiber composites with low sensitivity to refractive index of the polymer matrix. *Applied Physics Letters*, 87(24):243110, December 2005.
- [141] Masaya Nogi, Makoto Karakawa, Natsuki Komoda, Hitomi Yagyu, and Thi Thi Nge. Transparent Conductive Nanofiber Paper for Foldable Solar Cells. *Scientific Reports*, 5:17254, November 2015.
- [142] Masaya Nogi and Hiroyuki Yano. Transparent Nanocomposites Based on Cellulose Produced by Bacteria Offer Potential Innovation in the Electronics Device Industry. *Advanced Materials*, 20(10):1849–1852, 2008.
- [143] Masaya () Nogi, Changjae () Kim, Tohru () Sugahara, Tetsuji () Inui, Tsukasa () Takahashi, and Katsuaki () Sukanuma. High thermal stability of optical transparency in cellulose nanofiber paper. *Applied Physics Letters*, 102(18):181911, May 2013.
- [144] Masaya () Nogi and Hiroyuki () Yano. Optically transparent nanofiber sheets by deposition of transparent materials: A concept for a roll-to-roll processing. *Applied Physics Letters*, 94(23):233117, June 2009.
- [145] Kazuo Nojiri. *Dry Etching Technology for Semiconductors*. Springer, 2012.
- [146] Yoko Okahisa, Ayako Yoshida, Satoshi Miyaguchi, and Hiroyuki Yano. Optically transparent wood–cellulose nanocomposite as a base substrate for flexible organic light-emitting diode displays. *Composites Science and Technology*, 69(11):1958–1961, September 2009.
- [147] Monika Österberg, Jari Vartiainen, Jessica Lucenius, Ulla Hippi, Jukka Seppälä, Ritva Serimaa, and Janne Laine. A Fast Method to Produce Strong NFC Films as a Platform for Barrier and Functional Materials. *ACS Applied Materials & Interfaces*, 5(11):4640–4647, June 2013.
- [148] Daniel Packwood. *Bayesian Optimization for Materials Science*, volume 3. Springer, 2017.

- [149] Shuaijun Pan, Arun K. Kota, Joseph M. Mabry, and Anish Tuteja. Superomniphobic Surfaces for Effective Chemical Shielding. *Journal of the American Chemical Society*, 135(2):578–581, January 2013.
- [150] Kyoo-Chul Park, Hyungryul J. Choi, Chih-Hao Chang, Robert E. Cohen, Gareth H. McKinley, and George Barbastathis. Nanotextured Silica Surfaces with Robust Superhydrophobicity and Omnidirectional Broadband Supertransmissivity. *ACS Nano*, 6(5):3789–3799, May 2012.
- [151] Kyoo-Chul Park, Hyungryul J. Choi, Chih-Hao Chang, Robert E. Cohen, Gareth H. McKinley, and George Barbastathis. Nanotextured Silica Surfaces with Robust Superhydrophobicity and Omnidirectional Broadband Supertransmissivity. *ACS Nano*, 6(5):3789–3799, May 2012.
- [152] Sucheol Park and Jin Who Hong. Polymer dispersed liquid crystal film for variable-transparency glazing. *Thin Solid Films*, 517(10):3183–3186, March 2009.
- [153] C. Q. Peng, Y. S. Thio, and R. A. Gerhardt. Conductive paper fabricated by layer-by-layer assembly of polyelectrolytes and ITO nanoparticles. *Nanotechnology*, 19(50):505603, November 2008.
- [154] A. Piccolo. Thermal performance of an electrochromic smart window tested in an environmental test cell. *Energy and Buildings*, 42(9):1409–1417, 2010.
- [155] A. Poruba, A. Fejfar, Z. Remeš, J. Špringer, M. Vaněček, J. Kočka, J. Meier, P. Torres, and A. Shah. Optical absorption and light scattering in microcrystalline silicon thin films and solar cells. *Journal of Applied Physics*, 88(1):148–160, June 2000.
- [156] Colin Preston, Zhiqiang Fang, Joseph Murray, Hongli Zhu, Jiaqi Dai, Jeremy N. Munday, and Liangbing Hu. Silver nanowire transparent conducting paper-based electrode with high optical haze. *J. Mater. Chem. C*, 2(7):1248–1254, 2014.
- [157] Colin Preston, Yunlu Xu, Xiaogang Han, Jeremy N. Munday, and Liangbing Hu. Optical haze of transparent and conductive silver nanowire films. *Nano Res.*, 6(7):461–468, July 2013.
- [158] Sumit Purandare, Eliot F. Gomez, and Andrew J. Steckl. High brightness phosphorescent organic light emitting diodes on transparent and flexible cellulose films. *Nanotechnology*, 25(9):094012, February 2014.

- [159] Victor L. Pushparaj, Manikoth M. Shaijumon, Ashavani Kumar, Saravanababu Murugesan, Lijie Ci, Robert Vajtai, Robert J. Linhardt, Omkaram Nalamasu, and Pulickel M. Ajayan. Flexible energy storage devices based on nanocomposite paper. *Proceedings of the National Academy of Sciences*, 104(34):13574–13577, August 2007.
- [160] Dianpeng Qi, Nan Lu, Hongbo Xu, Bingjie Yang, Chunyu Huang, Miaojun Xu, Liguao Gao, Zhouxiang Wang, and Lifeng Chi. Simple Approach to Wafer-Scale Self-Cleaning Antireflective Silicon Surfaces. *Langmuir*, 25(14):7769–7772, July 2009.
- [161] Carl Edward Rasmussen and Christopher K. I. Williams. *Gaussian Processes for Machine Learning (Adaptive Computation and Machine Learning)*. The MIT Press, 2005.
- [162] Aamir Razaq, Leif Nyholm, Martin Sjödin, Maria Strømme, and Albert Mihranyan. Paper-Based Energy-Storage Devices Comprising Carbon Fiber-Reinforced Polypyrrole-Cladophora Nanocellulose Composite Electrodes. *Advanced Energy Materials*, 2(4):445–454, 2012.
- [163] Guofeng Ren, Shiqi Li, Zhao-Xia Fan, Md Nadim Ferdous Hoque, and Zhaoyang Fan. Ultrahigh-rate supercapacitors with large capacitance based on edge oriented graphene coated carbonized cellulosic paper as flexible freestanding electrodes. *Journal of Power Sources*, 325:152–160, September 2016.
- [164] Bichitra Sahoo, Kukro Yoon, Jungmok Seo, and Taeyoon Lee. Chemical and Physical Pathways for Fabricating Flexible Superamphiphobic Surfaces with High Transparency. *Coatings*, 8(2):47, January 2018.
- [165] Nasim Sahraei, Karen Forberich, Selvaraj Venkataraj, Armin G. Aberle, and Marius Peters. Analytical solution for haze values of aluminium-induced texture (AIT) glass substrates for a-Si:H solar cells. *Opt Express*, 22 Suppl 1:A53–67, January 2014.
- [166] Houssine Sehaqui, Andong Liu, Qi Zhou, and Lars A. Berglund. Fast Preparation Procedure for Large, Flat Cellulose and Cellulose/Inorganic Nanopaper Structures. *Biomacromolecules*, 11(9):2195–2198, September 2010.
- [167] Kwangseok Seo, Minyoung Kim, and Do Hyun Kim. Re-derivation of Young’s Equation, Wenzel Equation, and Cassie-Baxter Equation Based on Energy Minimization. *Surface Energy*, December 2015.

- [168] B. Shahriari, K. Swersky, Z. Wang, R. P. Adams, and N. de Freitas. Taking the human out of the loop: A review of bayesian optimization. *Proceedings of the IEEE*, 104(1):148–175, Jan 2016.
- [169] Md Iftekhar Shams, Masaya Nogi, Lars A. Berglund, and Hiroyuki Yano. The transparent crab: preparation and nanostructural implications for bioinspired optically transparent nanocomposites. *Soft Matter*, 8(5):1369–1373, January 2012.
- [170] Yifan Si, Zhichao Dong, and Lei Jiang. Bioinspired Designs of Superhydrophobic and Superhydrophilic Materials. *ACS Central Science*, 4(9):1102–1112, September 2018.
- [171] Radwanul Hasan Siddique, Guillaume Gomard, and Hendrik Hölscher. The role of random nanostructures for the omnidirectional anti-reflection properties of the glasswing butterfly. *Nature Communications*, 6:6909, April 2015.
- [172] Chunyan Song, Nan Zhang, Jie Lin, Xiaoyang Guo, and Xingyuan Liu. Sb(2)o(3)/ag/sb(2)o(3) multilayer transparent conducting films for ultraviolet organic light-emitting diode. *Scientific Reports*, 7:41250, 2017.
- [173] J. Springer, A. Poruba, and M. Vanecek. Improved three-dimensional optical model for thin-film silicon solar cells. *Journal of Applied Physics*, 96(9):5329–5337, October 2004.
- [174] Siddarth Srinivasan, Shreerang S. Chhatre, Joseph M. Mabry, Robert E. Cohen, and Gareth H. McKinley. Solution spraying of poly(methyl methacrylate) blends to fabricate microtextured, superoleophobic surfaces. *Polymer*, 52(14):3209–3218, June 2011.
- [175] D.G Stavenga, S Foletti, G Palasantzas, and K Arikawa. Light on the moth-eye corneal nipple array of butterflies. *Proceedings of the Royal Society B: Biological Sciences*, 273(1587):661–667, March 2006.
- [176] Jingyao Sun, Xiaobing Wang, Jinghua Wu, Chong Jiang, Jingjing Shen, Merideth A. Cooper, Xiuting Zheng, Ying Liu, Zhaogang Yang, and Daming Wu. Biomimetic Moth-eye Nanofabrication: Enhanced Antireflection with Superior Self-cleaning Characteristic. *Scientific Reports*, 8(1):5438, April 2018.

- [177] A. Taflove. Application of the finite-difference time-domain method to sinusoidal steady-state electromagnetic-penetration problems. *Electromagnetic Compatibility, IEEE Transactions on*, EMC-22(3):191–202, 1980.
- [178] Akihiro Tagaya, Michio Nagai, Yasuhiro Koike, and Kazuaki Yokoyama. Thin liquid-crystal display backlight system with highly scattering optical transmission polymers. *Appl. Opt., AO*, 40(34):6274–6280, December 2001.
- [179] GuanJun Tan, Jiun-Haw Lee, Yi-Hsin Lan, Mao-Kuo Wei, Lung-Han Peng, I.-Chun Cheng, and Shin-Tson Wu. Broadband antireflection film with moth-eye-like structure for flexible display applications. *Optica*, 4(7):678–683, July 2017.
- [180] R. H. Tredgold. *Order in Thin Organic Films*. Cambridge University Press, 1994. Google-Books-ID: 0M2h2G_zJJsC.
- [181] Anish Tuteja, Wonjae Choi, Minglin Ma, Joseph M. Mabry, Sarah A. Mazzella, Gregory C. Rutledge, Gareth H. McKinley, and Robert E. Cohen. Designing Superoleophobic Surfaces. *Science*, 318(5856):1618–1622, December 2007.
- [182] Anish Tuteja, Wonjae Choi, Joseph M. Mabry, Gareth H. McKinley, and Robert E. Cohen. Robust omniphobic surfaces. *Proceedings of the National Academy of Sciences*, 105(47):18200–18205, November 2008.
- [183] S. Ummartyotin, J. Juntaro, M. Sain, and H. Manuspiya. Development of transparent bacterial cellulose nanocomposite film as substrate for flexible organic light emitting diode (OLED) display. *Industrial Crops and Products*, 35(1):92–97, January 2012.
- [184] Jorik van de Groep, Dhritiman Gupta, Marc A. Verschuuren, Martijn M. Wienk, Rene A. J. Janssen, and Albert Polman. Large-area soft-imprinted nanowire networks as light trapping transparent conductors. *Scientific Reports*, 5:11414 EP –, 06 2015.
- [185] Jorik van de Groep, Pierpaolo Spinelli, and Albert Polman. Single-Step Soft-Imprinted Large-Area Nanopatterned Antireflection Coating. *Nano Letters*, 15(6):4223–4228, June 2015.
- [186] Claire van Lare, Frank Lenzmann, Marc A. Verschuuren, and Albert Polman. Dielectric Scattering Patterns for Efficient Light Trapping in Thin-Film Solar Cells. *Nano Lett.*, 15(8):4846–4852, August 2015.

- [187] Swambabu Varanasi and Warren J. Batchelor. Rapid preparation of cellulose nanofibre sheet. *Cellulose*, 20(1):211–215, February 2013.
- [188] Fang Wan, De-Quan Yang, and Edward Sacher. Repelling hot water from superhydrophobic surfaces based on carbon nanotubes. *Journal of Materials Chemistry A*, 3(33):16953–16960, August 2015.
- [189] Bo Wang and Lei L. Kerr. Dye sensitized solar cells on paper substrates. *Solar Energy Materials and Solar Cells*, 95(8):2531–2535, August 2011.
- [190] Fei Wang, Zhijian Chen, Lixin Xiao, Bo Qu, and Qihuang Gong. Papery solar cells based on dielectric/metal hybrid transparent cathode. *Solar Energy Materials and Solar Cells*, 94(7):1270–1274, July 2010.
- [191] Fuliang Wang, Peng Mao, and Hu He. Dispensing of high concentration Ag nanoparticles ink for ultra-low resistivity paper-based writing electronics. *Scientific Reports*, 6:21398, February 2016.
- [192] Nan Wang, Dangsheng Xiong, Sai Pan, Kun Wang, Yan Shi, and Yaling Deng. Robust superhydrophobic coating and the anti-icing properties of its lubricants-infused-composite surface under condensing condition. *New Journal of Chemistry*, 41(4):1846–1853, February 2017.
- [193] T. Wang, Y. Zhang, Y. Yan, C. G. Jones, and D. G. Lidzey. Polymer Light Emitting Diodes Powered via Paper-Mounted Electronics. *Journal of Display Technology*, 12(6):583–588, June 2016.
- [194] Xi Wang, Kezheng Gao, Ziqiang Shao, Xiaoqing Peng, Xue Wu, and Feijun Wang. Layer-by-Layer assembled hybrid multilayer thin film electrodes based on transparent cellulose nanofibers paper for flexible supercapacitors applications. *Journal of Power Sources*, 249:148–155, March 2014.
- [195] Ralf B. Wehrspohn, Uwe Rau, and Andreas Gombert. *Photon Management in Solar Cells*. John Wiley & Sons, March 2016. Google-Books-ID: lgm8CwAAQBAJ.
- [196] Robert N. Wenzel. Resistance of solid surfaces to wetting by water. *Industrial & Engineering Chemistry*, 28(8):988–994, 1936.

- [197] Kyle L. Wilke, Daniel J. Preston, Zhengmao Lu, and Evelyn N. Wang. Toward Condensation-Resistant Omniphobic Surfaces. *ACS Nano*, 12(11):11013–11021, November 2018.
- [198] Jessica X. H. Wong and Hua-Zhong Yu. Preparation of Transparent Superhydrophobic Glass Slides: Demonstration of Surface Chemistry Characteristics. *J. Chem. Educ.*, 90(9):1203–1206, September 2013.
- [199] Tak-Sing Wong, Sung Hoon Kang, Sindy K. Y. Tang, Elizabeth J. Smythe, Benjamin D. Hatton, Alison Grinthal, and Joanna Aizenberg. Bioinspired self-repairing slippery surfaces with pressure-stable omniphobicity. *Nature*, 477(7365):443–447, September 2011.
- [200] Hui Wu, Desheng Kong, Zhichao Ruan, Po-Chun Hsu, Shuang Wang, Zongfu Yu, Thomas J. Carney, Liangbing Hu, Shanhui Fan, and Yi Cui. A transparent electrode based on a metal nanotrough network. *Nature Nanotechnology*, 8(6):421–425, June 2013.
- [201] Jian Wu and Peter Frazier. The parallel knowledge gradient method for batch Bayesian optimization. In *Advances in Neural Information Processing Systems*, pages 3126–3134, 2016.
- [202] Tianzhun Wu and Yuji Suzuki. Design, microfabrication and evaluation of robust high-performance superlyophobic surfaces. *Sensors and Actuators B: Chemical*, 156(1):401–409, August 2011.
- [203] Fan Xia and Lei Jiang. Bio-Inspired, Smart, Multiscale Interfacial Materials. *Advanced Materials*, 20(15):2842–2858, 2008.
- [204] Xuezhu Xu, Jian Zhou, Long Jiang, Gilles Lubineau, Tienkhee Ng, Boon S. Ooi, Hsien-Yu Liao, Chao Shen, Long Chen, and J. Y. Zhu. Highly transparent, low-haze, hybrid cellulose nanopaper as electrodes for flexible electronics. *Nanoscale*, 8(24):12294–12306, June 2016.
- [205] Jixian Yan, Mei Yan, Lei Ge, Jinghua Yu, Shenguang Ge, and Jiadong Huang. A microfluidic origami electrochemiluminescence aptamer-device based on a porous Au-paper electrode and a phenyleneethynylene derivative. *Chemical Communications*, 49(14):1383–1385, January 2013.

- [206] Quanling Yang, Hayaka Fukuzumi, Tsuguyuki Saito, Akira Isogai, and Lina Zhang. Transparent Cellulose Films with High Gas Barrier Properties Fabricated from Aqueous Alkali/Urea Solutions. *Biomacromolecules*, 12(7):2766–2771, July 2011.
- [207] Quanling Yang, Haisong Qi, Ang Lue, Kai Hu, Gongzhen Cheng, and Lina Zhang. Role of sodium zincate on cellulose dissolution in NaOH/urea aqueous solution at low temperature. *Carbohydrate Polymers*, 83(3):1185–1191, January 2011.
- [208] Quanling Yang, Xingzhen Qin, and Lina Zhang. Properties of cellulose films prepared from NaOH/urea/zincate aqueous solution at low temperature. *Cellulose*, 18(3):681–688, June 2011.
- [209] Yang Yang, Xiangjia Li, Xuan Zheng, Zeyu Chen, Qifa Zhou, and Yong Chen. 3D-Printed Biomimetic Super-Hydrophobic Structure for Microdroplet Manipulation and Oil/Water Separation. *Advanced Materials*, 30(9):1704912, 2018. _eprint: <https://onlinelibrary.wiley.com/doi/pdf/10.1002/adma.201704912>.
- [210] H. Yano, J. Sugiyama, A. N. Nakagaito, M. Nogi, T. Matsuura, M. Hikita, and K. Handa. Optically Transparent Composites Reinforced with Networks of Bacterial Nanofibers. *Advanced Materials*, 17(2):153–155, 2005.
- [211] Yonggang Yao, Jinsong Tao, Jianhua Zou, Bilun Zhang, Tian Li, Jiaqi Dai, Mingwei Zhu, Sha Wang, Kun Kelvin Fu, Doug Henderson, Emily Hitz, Junbiao Peng, and Liangbing Hu. Light management in plasticâpaper hybrid substrate towards high-performance optoelectronics. *Energy & Environmental Science*, 9(7):2278–2285, 2016.
- [212] Xin Ye, Xiaodong Jiang, Jin Huang, Feng Geng, Laixi Sun, Xiaotao Zu, Weidong Wu, and Wanguo Zheng. Formation of broadband antireflective and superhydrophilic subwavelength structures on fused silica using one-step self-masking reactive ion etching. *Scientific Reports*, 5:srep13023, August 2015.
- [213] Kane Yee. Numerical solution of initial boundary value problems involving maxwell’s equations in isotropic media. *Antennas and Propagation, IEEE Transactions on*, 14(3):302–307, 1966.
- [214] Min-Hsin Yeh, Long Lin, Po-Kang Yang, and Zhong Lin Wang. Motion-Driven Electrochromic Reactions for Self-Powered Smart Window System. *ACS Nano*, 9(5):4757–4765, May 2015.

- [215] Jiale Yong, Feng Chen, Qing Yang, Jinglan Huo, and Xun Hou. Superoleophobic surfaces. *Chemical Society Reviews*, 46(14):4168–4217, 2017.
- [216] Peng You, Zhike Liu, Qidong Tai, Shenghua Liu, and Feng Yan. Efficient semi-transparent perovskite solar cells with graphene electrodes. *Advanced Materials*, 27(24):3632–3638, 2015.
- [217] Geun-Tae Yun, Woo-Bin Jung, Myung Seok Oh, Gyu Min Jang, Jieung Baek, Nam Il Kim, Sung Gap Im, and Hee-Tae Jung. Springtail-inspired superomniphobic surface with extreme pressure resistance. *Science Advances*, 4(8):eaat4978, August 2018.
- [218] Jungheum Yun, Wei Wang, Soo Min Kim, Tae-Sung Bae, Sunghun Lee, Donghwan Kim, Gun-Hwan Lee, Hae-Seok Lee, and Myungkwan Song. Light trapping in bendable organic solar cells using silica nanoparticle arrays. *Energy & Environmental Science*, 8(3):932–940, March 2015.
- [219] Imran Zada, Wang Zhang, Peng Sun, Muhammad Imtiaz, Waseem Abbas, and Di Zhang. Multifunctional, angle dependent antireflection, and hydrophilic properties of SiO₂ inspired by nano-scale structures of cicada wings. *Applied Physics Letters*, 111(15):153701, October 2017.
- [220] Valerio Zardetto, Thomas M. Brown, Andrea Reale, and Aldo Di Carlo. Substrates for flexible electronics: A practical investigation on the electrical, film flexibility, optical, temperature, and solvent resistance properties. *Journal of Polymer Science Part B: Polymer Physics*, 49(9):638–648, May 2011.
- [221] M. Zeman, R. a. C. M. M. van Swaaij, J. W. Metselaar, and R. E. I. Schropp. Optical modeling of a-Si:H solar cells with rough interfaces: Effect of back contact and interface roughness. *Journal of Applied Physics*, 88(11):6436–6443, November 2000.
- [222] Chi Zhang, Wenchao Li, Dongliang Yu, Yanshan Wang, Min Yin, Hui Wang, Ye Song, Xufei Zhu, Paichun Chang, Xiaoyuan Chen, and Dongdong Li. Wafer-Scale Highly Ordered Anodic Aluminum Oxide by Soft Nanoimprinting Lithography for Optoelectronics Light Management. *Advanced Materials Interfaces*, 4(5):1601116, 2017.
- [223] Gang Zhang, Dayang Wang, Zhong-Ze Gu, and Helmuth Möhwald. Fabrication of superhydrophobic surfaces from binary colloidal assembly. *Langmuir*, 21(20):9143–9148, August 2005.

- [224] Jie Zhang, Su Shen, Xiao X. Dong, and Lin S. Chen. Low-cost fabrication of large area sub-wavelength anti-reflective structures on polymer film using a soft PUA mold. *Optics Express*, 22(2):1842–1851, January 2014.
- [225] Lina Zhang, Dong Ruan, and Jinping Zhou. Structure and Properties of Regenerated Cellulose Films Prepared from Cotton Linters in NaOH/Urea Aqueous Solution. *Industrial & Engineering Chemistry Research*, 40(25):5923–5928, December 2001.
- [226] Xin-Tong Zhang, Osamu Sato, Minoru Taguchi, Yasuaki Einaga, Taketoshi Murakami, and Akira Fujishima. Self-Cleaning particle coating with antireflection properties. *Chemistry of Materials*, 17(3):696–700, February 2005.
- [227] Lisong Zhou, Alfred Wanga, Sheng-Chu Wu, Jie Sun, Sungkyu Park, and Thomas N. Jackson. All-organic active matrix flexible display. *Applied Physics Letters*, 88(8):083502, February 2006.
- [228] Yinhua Zhou, Canek Fuentes-Hernandez, Talha M. Khan, Jen-Chieh Liu, James Hsu, Jae Won Shim, Amir Dindar, Jeffrey P. Youngblood, Robert J. Moon, and Bernard Kippelen. Recyclable organic solar cells on cellulose nanocrystal substrates. *Scientific Reports*, 3:1536, March 2013.
- [229] Hongli Zhu, Zhiqiang Fang, Zhu Wang, Jiaqi Dai, Yonggang Yao, Fei Shen, Colin Preston, Wenxin Wu, Peng Peng, Nathaniel Jang, Qingkai Yu, Zongfu Yu, and Liangbing Hu. Extreme Light Management in Mesoporous Wood Cellulose Paper for Optoelectronics. *ACS Nano*, 10(1):1369–1377, January 2016.
- [230] Hongli Zhu, Zhengguo Xiao, Detao Liu, Yuanyuan Li, Nicholas J. Weadock, Zhiqiang Fang, Jinsong Huang, and Liangbing Hu. Biodegradable transparent substrates for flexible organic-light-emitting diodes. *Energy & Environmental Science*, 6(7):2105–2111, June 2013.
- [231] Mingwei Zhu, Tian Li, Chelsea S. Davis, Yonggang Yao, Jiaqi Dai, Yanbin Wang, Feras AlQatari, Jeffrey W. Gilman, and Liangbing Hu. Transparent and haze wood composites for highly efficient broadband light management in solar cells. *Nano Energy*, 26:332–339, August 2016.
- [232] Pingan Zhu, Tiantian Kong, Xin Tang, and Liqui Wang. Well-defined porous membranes for robust omniphobic surfaces via microfluidic emulsion templating. *Nature Communications*, 8:15823, June 2017.

- [233] André Zitzler-Kunkel, Martin R. Lenze, Nils M. Kronenberg, Ana-Maria Krause, Matthias Stolte, Klaus Meerholz, and Frank Würthner. NIR-Absorbing Merocyanine Dyes for BHJ Solar Cells. *Chem. Mater.*, 26(16):4856–4866, August 2014.